MŰEGYETEM 1782

Ph.D. Thesis

Spectroscopic studies in magnetoelectric and spiral antiferromagnets

Boglárka Tóth

Supervisor:

Dr. Sándor Bordács

Department of Physics
Budapest University of Technology and Economics

Budapest
2025

Acknowledgments

First and foremost, I cannot be thankful enough to my supervisor, Dr. Sándor Bordács, without whom this Ph.D. would not have been possible. His immense patience and knowledge were invaluable throughout many aspects of my studies. I also thank all my colleagues at the department. I must thank Estonian colleagues for their warm welcome in cold Tallinn. Thank you to my friends and loved ones who kept my spirits high when they would have otherwise fallen.

This work was supported by the Hungarian National Research, Development and Innovation Office – NKFIH grants FK 135003 and by the Ministry of Culture and Innovation and the National Research, Development and Innovation Office within the Quantum Information National Laboratory of Hungary (Grant No. 2022-2.1.1-NL-2022-00004).

Contents

Chapter 1

Introduction

The fields of electronics and information technology are facing challenges recently. Moore's law, which predicted a steady rate of ever smaller and smaller transistor sizes [1, 2], and hence the increase in information density, is nearing a halt. Today's transistors are, however, so small (a few nanometers) that this miniaturization rate cannot be sustained due to the heat generated by the densely integrated components as well as quantum-mechanical effects such as tunneling existing at such small length scales. Fabrication and engineering tricks have to be implemented to push feature sizes to the few nm range [3–5], while CPU clock rates have been stagnating in the GHz range since the mid-2000's [6, 7]. Moreover, the development of artificial intelligence (AI), machine learning, and the internet of things (IoT) is more data-intense, thus, requires more efficient and more closely integrated computation and memory devices. As more and more activities require computers, the energy needed to run them and cool the elements within increases steadily [8]. To keep up with these rapidly increasing needs of today's humanity, new platforms are needed.

Newly emerging fields in physics may provide a solution to such problems. The field of spintronics utilizes the spin of the electron in addition to its electric charge [9]. Spintronic technologies have already demonstrated success in devices that, for example, use the GMR (giant magnetoresistance) and TMR (tunnel magnetoresistance) effects in magnetic field sensors, and magnetic random access memories (MRAMs) [10]. Recently, the focus of spintronics moved to antiferromagnets [11–20], which gave a new boost to the study of antiferromagnetic (AFM) materials. The application of such compounds could have significant benefits as (1) the wide variety of AFM orders offers new possibilities to encode information, (2) their THz dynamics promise great speed, and (3) the absence of net magnetization makes them robust against stray magnetic fields. However, due to the lack of magnetization, the detection and manipulation of the AFM order is a challenging task, and it is not clear which form of AFM order suits the best applications.

The magnetoelectric (ME) effect may provide an alternative approach to detect and control the magnetic order. In these materials, the electric polarization and the magnetism are cross-coupled allowing an efficient, electric field control of the magnetic order. Although these two forms of long range order usually exclude each other [21], already in the 19^{th} century P. Curie predicted [22], the existence of ME materials, in which a magnetic field induces electric polarization and an electric field induces magnetization. L. D. Landau and E. M. Lifshitz showed [23], that linear ME effect can emerge only when the inversion and time-reversal symmetries are simultaneously broken, since the electric field and the electric polarization are time-reversal even polar vectors, while magnetic field and magnetization are time-reversal odd axial vectors. The linear ME effect was observed for the first time in Cr_2O_3 [24] in the 1960's, but remained under the radar for the next decades. In the early 2000's, it was shown in manganates [25] that in multiferroic materials with coexisting ferroelectric and magnetic orders, the ME signal can be amplified by several orders of magnitude. This discovery initiated a revival of the research of ME effects [26], motivated by the interest in materials with cross-coupled order parameters as well as by potential applications in efficient memory and logic devices [27]. As opposed to magnetoresistive systems and current controlled spintronic devices, the writing and reading of information could be done without generating much Joule heat with the application of multiferroic materials [28]. Among others, my research group proposed that multiferroic materials could also be used as optical rectifiers, since the absorption of electromagnetic waves differs significantly for beams propagating in opposite directions [29].

Antiferromagnets (AFMs) can also host ME coupling, and have the advantage over ferromagnets, that they are resistant to stray fields. An antiferromagnet is a type of compensated ordering of magnetic moments first predicted by L. Néel in his thesis [30] and was of the opinion that this phenomenon is more of a curiosity than a useful trait that can be utilized [31]. In these kind of magnetic materials, long range order exists, but no net moment is observable, since it is a compensated structure. Depending on the interaction between magnetic moments, there are many ways to form such compensated structures [32]. In the simplest case of the so-called Néel state, it is a two-sublattice formation of spins, where the magnetic moments $\mathbf{M}_1$ on one sublattice point in the opposite direction than moments $\mathbf{M}_2$ on the other sublattice.

A deeper understanding of the underlying physical phenomena behind potential materials for applications is key to technological advancement. My thesis aims to contribute to that fundamental knowledge by studying unconventional antiferromagnets, which may open novel routes for applications. Furthermore, the emergence of the non-trivial cross-coupling effect and topological AFM spin textures provides interesting questions also from the basic research point of view.

These issues motivated my research equally. Specifically, I investigated the following compounds: a collinear AFM with a large ME effect, $LiCoPO_4$, an AFM proposed to host AFM skyrmions, $MnSc_2S_4$, and $BiFeO_3$, which has several modulated AFM states and also possesses strong ME coupling.

My thesis is organized as follows: In Chapter 2, I am going to introduce the main theoretical concepts that are needed to understand the motivation, and the results of my experiments. To get insights to the experimental techniques used in the measurements, Chapter 3 describes the various probing methods that I applied throughout my studies. Then, in Chapter 4, I present the optical spectroscopy experiments I performed on $LiCoPO_4$, and I show images of the antiferromagnetic domains which I could differentiate by utilizing the nonreciprocal directional dichroism observed in the spectroscopy data. The next chapter, Chapter 5 presents experiments on a ME multiferroic antiferromagnet with incommensurate magnetic order, $BiFeO_3$. After briefly summarizing the most important properties of $BiFeO_3$ from the point of view of my experiments, I show small-angle neutron scattering data that support previous works introducing a new high-temperature field-induced magnetic phase in the material. This is followed by the presentation of magnetic-field dependent THz absorption spectroscopy conducted at and above room temperature in this phase. In Chapter 6, I describe my spectroscopic investigations in the GHz range on an other noncollinear antiferromagnet $MnSc_2S_4$. I present magnetic-field-dependent THz absorption spectra and broadband microwave absorption data recorded in the antiferromagnetically ordered, as well as in the paramagnetic state of the compound. Finally, I summarize my work and present my thesis points in Chapter 7.

Chapter 2

Theoretical summary

Throughout my doctoral research, I investigated antiferromagnets. They either have nontrivial magnetic orderings, such as $MnSc_2S_4$, or are magnetoelectric, like $LiCoPO_4$, or both, as it is the case for multiferroic $BiFeO_3$. In this chapter, the reader will get a brief introduction to the theoretical concepts and the phenomena that motivated my research. First, there is an overview of magnetic interactions. Then, two major concepts are discussed: magnetoelectric coupling and multiferroicity, which are two independent phenomena, but in most cases we cannot talk about one without mentioning the other.

2.1 Magnetic interactions

Magnetic materials have fascinated people for thousands of years. They were used in practice since ancient times, however, their description was delayed until the 20th century. Electromagnetism had already been established, magnetic induction was well described, but the origin of magnetism had not yet been explained. A major step towards that was when the theory of quantum mechanics was established.

As a starting point for understanding magnetism, let us consider the origin of the atomic magnetic moment. According to Hund's rules, determining the electron configuration in the ground state, atoms (and ions) tend to maximize their total spin S and then their total orbital angular momentum L. Therefore, atoms with partially filled orbitals have a magnetic moment due to the non-zero angular momentum of the electrons. The Coulomb interaction plays an important role in splitting the energy levels of the many electron states having different spin states. Although the Coulomb interaction does not explicitly depends on the spin, Pauli's principle links the orbital states to the spin states. As the total wave function of fermions such as electrons is antisymmetric, a symmetric orbital part comes with an antisymmetric spin part and vice versa. In case of the two electron problem, the symmetric and antisymmetric part of the wave function have the following form

$$\Psi_{\mathrm{symm}}(\mathbf{r}_1,\mathbf{r}_2) = \frac{1}{\sqrt{2}}[\varphi_a(\mathbf{r}_1)\varphi_b(\mathbf{r}_2) + \varphi_b(\mathbf{r}_1)\varphi_a(\mathbf{r}_2)] \tag{2.1}$$

and

$$\Psi_{\mathrm{a.symm}}(\mathbf{r}_1,\mathbf{r}_2) = \frac{1}{\sqrt{2}}[\varphi_a(\mathbf{r}_1)\varphi_b(\mathbf{r}_2) - \varphi_b(\mathbf{r}_1)\varphi_a(\mathbf{r}_2)], \tag{2.2}$$

where φ_a and φ_b are spatial one-electron wavefunctions.

Considering two electrons on an atom, the two-electron Hamiltonian can be written as

$$\mathcal{H} = h_0(\mathbf{r}_1) + h_0(\mathbf{r}_2) + \frac{1}{4\pi\varepsilon_0}\frac{e^2}{|\mathbf{r}_1 - \mathbf{r}_2|}, \tag{2.3}$$

where $h_0(\mathbf{r}) = -\frac{\hbar^2}{2m}\nabla^2 - \frac{Ze^2}{4\pi\varepsilon_0 r}$ is the one-electron Hamiltonian with the electronic charge $-e$ and electron mass m, atomic number Z, ε_0 is the vacuum permittivity, and $\hbar$ is the reduced Planck constant. The third term in Eq. (2.3) is the Coulomb interaction between the two electrons. The eigenenergies of this Hamiltonian

$$E = 2E_0 + C_{ab} \pm J_{ab}, \tag{2.4}$$

correspond to the symmetric and antisymmetric wavefunctions, respectively. In Eq. (2.4), $C_{ab} > 0$ is the Coulomb integral, J_{ab} is the exchange integral

$$J_{ab} = e^2 \int \frac{\varphi_a^*(\mathbf{r}_1)\varphi_b(\mathbf{r}_1)\varphi_b^*(\mathbf{r}_2)\varphi_a(\mathbf{r}_2)}{|\mathbf{r}_1 - \mathbf{r}_2|}\mathrm{d}\mathbf{r}_1\mathrm{d}\mathbf{r}_2. \tag{2.5}$$

Because electronic orbitals of the same atom are orthogonal, it can be shown that the exchange integral is always positive, $J_{ab} > 0$, energetically favoring the spatial wave functions to be antisymmetric. This means that the corresponding symmetric spin state (called triplet) with parallel spins, and total spin $S = 1$ will have lower energy than the antisymmetric spin state (singlet) with total spin $S = 0$. Thus, the direct exchange of atomic orbitals supports parallel ordering of spins, which, in essence, is Hund's first rule.

The effect of the Hamiltonian in Eq. (2.3) can be rewritten omitting an additive constant in terms of spin operators

$$\mathcal{H} = -2J\mathbf{S}_1\mathbf{S}_2. \tag{2.6}$$

The Heisenberg exchange Hamiltonian introduced in Eq. (2.6) captures the interaction between the two electrons by the relative orientation of their spins, $\mathbf{S}_1$ and $\mathbf{S}_2$ through a coupling constant J. When talking about electron interactions on the same atom, $J > 0$ represents Hund's first rule, thus it is termed as Hund's rule coupling. Not restricting the discussion to single atoms and allowing non-orthogonal electronic wavefunctions (nonzero overlap), J may contain different Coulomb terms (on-site and inter-site Coulomb integrals, exchange, pair hopping, etc.), and overlap integrals, and can take negative values as well. Depending on the sign of J, the energy is minimized for parallel ($J > 0$), ferromagnetic, or antiparallel ($J < 0$), antiferromagnetic spin configurations.

Generalizing Eq. (2.6) for a lattice where spin $\mathbf{S}_i$ is on a lattice site $\mathbf{R}_i$, and the exchange between spins is characterized by $J_{ij} = J(\mathbf{R}_i - \mathbf{R}_j)$, the effective Hamiltonian can be written as

$$\mathcal{H} = -\sum_{i \neq j} J_{ij} \mathbf{S}_i \mathbf{S}_j. \tag{2.7}$$

If the (direct or indirect) overlap is large enough, additionally to the first neighbors (nearest neighbors), second, third etc. neighbors (next-nearest, next-next-nearest neighbors, etc.) can be taken into consideration for calculations. When $J_{ij} > 0$, the interaction is ferromagnetic, for $J_{ij} < 0$, the interaction is antiferromagnetic.

The Hamiltonians in Eqs. (2.6) and (2.7) are SU(2) symmetric, i.e., do not favor a specific spin direction, only the relative spin orientations. In a long-range ordered state, however, the spins point to a specific direction, thus the realized state spontaneously brakes the symmetry of the Hamiltonian. According to the Goldstone theorem [33], this breaking of a continuous symmetry manifests in the emergence of gapless excitations.

Taking the relativistic Dirac equation, and expanding it in terms of $1/c$, a term arises, that couples the spin and orbital moments of the electron. The relativistic spin-orbit term in the Dirac Hamiltonian of a hydrogen-like atom, i.e., one electron in a Coulomb potential is [34]

$$\mathcal{H}_{\mathrm{s-o}} = \frac{\hbar^2}{2m^2c^2} \frac{Ze^2}{r^3} \mathbf{L} \cdot \mathbf{S}, \tag{2.8}$$

where $\mathbf{L}$ and $\mathbf{S}$ are the orbital momentum and the spin operators, respectively, and c is the speed of light. The consequence of this term in the Hamiltonian, that L and S are no longer conserved quantities, only the total angular momentum $\mathbf{J} = \mathbf{L} + \mathbf{S}$. From this follows Hund's third rule that the total angular momentum of an atom $J = |L - S|$ for less than half-filled, and $J = L + S$ for more than half filled shells.

On the other hand, the ground state electronic configuration of an atom depends also on the surrounding environment of the incomplete electron shell, for example, in an ionic octahedron. Applying Hund's rules to find the electron configuration in these cases does not match with measured spin values. This surrounding inhomogeneous electric field is called the crystal or ligand field. The crystal field splits the orbital levels, and may cause the quenching of the orbital moment.

In crystals which, by their symmetry, have distinguished directions, the magnetic Hamiltonian is anisotropic. For example, in tetragonal crystals, where the z axis is privileged, the exchange Hamiltonian will have the form [35]

$$\mathcal{H} = -\sum_{i\neq j} J_{ij}(S_i^x S_j^x + S_i^y S_j^y + \Delta S_i^z S_j^z). \tag{2.9}$$

This is a case for uniaxial anisotropy. For $\Delta > 1$, the material has an easy axis: the z components of the spins are coupled stronger than the other two, i.e., the z direction is preferred for the alignment of spins. In case of $\Delta < 1$, the coupling to the xy plane will be stronger, thus, the material has an easy plane. The extreme case of the uniaxial anisotropy is the Ising model, where only the S_i^z components are coupled. For $S > 1/2$, the low crystal symmetry may also manifest in on-site or single-ion anisotropy, which has the form $K(S_i^z)^2$ in the effective Hamiltonian of an axial crystal, where K is the anisotropy parameter.

There can be an effective exchange interaction between magnetic moments on different atomic sites even when the direct overlap of their electronic wavefunctions is negligible. Then, an indirect exchange can happen via a neighboring non-magnetic intermediary anion (e.g. O^{2-}, F^-), which is called the superexchange center, and the interaction is dubbed the superexchange interaction. Superexchange, similarly to direct exchange, is also a result of the Pauli exclusion principle and the Coulomb repulsion between electrons. As an example, in MnO, the d orbitals of the transition-metal Mn^{2+} ions overlap with the p orbitals of the intermediary ion O^{2-}, and the d-orbital magnetic moments of the transition-metal ions interact. Based on the angle between the three ions, the exchange can be either ferromagnetic or antiferromagnetic as described by the Goodenough-Kanamori rules: if the bond angle $\theta_{\mathrm{B}} = 90^\circ$, the exchange is ferromagnetic, and for $\theta_{\mathrm{B}} \approx 180^\circ$, the exchange is antiferromagnetic [36, 37]. Another type of indirect exchange can be observed in metals, where the exchange interaction can be mediated via conduction electrons, known as the Ruderman-Kittel-Kasuya-Yosida (RKKY) interaction [38–40].

The particular symmetry of a system can also allow additional exchange terms: in the absence of inversion symmetry, the Dzyaloshinskii-Moriya (DM) term becomes allowed (e.g., when the central O^{2-} moves away from the axis defined by the metal ions in case of superexchange). This term was proposed by Dzyaloshinskii [41] and Moriya [42, 43] to explain the weak ferromagnetic moment arising in antiferromagnets with broken inversion symmetry on bonds of magnetic ions. The DM interaction is an antisymmetric exchange interaction that has the form

$$\mathcal{H}_{\mathrm{DM}} = \mathbf{D} \cdot (\mathbf{S}_i \times \mathbf{S}_j), \tag{2.10}$$

where $\mathbf{D}$ is the DM vector. For the direction of $\mathbf{D}$, Moriya stated rules in Ref. [43] based on symmetry considerations. The energy of $\mathcal{H}_{\mathrm{DM}}$ is minimal for perpendicular spins.

When multiple spin interactions of comparable magnitudes are present in a spin-system, the preferred spin configurations of the interactions are not granted to match. The competition of the interactions result in frustration. Their compromise often manifests in a modulated spin configuration, such as spin helices (dysprosium, holmium), conical (holmium, erbium) or cycloidal ($BiFeO_3$) structures.

2.2 Multiferroics

After a new method of classifying materials introduced by K. Aizu [44], the term multi-ferroic was coined by H. Schmid [45], referring to materials, in which two or more ferroic states are present in the same phase. A ferroic state, in general, is a state with $q = 0$ long range order (i.e., no modulation) that is switchable by a homogeneous external field. The four primary ferroic properties are ferroelastic, ferroelectric, ferromagnetic and ferrotoroidal. A ferroelastic material has spontaneous strain in its structure, that can be switched with external stress. Considering time-reversal and inversion symmetries, this state is invariant to both of them. In the ferroelectric state, electric polarization can be switched with the application of electric fields. Ferroelectric order is invariant under time-reversal, but antisymmetric to spatial inversion. Magnetization is switchable with external magnetic field in a ferromagnet. Ferromagnetism is antisymmetric under time-reversal, but remains invariant upon spatial inversion. A relatively new concept, ferrotoroidicity completes the listing of ferroic orders, being antisymmetric both under time-reversal and spatial inversion. Its order parameter, the toroidal moment [46] emerges from a vortex-like alignment of magnetic moments analogous to the magnetic moment induced by a current loop, but can be thought of also as the cross-product of local polarization and magnetization. In this last case, the control field is a combination of crossed magnetic and electric fields.

Nowadays, the term multiferroic is used for materials showing electric polarization and some kind of magnetic order (not only ferromagnetism). In this thesis, I also follow this definition as shown by the red hatched area in Fig. 2.1. The combination of a large electric polarization and a magnetization in a single phase is highly desirable to achieve cross-coupling between these properties, however, it is not very common [21]. The materials hosting these two orders are classified by the origin of the ferroelectric polarization [52]. Type-I multiferroics are materials, in which magnetism and ferroelectricity have different origins and principally appear to be independent of each other. Usually, as temperature decreases after solidification, it is the ferroelectric order that appears first, e.g., in $BiFeO_3$, which will be discussed more in detail in Chapter 5. In contrast, the magnetic order itself induces ferroelectric polarization in type-II multiferroics. Consequently, the coupling between the two orders is strong, but the ferroelectric polarization is usually

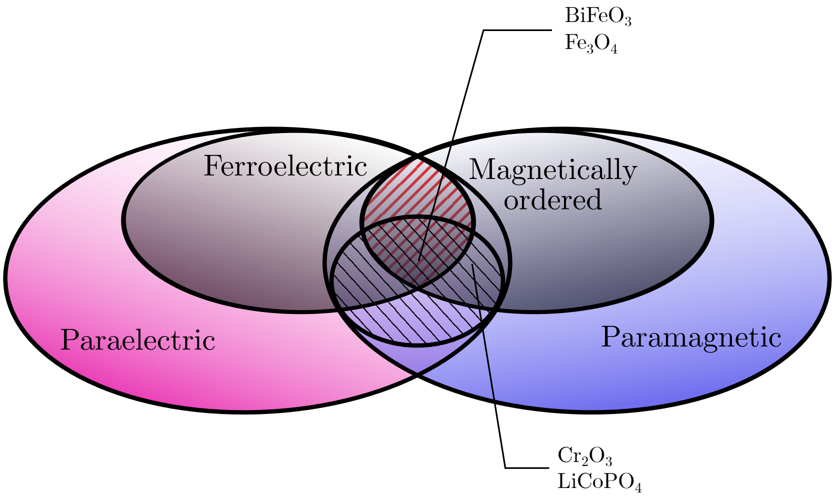

Figure 2.1: Classification of magnetoelectric and multiferroic materials. Paraelectrics are electrically polarizable materials, whose subset is ferroelectric materials that possess spontaneous switchable polarization. Magnetically ordered materials are a subset of paramagnets, allowing ferromagnetic, ferrimagnetic and antiferromagnetic orders. Multiferroic materials are in the intersection of the circles representing magnetically ordered and ferroelectric materials (red hatched region). The black hatched area represents materials where linear ME effect is observed, which are not necessarily multiferroic. Some examples for the most important cross-sections: Cr_2O_3 [47] and $LiCoPO_4$ [48] are antiferromagnetic ME materials, but have no net electric polarization. Magnetite Fe_3O_4 [49, 50] is a ferroelectric ferrimagnet showing ME coupling. $BiFeO_3$ is an antiferromagnetic ferroelectric, that also shows ME effects. Venn diagram is based on Ref. [51].

weak. Orthorhombic manganites, $R\mathrm{MnO}_3$ with spin spiral order are prototypes of type-II multiferroics.

Type-I multiferroics can be further categorized considering the mechanism leading to their ferroelectricity, as shown in Fig. 2.2 (a)–(c). First, ferroelectricity may be induced via the lone-pair mechanism [2.2 (a)]. A prominent example for the emergence of polarization due to lone pairs is BiFeO_3. The Bi^{3+} ions have two $6s$ electrons that are not involved in chemical bonds. These are the so-called lone pairs, which are well polarizable and create a local dipole by ordering in one direction. Secondly, polarization can arise from purely geometric reasons too [2.2 (b)]. For example, in h-$R\mathrm{MnO}_3$, a unit-cell trimerizing lattice distortion [56, 57] is what leads to a ferroelectric phase transition. Charge ordering can also be responsible for electric polarization [2.2 (c)]. Valence electrons localized on a superlattice breaking inversion symmetry may lead to ferroelectricity as hypothesized in $\mathrm{LuFe}_2\mathrm{O}_3$ [58].

The different spin-dependent mechanisms that can induce electric polarization in type-II multiferroics are illustrated in Fig. 2.2 (d). The non-centrosymmetric nature of a spin structure, e.g., a spin-cycloid can induce polarization via the so-called inverse Dzyaloshinskii-Moriya (DM) interaction. This mechanism corresponds to the energy gain of distorting a bond connecting non-collinear spins. Magnetic frustration can lead to the formation of a spin cycloid, thus, frustrated systems with non-collinear order are good candidates when looking for type-II multiferroics. Contrasting the above mentioned spin-cycloids, in collinear magnets, a Heisenberg-like exchange striction can cause charge displacements [59]. A third phenomenon leading to ferroelectric polarization, which is irrespective of the non-collinearity of the spin order, is the spin-dependent $p-d$ hybridization. Spin-orbit coupling (SOC) can influence a locally polar bond between the transition metal having the spin and the ligand site which hybridize based on the spin direction.

As an outlook, I mention that there exist so-called composite multiferroics, one group of which are hybrid systems of ferromagnetic magnetostrictive and ferroelectric piezoelectric components either in granular or in layered form. In these composites, strain is induced in the magnetic layer by a magnetic field via magnetostriction. Then, this strain is transferred to the piezoelectric component, where this strain induces a voltage [55].

The existence of multiple ferroic orders in a single phase can serve with unique advantages, especially in the case of ferroelectricity and magnetism. A coupling between those two orders (black hatched area in Fig. 2.1), the so-called magnetoelectric (ME) coupling may open new doors for applications.

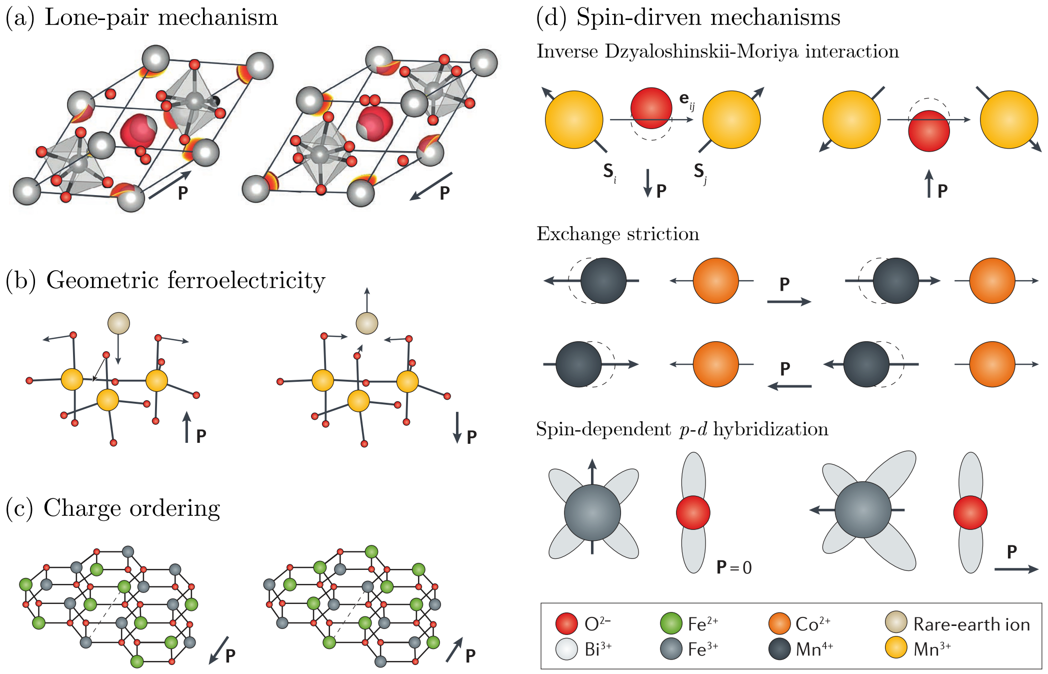

Figure 2.2: Summary of mechanisms inducing ferroelectric polarization in a multiferroic material. (a) Polarization emerging in $BiFeO_3$ as a result of the lone-pair mechanism. The two electrons of Bi^{3+} ions shift along the body diagonal. (b) in h-$R$$MnO_3$, MnO_5 pyramids tilt and deform, thus displacing the rare-earth ion, resulting in an electric polarization. (c) Charge ordering between nonbalanced Fe^{2+} and Fe^{3+} sites can lead to spontaneous polarization. (d) Spin-driven mechanisms of emergent ferroelectricity [53, 54]. Top: a non-centrosymmetric spin-structure allows the emergence of a polarization via the inverse DM interaction. Middle: Symmetric spin-exchange can lead to magnetostriction, resulting in polar distortions. Bottom: Chemical bonds can be modulated by the orientation of the spin of the participating transition metal ion, developing spontaneous polarization parallel to the bond direction. Figure adapted from Ref. [55].

2.3 Magnetoelectric effect

In a material, a magnetic field can cause magnetization proportional to the magnetic field. This linear response function, the magnetic susceptibility χ^m is a characteristic of the material. In general, χ^m is a tensor, meaning that the susceptibility of a sample may depend on the relative orientation of the crystallographic directions and the direction of the external magnetic field

$$M_i = \chi^m_{ij} H_j. \tag{2.11}$$

Following this, longitudinal and transverse susceptibilities can be defined. In the former case, magnetization is measured as a response to a small magnetic field applied parallel to a large external field, while in the latter, the probing and the bias magnetic fields are perpendicular to each other.[1]

In some materials, magnetic field can not only induce magnetization, but also electric polarization. This phenomenon, the magnetoelectric effect is discussed below, the essence of which was first predicted by P. Curie [22] stating that magnetization **M** can be induced by an electric field **E**, and simultaneously, electric polarization **P** can be induced by a magnetic field **H**. This unusual response can be derived from the Landau free energy expansion

$$\begin{aligned} F(\mathbf{E},\mathbf{H}) =& F_0 - P^S_i E_i - \mu_0 M^S_i H_i - \\ & -\frac{1}{2}\varepsilon_0 \chi^e_{ij} E_i E_j - \frac{1}{2}\mu_0 \chi^m_{ij} H_i H_j - \sqrt{\varepsilon_0 \mu_0}\chi^{me}_{ij} E_i H_j - .., \end{aligned} \tag{2.12}$$

where $\mathbf{P}^S$ and $\mathbf{M}^S$ are the spontaneous polarization and magnetization, and $\hat{\chi}^e$ and $\hat{\chi}^m$ are the dimensionless electric and magnetic susceptibility tensors, respectively, ε_0 is the vacuum permittivity, μ_0 is the vacuum permeability, and $1/\sqrt{\varepsilon_0 \mu_0} = c$, the speed of light. The tensor $\hat{\chi}^{me}$ is the dimensionless linear ME susceptibility. By differentiating with respect their respective conjugate fields, we obtain the polarization

$$P_i(\mathbf{E},\mathbf{H}) = -\frac{\partial F}{\partial E_i} = P^S_i + \varepsilon_0 \chi^e_{ij} E_j + \sqrt{\varepsilon_0 \mu_0}\chi^{me}_{ij} H_j + \dots \quad , \tag{2.13}$$

and the magnetization

$$M_i(\mathbf{E},\mathbf{H}) = -\frac{1}{\mu_0}\frac{\partial F}{\partial H_i} = M^S_i + \chi^m_{ij} H_j + \sqrt{\frac{\varepsilon_0}{\mu_0}}\chi^{me}_{ji} E_j + \dots \quad , \tag{2.14}$$

---

[1] At this point it is worth noting that in experiments, the applied magnetic field is often given by the magnetic induction (or flux density), **B** in units of [T]. In free space the two differ by a constant: $\mathbf{B} = \mu_0 \mathbf{H}$, where **H** is the magnetic field in units of [A/m] and μ_0 is the vacuum permeability.

and see that via $\hat{\chi}^{me}$, the electric polarization and the magnetic field are connected, just as magnetization and electric field. It is important to note the existence of higher-order susceptibilities, however, most research is focused on the linear ME term, and thus the adjective "linear" is often omitted.

In spite of being predicted by P. Curie in 1894 [22] and preliminary observations of similar effects in moving media [60, 61], the first observation of true static ME effect was in Cr_2O_3 by D. N. Astrov in 1960 [62], showing a coupling constant $\chi^{me}_{zz}/c = 4.13$ ps/m. The experiment confirmed the prediction of I. Dzyaloshinskii [63] who pointed out first that the linear magnetoelectric effect is allowed only in materials where time-reversal and inversion symmetries are simultaneously broken. This is a necessary condition as electric and magnetic fields transform oppositely under these symmetries and the free energy must be invariant. In his seminal paper, Dzyaloshinskii also suggested Cr_2O_3 as a candidate to verify the presence of the ME effect as its long-range antiferromagnetic order not only breaks time-reversal but also the inversion symmetry. The larger the ME coupling constant, the larger the induced polarization in the compound, which makes it the more desirable for applications. Materials where electric fields can not only modulate the magnetization but can facilitate switching between different magnetic states are extremely appealing for memory and logic devices. In this respect multiferroics with coupled ferroelectric and magnetic order are particularly interesting as they may allow the construction of low-dissipation, voltage controlled devices [27].

The electric and magnetic dipole moments are entangled not only in the static limit but they have coupled dynamics as well. This dynamic ME effect, the magnetization (polarization) induced by an oscillating electric (magnetic) field is expressed as

$$\Delta M_i^{\omega} = \sqrt{\frac{\varepsilon_0}{\mu_0}}\chi_{ij}^{me}(\omega)E_j^{\omega}, \tag{2.15}$$

and

$$\Delta P_j^{\omega} = \sqrt{\varepsilon_0\mu_0}\,\chi_{ji}^{em}(\omega)H_i^{\omega}, \tag{2.16}$$

where $\chi^{me}(\omega)$ and $\chi^{em}(\omega)$ are the ME susceptibility tensors. Numerous optical phenomena are the consequences of the extension of ME coupling to finite frequencies [64].

One manifestation of the ME effect is the so-called nonreciprocal directional dichroism (NDD). Experiments that I present in this thesis also focus on this ME effect. NDD is the nonreciprocal absorption of counter-propagating light beams. This effect can be understood in the following simplistic way. It is an interplay of electric and magnetic dipoles simultaneously excited in a magnetoelectric compound. The oscillation of the polarization is induced by the electric component of the light via the electric susceptibility as well as the magnetic field via the ME susceptibility $\chi^{me}(\omega)$. Since the relative sign of the electric and magnetic fields are reversed when the light propagation is reversed, these two contributions either add up or subtract leading to a propagation dependent refractive index and absorption coefficient. The same reasoning holds for the oscillating magnetization as well. Thus, the transmitted intensity depends on the direction of the illuminating light beam, even for unpolarized light.

The dynamical susceptibility tensors can be calculated from the Kubo formula [65, 66]

$$\chi_{ij}^{me}(\omega) = \frac{2}{\hbar}\sum_n \frac{\omega_{n0}\,\mathrm{Re}\{\langle 0|m_i|n\rangle\langle n|e_j|0\rangle\} + i\omega\,\mathrm{Im}\{\langle 0|m_i|n\rangle\langle n|e_j|0\rangle\}}{\omega_{n0} - \omega^2 - 2i\omega\delta} \tag{2.17a}$$

$$\chi_{ij}^{em}(\omega) = \frac{2}{\hbar}\sum_n \frac{\omega_{n0}\,\mathrm{Re}\{\langle 0|e_i|n\rangle\langle n|m_j|0\rangle\} + i\omega\,\mathrm{Im}\{\langle 0|e_i|n\rangle\langle n|m_j|0\rangle\}}{\omega_{n0} - \omega^2 - 2i\omega\delta}, \tag{2.17b}$$

where $|0\rangle$ is the ground state, $|n\rangle$ are the excited states, and the excitation energy to reach from the ground state is $\hbar\omega_{n0}$, both by means of magnetic m_i and electric e_j dipole operators. The susceptibilities can be split to parts proportional to the real and imaginary parts of the matrix elements noted with $'$ and $''$, respectively. The real part changes sign, while the imaginary part is invariant under time-reversal. The Kubo formula connects $\hat{\chi}^{me}$ and $\hat{\chi}^{em}$:

$$\chi_{ij}^{me}(\omega) = \chi'_{ij}(\omega) + \chi''_{ij}(\omega) \tag{2.18a}$$

$$\chi_{ij}^{em}(\omega) = \chi'_{ji}(\omega) - \chi''_{ji}(\omega). \tag{2.18b}$$

In the DC, $\omega = 0$ case, the imaginary part of the matrix element vanishes, and thus $\chi_{ij}^{me}(0) = \chi_{ji}^{em}(0)$.

The off-diagonal components of $\chi_{ij}^{me}(\omega), (i \neq j)$ determine the NDD [29, 65, 67]. The absorption difference is nothing else but a difference in the index of refraction ($N^{\pm}$) of a material for opposite directions of light propagations ($\pm\mathbf{k}$). When the sample is thin enough that the light polarization is conserved during transmission, $N^{\pm}$ can be approximated as [65, 66, 68–71]

$$N^{\pm}(\omega) \approx \sqrt{\varepsilon_{jj}\mu_{ii}} \pm \frac{1}{2}[\chi_{ij}^{me}(\omega) - T\{\chi_{ij}^{me}(\omega)\}], \tag{2.19}$$

where T stands for the time-reversal operation. The imaginary part of N proportional to the absorption coefficient α ($N = n + i\kappa$, $\alpha = 2\omega\kappa/c$) will be different for N^+ and N^-. NDD is the resultant difference in absorption for counter-propagating light beams:

$$\Delta\alpha = \alpha_{+k}(\omega) - \alpha_{-k}(\omega). \tag{2.20}$$

With application of the Kramers-Kronig relations, the static ME susceptibility can be connected to the directional dichroism spectrum as a sum rule [72]

$$\chi_{ij}^{me}(\omega = 0) = \frac{c}{2\pi}\mathcal{P}\int_0^{\infty} \frac{\Delta\alpha(\omega)}{\omega^2}\mathrm{d}\omega. \tag{2.21}$$

This sum rule states that the NDD of low-frequency (low-energy) excitations govern the static ME effect, high-energy contributions are cut off by ω^2 in the denominator.

An extreme case of NDD is the one-way transparency when the absorption vanishes for one propagation direction, but it remains finite for the opposite direction. As the ME effect can be often controlled by switching the magnetic states using electric or magnetic fields, materials showing NDD may serve as switchable optical diodes [29] or directional couplers.

Several other optical effects are also a consequence of the ME coupling. Gyrotropic birefringence (GB), for example, is the opposite rotation of polarization for counter-propagating light beams [73, 74], also an optical ME effect. Jones birefringence is induced by parallel electric and magnetic fields perpendicular to the light propagation direction results in absorption difference of ±45° light polarizations [75]. Nonreciprocal rotation of reflected light (NRR) [47] is much like the magneto-optical Kerr effect, i.e., the polarization rotation of reflected light, except it is not attributed to the net magnetization of the material. In chiral materials, natural optical activity such as natural circular dichroism (NCD) and optical rotatory dispersion (ORD), the frequency dependent rotation of the light polarization are related to the ME effect, in particular to $\chi''_{ij}(\omega)$ [76].

Chapter 3

Measurement techniques

3.1 Spectroscopy of electromagnetic radiation

Spectroscopy, in general, is the energy resolved measurement of physical properties. For example, when the light absorption is determined at a wide range of discrete frequency points, the absorption spectrum is obtained. In my thesis, I used electromagnetic radiation in a broad spectral range from microwave (RF), THz, infrared (IR) to visible (VIS) in order to study excitations in magnetic materials. I summarized the different units used in optical, infrared and RF spectroscopy in Table 3.1 together with the typical excitations appearing in the different ranges.

3.1.1 Dispersive spectroscopy

This dispersive type spectroscopy is based on the frequency selective separation of light. A grating can be useful in many instruments, e.g. in spectrographs, laser tuners, laser pulse modification, or monochromators. For spectroscopy, the intensity of the monochromatic light leaving the monochromator is measured. The frequency separation can be achieved with a prism, or with a diffraction grating. The simplest realization of a diffraction grating is a microscopic series of parallel slits or grooves, depending on whether it is a transmission or reflection arrangement. The components of white light reaching these structures, diffract (have constructive interference) at different angles determined by the individual wavelength of the components.

If α is the angle of incidence, β is the angle at which the diffracted light leaves the grating with respect to the grating's normal as depicted in Fig. 3.1, the condition for constructive interference can be written as:

$$d(\sin\alpha - \sin\beta) = m\lambda, \tag{3.1}$$

	Visible (VIS)	Infrared (IR)	Microwave (RF)
wavelength	400 – 750 nm	750 nm – 1 mm	1 mm – 1 m
frequency	700 THz – 400 THz	400 THz – 300 GHz	300 GHz – 300 MHz
wavenumber	25,000 – 14,300 cm^{-1}	14,300 – 10 cm^{-1}	10 – 0.01 cm^{-1}
photon energy	3 eV – 1.7 eV	1.7 eV – 1.24 meV	1.24 meV – 1.24 μeV
excited degrees of freedom	electron excitations	• molecular vibrations • phonons • spin-wave excitations	• molecular rotations • magnetic resonance

Table 3.1: Conversion across units in different ranges of the electromagnetic spectrum.

where d is the distance between the grooves, λ is the wavelength of the incident light, and m is an integer. Since constructive interference can happen at multiple angles, the value of m determines the order of the diffraction: at $m = 0$, light is directly reflected back or transmitted. First order diffraction happens at $m = 1$, second order at $m = 2$ and so on, as illustrated in Fig. 3.2 (a). The diffraction orders can overlap with each other in case of using broad band illumination as shown in Fig. 3.2 (b). The frequency range for which no overlap occurs, is called the free spectral range. The overlapping can be dealt with by applying high-pass optical filters to filter out unwanted frequencies, or using detectors with different sensitivity ranges.

The resolution of a diffraction grating is quantified by the resolvance, that defines the smallest resolvable wavelength difference, that is $R = \lambda/\Delta\lambda$. According to the so-called Rayleigh criterion, two wavelengths are resolved when the diffraction maximum of λ coincides with the diffraction minimum of the wavelength $\lambda + \Delta\lambda$, giving the theoretical limit for resolution

$$R = \frac{\lambda}{\Delta\lambda} = mN, \tag{3.2}$$

where N is the total number of grooves. The highest achievable resolution in instruments for a given signal-to-noise ratio is generally limited by optical aberrations, and the slit width. The angular dispersion $\Delta\beta/\Delta\lambda$, i.e. the change in

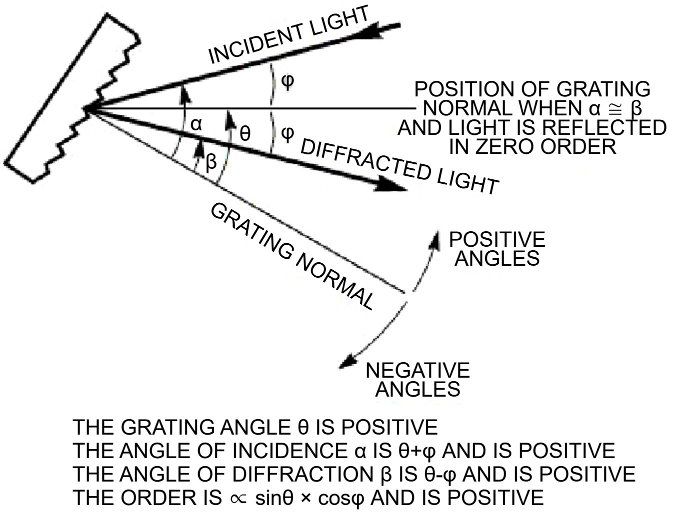

Figure 3.1: Schematic illustration of a light beam reflected from a diffraction grating, with sign conventions indicated. Figure reproduced from Ref. [77].

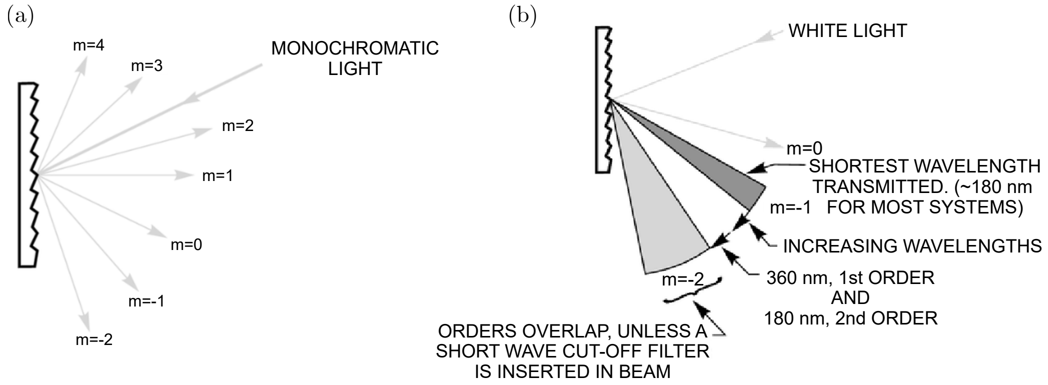

Figure 3.2: (a) Diffraction peak orders for a monochromatic light incident on a diffraction grating. (b) White light diffracted from a grating. Figure reproduced from Ref. [77].

the diffraction angle corresponding to a small change in the wavelength can be calculated by differentiating Eq. (3.1) with respect to the wavelength, assuming the angle of incidence α is fixed

$$d \cdot \cos\beta \cdot \Delta\beta = m \cdot \Delta\lambda, \tag{3.3}$$

from which

$$\frac{\Delta\beta}{\Delta\lambda} = \frac{m}{d \cdot \cos\beta}. \tag{3.4}$$

Multiplied by the output focal length, we get the linear dispersion

$$\frac{\Delta L}{\Delta\lambda} = f \cdot \frac{m}{d \cdot \cos\beta}. \tag{3.5}$$

The reciprocal (linear) dispersion is used more commonly, which gives the wavelength dispersion in nm per 1 mm (nm/mm) of the slit width ΔL. This quantity is usually listed in the properties of the grating at the blaze wavelength.

Blaze wavelength of a grating is the wavelength that is diffracted with the highest efficiency, i.e., where the diffracted light is the brightest. Absolute diffraction efficiency is the ratio of the diffracted light intensity of the incident light intensity, while relative diffraction efficiency is the absolute diffraction efficiency divided by the reflectance of the grating's coating material. The efficiency of the grating depends on the polarization of the incident light. For s-polarization, the grooves of the grating are perpendicular to the oscillating electric field of the light, and large fluctuations are present in the efficiency. For p-polarization, where the oscillating electric field and the grooves are parallel, high efficiency with little to no fluctuations can be observed.

In my measurements, I used a Newport Cornerstone 260 monochromator [77] whose optical configuration is shown schematically in Fig. 3.3, with a halogen lamp as a light source. Equipped with multiple ruled gratings, the wavelength range for my measurements was between 400 and 1700 nm.

3.1.2 Fourier transform infrared (FTIR) spectroscopy

In principle, grating spectrometers can operate at longer wavelength as well, however, they are less commonly used in the infrared range as thermal sources emit less at longer wavelength and it is inefficient to scan the spectrum step-by-step. A Fourier transform infrared (FTIR) spectrometer has the advantage of measuring at all wavelengths simultaneously which is known as Fellgett's or multiplex advantage [78]. This does not only makes measurements faster, but also more sensitive, since more scans can be averaged together to reduce noise. Another advantage of FTIR compared to grating spectrometers is their higher brightness for a given spectral

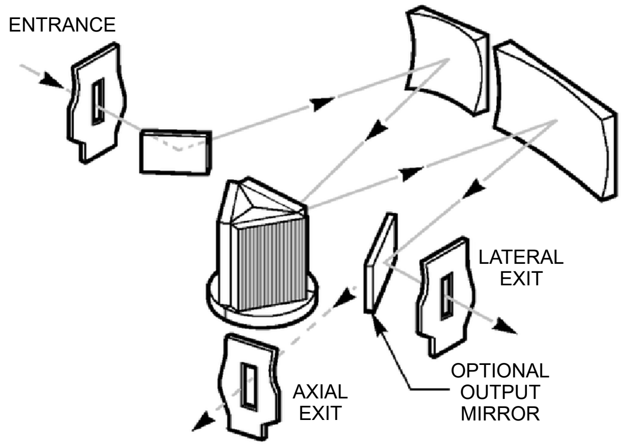

Figure 3.3: Optical configuration of the Cornerstone 260 instrument. Figure reproduced from Ref. [77].

resolution, which is the so-called Jacquinot's, or throughput advantage. Finally, as opposed to the mechanical movement of diffraction gratings, the wavelength in an FTIR is calibrated by an internal reference laser that passes through the interferometer, termed as wavelength accuracy or Connes' advantage.

A Fourier transform spectrometer is based on an interferometer. In Fig. 3.4 (a), the Michelson interferometer configuration is shown, consisting of a(n infrared) light source (*S*), whose collimated light is split by a beamsplitter (*BMS*). One beam goes to a stationary mirror (M_1), and the other to a moving mirror M_2. The reflected beams meet again at the beamsplitter with a phase (path) difference introduced by the time-delay of the moving mirror. The recombined beams interfere with each other, and this beam goes through the sample (*SP*), then gets measured by the detector *D*. The interferogram, which is the light intensity as a function of the path difference, measures the autocorrelation function of the beam.

If the light source is monochromatic (e.g. a laser), then the sum of the split beams (the interferogram) will result in a sinusoidally varying intensity at the detector as a function of path difference. In Fig. 3.4 (b), such interferograms are shown for six different frequencies. According to the Wiener–Khinchin theorem, the Fourier-transform of the auto-correlation function, i.e. interferogram is equal to the spectrum of the light source, as described by Eq. (3.6).

$$\mathcal{F}\left(\int_{-\infty}^{\infty} f(t)f^{*}(t+\tau)\mathrm{d}t\right) = |\mathcal{F}(f(t))|^2 = |\tilde{f}(\omega)|^2 \tag{3.6}$$

For a white-light source, the recombination of the time-delayed beams will result in a sinusoidally varying interference pattern for all frequency components at the

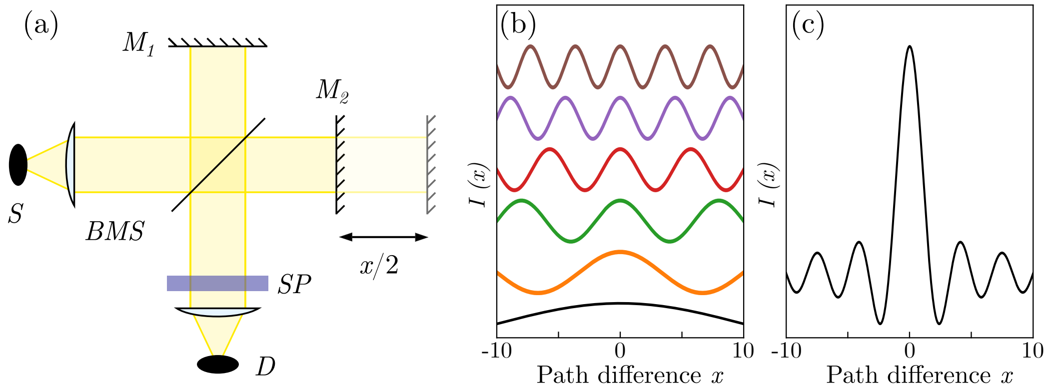

Figure 3.4: (a) Michelson interferometer of an FTIR spectrometer. The light from the source (*S*) is collimated, then split by a beamsplitter (*BMS*). The reflected part of the beam goes to a stationary mirror (M_1), the transmitted part to a moving mirror M_2. The split beam recombines again at the *BMS*, goes through the sample *SP* and then is focused on the detector *D*. (b) Interferograms from six monochromatic sources, shifted vertically for better visibility. (c) Interferogram of the sum of the frequencies on panel (b), illustrating the interferogram of a polychromatic source. Adapted from Ref. [79].

same time, and their sum will be the interferogram measured by the detector. In Fig. 3.4 (c), the interference patterns of all the frequencies shown on panel (b) are summed up, thus simulating the interferogram of a polychromatic source.

The spectral resolution of an instrument is limited by the maximum time-delay introduced by the moving mirror, meaning that instead of the integration going from $-\infty$ to ∞ in Eq. (3.6), a rectangular window from time-delay $-\tau$ to $+\tau$ is applied. This delay affects the width of absorption peaks, and thus how fine structures can be resolved. A practical method is to interpolate in frequency space, the so-called zero-padding, where zeros are added to the interferogram at large time-delays, making the rectangular window artificially wider. For the poling experiments on $LiCoPO_4$, I used a Varian 670 IR type spectrometer with an external InGaAs semiconductor detector in our laboratory in Budapest. The frequency range of the spectrometer depends on the material of the changeable beamsplitter inside. I used beamsplitters made of KBr and CaF_2, which together cover the spectral range from roughly 0.05 to 1.2 eV.

The Michelson interferometer has a number of features, that cause issues in its performance. The beamsplitter is made from a dielectric, whose efficiency goes to zero at low frequencies. The thickness of the dielectric introduces a periodic oscillation in the intensity of the interferometer output, resulting in frequency regions with zero or nearly zero intensity [80]. Furthermore, as with diffraction gratings, the efficiency of the dielectric beamsplitter differs for s and p polarization of the light as described by the Fresnel-formula [81].

A specialized FTIR spectrometer is the Martin-Puplett interferometer [82], where instead of a half-transparent dielectric mirror a wire-grid is used as a beamsplitter and the moving mirrors are rooftop mirrors instead of regular mirrors. The wire-grid polarizer is nothing else, but a series of thin metallic wires stretched at a distance d from each other. As the light reaches the wire-grid, the electric field that is parallel to the wires, induces a current along them. For this direction, the wires act as reflecting surfaces, mirrors. For the electric field that is perpendicular to the wires, they remain transparent. Rooftop mirrors are such mirrors, that flip the polarization state of a 45° linearly polarized incoming beam by 90°, where it is worth noting that pure s and p polarizations remain unaffected. These modifications allow the coverage of a wide frequency range, from below $2\,\mathrm{cm}^{-1}$ to above $100\,\mathrm{cm}^{-1}$ without varying efficiency and background levels.

The Martin-Puplett interferometer geometry is shown in Fig. 3.5. The incident light from the source S is collimated, and goes through the first polarizer, POL_1 (wires aligned [001]), after which the light is polarized along the [010] direction, meaning $\mathbf{E}^{\omega} \parallel [010]$. Then it reaches the 45°-aligned wire-grid, that serves as the beamsplitter BMS. This beamsplitter not only separates the light beam to two paths, but also separates two polarization states. The reflected part, denoted by $\boldsymbol{A}$ in Fig. 3.5, will be polarized along $[\bar{1}0\bar{1}]$. The transmitted part, denoted by $\boldsymbol{B}$, will be $[011]$-polarized. Following the path $\boldsymbol{A}$ first, it reaches the stationary rooftop mirror RM_1. These type of mirrors have two perpendicular surfaces, the edge, where they meet is called the ridge. RM_1 and RM_2 have their ridge parallel to [001]. The light that reaches the rooftop mirror, can be separated into polarization components along and perpendicular to the ridge. The component which is parallel to the ridge, stays intact upon the reflection from the two surfaces. The perpendicular component will be rotated by 180° after the reflections. Adding up the two polarization components after the reflections, the incident polarization state will be rotated by 90°. For the case of path $\boldsymbol{A}$, this means that it leaves RM_1 polarized along $[10\bar{1}]$, and goes though the beamsplitter to POL_2. Path $\boldsymbol{B}$ can be followed similarly, to then meet $\boldsymbol{A}$ after reflection from the BMS. The recombined beam passes through POL_2, then the sample (SP). Beams $\boldsymbol{A}$ and $\boldsymbol{B}$ are orthogonally polarized, and before POL_2, the recombined light is elliptically polarized because of the introduced wavelength-dependent phase difference by RM_2. The alignment of POL_2 with respect to POL_1 provides the intensity modulation at the detector. The intensity is maximal when the two polarizers are parallel, and minimal when the two polarizers are crossed.

For my magnetic-field-dependent THz absorption measurements performed on $BiFeO_3$ and on $MnSc_2S_4$, I had the opportunity to use a Martin-Puplett-type ScienceTech SPS200 spectrometer in the National Institute of Chemical Physics and Biophysics (KBFI), Tallinn, Estonia. The frequency range of the spectrometer

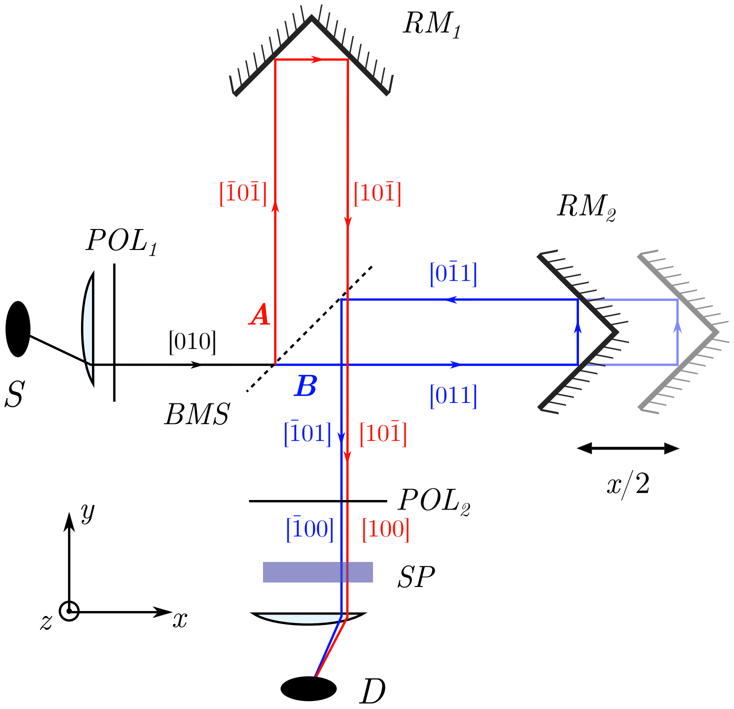

Figure 3.5: Configuration of a Martin-Puplett type FTIR setup. The light from the source (*S*) is collimated and polarized, then split by a 45°-aligned beamsplitter (*BMS*). The reflected part of the beam is colored red, and noted with *A*, while the transmitted part is colored blue, and noted with *B*. After reflection from the beamsplitter, light beam *A* goes to a stationary rooftop mirror (M_1), which rotates the polarization state by 90°. From M_1, the beam goes through the beamsplitter. Following now beam *B*, after transmission from the beamsplitter, it is reflected from a moving rooftop mirror, which, on top of rotating the polarization, also introduces a path difference *x* between beam *A* and *B*. The reflected beam *B* also gets reflected from *BMS*, and meets beam *A*. The recombined beam passes through the polarizer POL_2, and the sample *SP*, then is focused onto the detector. Adapted from Ref. [79].

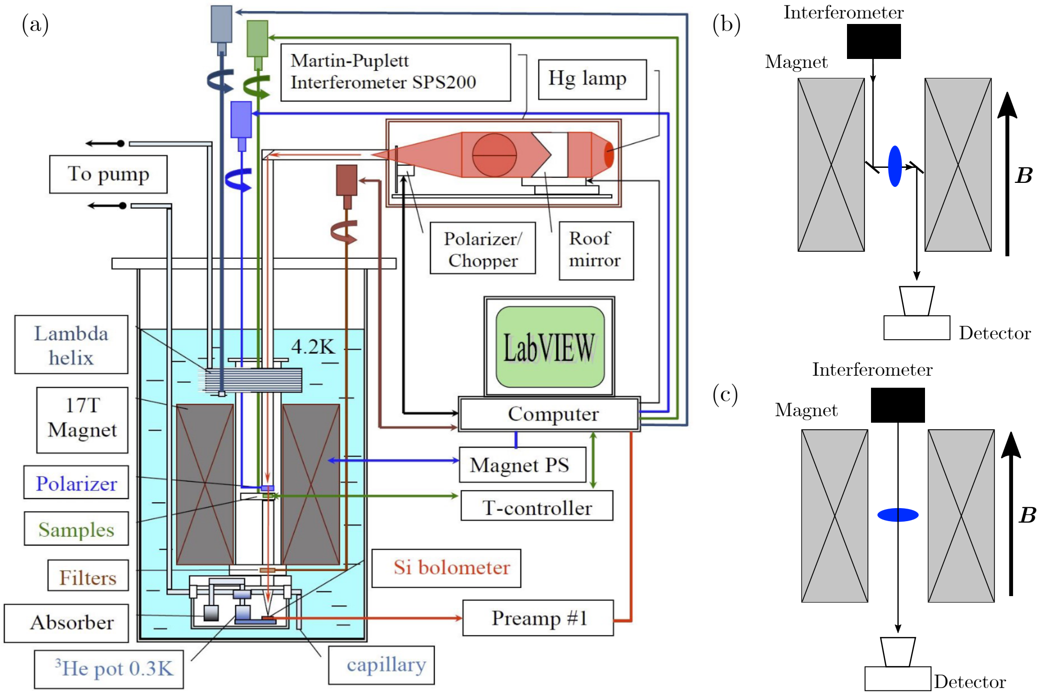

Figure 3.6: (a) Schematic drawing of the TeslaFIR setup. Magnet PS is the magnet power supply, T-controller is the temperature controller. (b) Voigt configuration with light propagating perpendicular to **B**. (c) Faraday configuration with light propagating parallel to **B**, the static field. The sample, symbolized with a blue ellipse, is at the center of the magnet. Adapted from Ref. [79].

spans from 75 GHz to 6 THz. The spectrometer can be used in two setups. One is with an Oxford TLE200 wet dilutional refrigerator, called MilliK. For my sub-Kelvin measurements on $MnSc_2S_4$, I used that system. The other setup is the so-called TeslaFIR setup, drawn schematically in Fig. 3.6 (a), with which my measurements of $BiFeO_3$ were performed. There, the light from the spectrometer is guided through a ^{4}He cryostat with a superconducting solenoid inside. The available magnetic field range goes from -17 T to 17 T, the sample temperature can be varied from 2.5 K up to even 400 K. There is also an option to apply DC voltages to the sample up to 1 kV/cm. Measurements can be performed either in Faraday or in Voigt configuration. The two possibilities are shown in Fig. 3.6 (b) for Faraday, and (c) for Voigt. In Faraday configuration, the light propagates along the static magnetic field, whereas in Voigt configuration, achieved with mirrors on the probe, the light propagation is perpendicular to the static magnetic field.

3.1.3 Data evaluation in visible and infrared experiments

The spectroscopy methods detailed above do not provide absolute measurements. The obtained signal on the detector depends on numerous factors, such as the spectrum of the source, the aperture shape, reflection from optical parts, or simply the presence of air in the light path. To be able to analyze data measured on the sample, a reference measurement is needed too. A reference can be a measurement with an empty sample holder, but based on technical constraints or desired parameter dependence, a reference can be a measurement on the sample in a specific condition, at a specific temperature or magnetic field value. The ratio of a pair of sample and reference measurement will give us the transmission (or the transmission difference)

$$\mathcal{T} = \frac{I_{\mathrm{sample}}}{I_{\mathrm{ref}}}, \tag{3.7}$$

where I_{sample} is the measured spectrum through the sample, I_{ref} is the spectrum of the reference. Assuming I_{ref} is the spectrum of an empty hole identical to the aperture at the sample, and the energy loss is dominated by the absorption in the sample, the absorbance α is obtained

$$\alpha = -\frac{1}{d}\ln\mathcal{T}, \tag{3.8}$$

where d is the sample thickness. Here, reflection losses and interferences due to multiple reflections are neglected. If the two hole shapes are not exactly the same, α will have a frequency dependent baseline. The multiple reflections inside the sample, especially if it is a plane-parallel sample, will result in an oscillation in the baseline, as a consequence of interference. From these oscillations, we can estimate the index of refraction of the sample

$$\frac{1}{n} = 2d\Delta k, \tag{3.9}$$

where Δk is the wavenumber difference of two interference maxima in the spectrum. The convention used in optics is $k = \frac{1}{\lambda}$, as opposed to $k = \frac{2\pi}{\lambda}$ used generally in solid state physics.

If the sample itself in different conditions is used as a reference, the differential absorption $\Delta\alpha$ can be calculated. For example, in a magnetic sample, a spectrum recorded above the ordering temperature, at T_{ref}, can be used as a reference

$$\Delta\alpha(T) = \alpha(T) - \alpha(T_{\mathrm{ref}}) = -\frac{1}{d}\ln\left(\frac{I(T)}{I(T_{\mathrm{ref}})}\right). \tag{3.10}$$

Alternatively, the reference spectrum can be obtained statistically from a series of for example, magnetic field dependent measurements. For that, the starting point is again, a differential absorption spectrum, in which now, a measurement at a specific field value, usually the zero-field value, serves as a reference $\Delta\alpha_B(B) = \alpha(B) - \alpha(B_{\mathrm{ref}}) = -\frac{1}{d}\ln\left(\frac{I(B)}{I(B_{\mathrm{ref}})}\right)$. After this step, negative peaks will appear in the remaining spectra at the absorption peak frequencies of the reference spectrum. This inconvenience is taken care of by creating a baseline, that is essentially the recovery of the absorption spectrum at the reference field $\Delta\alpha_0$. This can be done by either taking the minimum value of the $\Delta\alpha_B(B)$ spectra at each frequency point, or by taking the median of the set of $\Delta\alpha_B(B)$'s at each frequency point, both of these resulting in $-\Delta\alpha_0$. The final spectra are calculated as

$$\Delta\alpha(B) = \Delta\alpha_B(B) + \Delta\alpha_0. \tag{3.11}$$

The advantages of this method are, among others, is obviously that is does not require a reference hole, moreover, it can reveal weak features in the spectra. This method is not sensitive to features that are independent of the magnetic field. Additionally, this approach assumes that the resonances shift more in the field than their full width at half maximum.

3.1.4 Broadband microwave spectroscopy

If we want to probe low-energy excitations of solids, lower than the lowest provided by THz techniques, microwave techniques have to be utilized. However, microwaves have such a long wavelength, that free standing optical parts cannot be used efficiently, and the focal spot would be too large to focus on a small sample. Instead, microwaves confined in coaxial cables, waveguides or cavities are employed.

The probing of (anti)ferromagnetic resonance (A)FMR is an experimental technique, which has been utilized for a long time [83]. The magnetization of a sample is probed by the oscillating magnetic field of microwaves generated by a microwave source. In classical cavity measurements, the sample is placed in a resonant microwave cavity, which is coupled to the microwave source, creating a standing wave inside the cavity. When the (A)FMR resonance condition is met, there is a strong increase in the absorbed power. This is measured by the reduction of the reflected power. This conventional method has the obvious disadvantage of the fixed operational frequency. To have a comprehensive dataset, either a set of resonators is needed, each with a separate sample, or putting one sample into a number of resonators, which is very time consuming. These issues can be overcome with nonresonant broadband solutions. With help of a continuous microwave source and a sample put on a waveguide, broadband (A)FMR can be obtained.

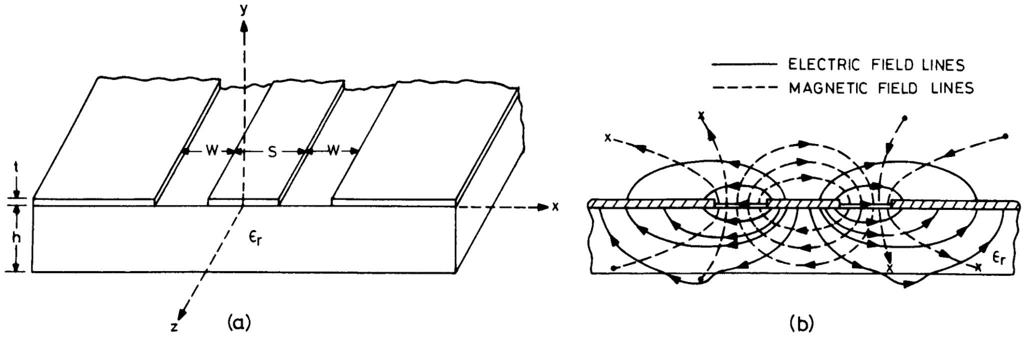

Figure 3.7: (a) A coplanar waveguide (CPW) consisting of the central signal line of width S, with two ground planes separated by W on a dielectric substrate of thickness h with dielectric constant ε_r. (b) The oscillating magnetic (dashed lines) and electric (solid lines) field lines drawn on the cross section of the CPW in panel (a). Figure reproduced from Ref. [84].

The coplanar waveguide (CPW) [85] is a type of transmission line, where the central conductor line of width S is separated from two ground planes at a distance W, all being in the same plane on a dielectric substrate with relative permittivity ε_r. The geometry is shown in Fig. 3.7 (a). In Fig. 3.7 (b), the electric and magnetic field lines are shown in quasi-static approximation. At low frequencies, the wave propagation can be approximated with a transverse electromagnetic (TEM) wave, but at high frequencies, a longitudinal component of the magnetic field exists, causing the wave propagation to be non-TEM [84]. The precise geometry of the waveguide depends on the parameters suitable for the particular measurement, but optimally the characteristic impedance of the waveguide can be set to $Z_\mathrm{c} = 50\,\Omega$ for a broad frequency range. As a rule of thumb, for measuring small samples, smaller CPW geometries are desired to maximize the filling and strength of the probing signal.

In waveguides, it is more useful to introduce scattering parameters, or shortly, S-parameters, that relate the amplitude of the incident and reflected electromagnetic waves. In microwave networks, the access lines to any component that consist of a pair of terminals are called ports. For an N-port network, where the amplitude of the voltage wave incident on port n is V_n^+, while the reflected voltage wave from port n has the amplitude V_n^-, the scattering matrix relates them as [86]

$$\begin{bmatrix} V_1^- \\ V_2^- \\ \vdots \\ V_N^- \end{bmatrix} = \mathbf{S} \begin{bmatrix} V_1^+ \\ V_2^+ \\ \vdots \\ V_N^- \end{bmatrix} = \begin{bmatrix} S_{11} & S_{12} & \dots & S_{1N} \\ S_{21} & S_{22} & & \vdots \\ \vdots & & \ddots & \\ S_{N1} & \dots & & S_{NN} \end{bmatrix} \begin{bmatrix} V_1^+ \\ V_2^+ \\ \vdots \\ V_N^- \end{bmatrix}. \tag{3.12}$$

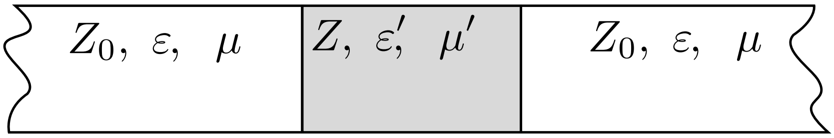

Figure 3.8: A sample put on a coplanar waveguide (CPW) can be considered as a segment of a CPW with different characteristic impedance Z, electric permittivity ε and magnetic permeability μ.

A particular element of the S-matrix can be calculated as

$$S_{ij} = \left. \frac{V_i^-}{V_j^+} \right|_{V_k^+=0;\, k\neq j}, \tag{3.13}$$

when all incident waves on all ports except on port j are set to zero. From Eq. (3.13) follows, that S_{ii} is the reflection coefficient at port i, while S_{ij} is the transmission coefficient from port j to i. From this point on, let us consider two-port microwave networks. They are used most often in practice, and enough to measure all four S-parameters for a single transmission line like a CPW. The parameter $S_{11} = \frac{V_1^-}{V_1^+}$ gives the reflected voltage, while $S_{21} = \frac{V_2^-}{V_1^+}$ will give the ratio of the incident voltage on port 1 V_1^+ transmitted to port 2 V_2^-. In an ideal case, the CPW in the network has a characteristic impedance of $Z_0 = 50\,\Omega$, thus no reflections are observable, $S_{11} = S_{22} = 0$, $S_{12} = S_{21} = 1$. A sample put on a CPW can be thought of as a lumped element put on the CPW, that will modify the impedance of the circuit to $Z(\omega)$, illustrated in Fig. 3.8. The reflection can be calculated simply with the impedances as

$$S_{11} = \frac{Z(\omega) - Z_0}{Z(\omega) + Z_0}. \tag{3.14}$$

When there is a lossy element in the circuit, the incident power will be equal to the sum of the reflected, transmitted and dissipated (absorbed) power. If the incident power is $P_{in} = \frac{(V_1^+)^2}{2Z_0}$, then with help of the scattering parameters, the power equation can be formulated as

$$P_{\text{in}} = |S_{11}|^2 P_{\text{in}} + |S_{21}|^2 P_{\text{in}} + P_{\text{abs}}. \tag{3.15}$$

If the reflection is small, Eq. (3.15) can be approximated as $P_{\text{in}} \approx |S_{21}|^2 P_{\text{in}} + P_{\text{abs}}$, which gives the absorbed power

$$P_{\text{abs}} = (1 - |S_{21}|^2) P_{\text{in}}. \tag{3.16}$$

The expression in 3.16 shows the proportionality between the scattering parameter S_{21} to the absorbed microwave power by the sample.[2]

---

[2] The same holds for S_{12}

The power balance of a microwave system can be obtained using the complex version of Poynting's theorem [87], where the electric and magnetic fields are harmonic propagating fields $\mathbf{E}(t) = \mathbf{E}e^{i\omega t}$ and $\mathbf{H}(t) = \mathbf{H}e^{i\omega t}$. Showing the power balance [88]

$$-\frac{1}{2}\oint_S (\mathbf{E}\times\mathbf{H}^*)\cdot \mathrm{d}\mathbf{S} = \frac{\sigma}{2}\int_V |\mathbf{E}|^2 \mathrm{d}V + \frac{i\omega}{2}\int_V (\mu|\mathbf{H}|^2 - \varepsilon^*|\mathbf{E}|^2)\mathrm{d}V, \tag{3.17}$$

where σ is the conductivity, μ the magnetic permeability, ε is the dielectric permittivity. On the left-hand site is the complex power flowing in the surface S. On the right-hand side, the first term corresponds to dissipated power due to ohmic losses in volume V, while the first and second part of the second term on the right-hand side show the electric and magnetic energies stored in V. Narrowing the integration volume to the sample V_S on the waveguide, the absorbed magnetic power in the sample is

$$P_{\mathrm{magn.abs}} = \frac{1}{2}\mathrm{Re}\left\{\int_{V_S} i\omega\mu|\mathbf{H}|^2\right\} = \frac{1}{2}\mathrm{Re}\left\{\int_{V_S} i\omega\mu_0(1+\chi^m)|\mathbf{H}|^2\right\}, \tag{3.18}$$

where $\mu = \mu_0(1+\chi^m)$. It can be seen from the expression in 3.18 that the absorbed power is related to the imaginary part of the magnetic susceptibility of the sample. Since the scattering parameter S_{21} is related to absorbed power, it is also connected to the magnetic susceptibility. When the resonance condition is met in a magnetic sample, more energy is stored in the sample, thus it absorbs more from the incoming power, hence S_{21} will be smaller.

A Vector Network Analyzer (VNA) is a device that allows us to measure the scattering parameters. The vector in the name indicates that the device can measure both the phase and the magnitude of the complex S-parameters. The basic working principle of a VNA can be understood with the help of a schematic figure of the device. A broadband microwave source produces the signal at frequency f, then the signal shown in Fig. 3.9 is split into two branches. One branch serves as a reference, the other goes to the device under test (DUT). The reference is locked to a local oscillator, which has frequency slightly off from the source $f+\Delta f$. The signal reflected back from the DUT is led to be collected by a directional coupler. The receiver mixes the signal of the local oscillator with the signal-to-be-measured, thus down-converting the reflected/transmitted signal to Δf, without change in the amplitude or phase. Finally, before detection, the down-converted signal goes through a bandpass filter optimized for the frequency Δf. Thus, GHz f signals are converted to sub-GHz Δf signals, that are easier to measure with low-frequency electronics.

I used broadband microwave spectroscopy to detect resonances in the absorption spectrum which correspond to the spin excitations of magnetic materials. To

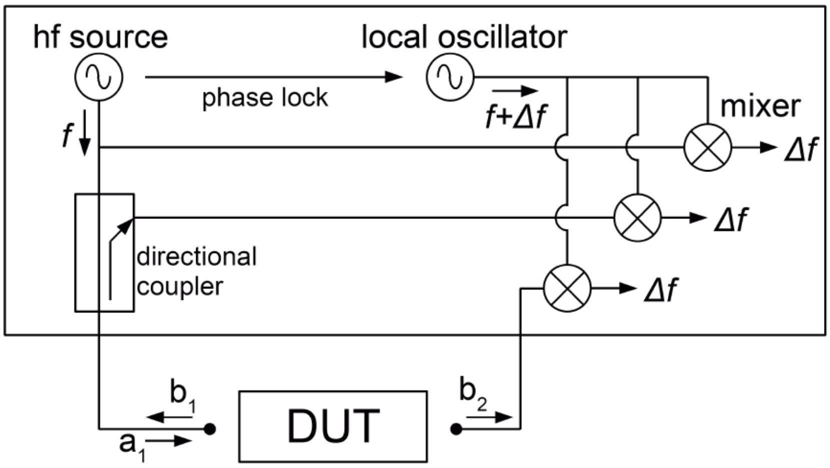

Figure 3.9: Schematic illustration of a VNA that measures only the reflection S_{11} and transmission S_{21}. A microwave signal with frequency f is generated by a high-frequency (hf) source. The incoming signal to the device under test (DUT) is denoted by a_1, the reflected signal by b_1, and the transmitted signal by b_2. S_{11} is calculated as $\frac{\mathrm{b}_1}{\mathrm{a}_1}$, and S_{21} as $\frac{\mathrm{b}_2}{\mathrm{a}_1}$. Reproduced from [89].

exemplify the microscopic processes responsible for the resonances, I discuss the magnetization dynamics in two simple, often studied cases. First, I will consider ferromagnetic resonance (FMR), the precession of the magnetization of a ferromagnetic sample around an effective magnetic field. When the frequency of the transverse RF field equals to the resonance frequency, energy is absorbed. The magnetization dynamics is described by the Landau-Lifshitz-Gilbert (LLG) equation [90, 91]

$$\frac{\mathrm{d}\mathbf{m}}{\mathrm{d}t} = -\mu_0 \gamma \mathbf{m} \times \mathbf{H}_{\mathrm{eff}} + \alpha \mathbf{m} \times \frac{\mathrm{d}\mathbf{m}}{\mathrm{d}t}, \tag{3.19}$$

where γ is the gyromagnetic ratio, $\mathbf{m}$ is the magnetization, μ_0 is the vacuum permeability, $\mathbf{H}_{\mathrm{eff}}$ is the effective magnetic field, and α is the Gilbert damping constant. The first term describes the steady-state precession of the magnetization vector, and the second term introduces the dissipative damping of the system. The effective magnetic field depends on the magnetocrystalline anisotropy, dipolar interactions and the external magnetic field, which all can have similar magnitude. These effective fields are usually derived from the free energy [23, 92], but since I will not analyze FMR signals in details I give the magnetic field dependence of the FMR for two simple cases to illustrate the effect of demagnetization. The resonance condition for a sample with negligible magnetization in the static field B_0 is [92]

$$\omega_0 = \gamma B_0. \tag{3.20}$$

When a magnetic sample is put in a magnetic field however, the magnetic field induces magnetization in the sample, which will counteract the external field. Introducing the demagnetization factor N, the effective field acting on the sample is

$$B_{\mathrm{eff},i} = B_{0,i} - N_i \mu_0 M_i, \tag{3.21}$$

where N depends on the field direction and sample shape, $i = x, y, z$. For a sphere, $N_x = N_y = N_z$. For an (xz) plate with in-plane external magnetic field B_0, $N_x = N_z = 0; N_y = 1$, the resonance condition can be written as [92]

$$\omega_0 = \gamma \sqrt{B_0(B_0 + \mu_0 M)}. \tag{3.22}$$

In case of an antiferromagnet, equations similar to 3.19 describe the precession of the sublattice magnetization. The main difference is that the exchange interaction generates a strong effective field, the exchange field B_E, which couples the sublattice dynamics. In a uniaxial easy-axis antiferromagnet, two sublattices, sublattice 1 and sublattice 2 have to be taken into consideration, with antiparallel magnetizations equal in magnitude $M = |\mathbf{M}_1| = |\mathbf{M}_2|$, which are directed by the anisotropy field $\pm B_A \hat{\mathbf{z}}$. The anisotropy field originates from an anisotropy energy density $U_K(\theta_1) = K \sin^2 \theta_1$ with θ_1 being the angle between $\mathbf{M}_1$ and $\hat{\mathbf{z}}$, K the anisotropy constant, and $B_A = 2K/M$. In mean field approximation, the exchange between $\mathbf{M}_1$ and $\mathbf{M}_2$ is [92]

$$\mathbf{B}_1(ex) = -\lambda \mathbf{M}_2; \quad \mathbf{B}_2(ex) = -\lambda \mathbf{M}_1, \tag{3.23}$$

from which B_E is defined as $B_E = \lambda M$. The equations of motion, when the static field is parallel to the easy-axis, are

$$\frac{dM_{1x}}{dt} = \gamma [M_{1y}(B_E + B_A + B_0) - M(-\lambda M_{2y})] \tag{3.24}$$

$$\frac{dM_{1y}}{dt} = \gamma [-M_{1x}(B_E + B_A + B_0) + M(-\lambda M_{2x})] \tag{3.25}$$

$$\frac{dM_{2x}}{dt} = \gamma [M_{2y}(-B_E - B_A + B_0) - (-M)(-\lambda M_{1y})] \tag{3.26}$$

$$\frac{dM_{2y}}{dt} = \gamma [-M_{2x}(-B_E - B_A + B_0) - M(-\lambda M_{1x})], \tag{3.27}$$

that can be gathered into a matrix equation, from which the solution for the resonance frequency, i.e., the antiferromagnetic resonance (AFMR) condition can be obtained [93, 94]

$$\omega_0 = \pm \gamma B_0 + \gamma \sqrt{B_A(B_A + 2B_E)}. \tag{3.28}$$

Further cases for AFMR are summarized in Ref. [95], including easy-plane AFMs.

The anisotropy field B_A used to model magnetic anisotropy, is markedly different from single-ion anisotropy quadratic in the spin component $\sim K(S^z)^2$.

3.2 Small-angle neutron scattering (SANS)

Diffraction is a fundamental tool to study periodic structures. The constructive or destructive interference of the scattered beams, resulting in the diffraction pattern, provides information about the structure and its symmetries. Scattering experiments can be carried out with different particles such as photons, electrons and neutrons, each revealing different aspects of the investigated material, and so often a combination of them are used to get a more complete picture. Different properties of the scattering methods are summarized in Table 3.2.

	photon (X-ray)	electron	neutron
mass	0	$9.1 \cdot 10^{-31}$ kg	$1.67 \cdot 10^{-27}$ kg
electric charge	0	$-e$ ($= -1.6 \cdot 10^{-19}$ C)	0
spin	$1\hbar$	$1/2\,\hbar$	$1/2\,\hbar$
interacts with	electric charge	electric charge	nucleus, magnetic moments
cost, infrastructure needs	relatively cheap, tabletop	electron microscope, dedicated laboratory	nuclear reactor or particle accelerator
element sensitivity (differential scattering cross section)	$\sim Z^2$ (small for light elements, large for heavy elements)	small for light elements, large for heavy elements	strongly isotope dependent
sensitivity	bulk	surface	bulk (+magnetic pattern)

Table 3.2: Properties of the different scattering techniques using different particles.

In my work, I used neutrons as they can be sensitive to the magnetic pattern of the studied material due to their magnetic moments shown in Table 3.2. In a general neutron scattering experiment, particles scattered into a $\mathrm{d}\Omega$ solid angle with energy between E' and $E' + \mathrm{d}E'$ are counted. To obtain material specific information, the number of scattered neutrons is normalized by the incoming particle flux. This normalized quantity, which is the the double differential cross section, can be calculated using Fermi's golden rule. If the quantum state of the studied sample changes from λ to λ' and the neutron spin changes from σ to σ' upon the scattering the cross-section has the following form [96]

$$\left(\frac{\mathrm{d}^2\boldsymbol{\sigma}}{\mathrm{d}\Omega\mathrm{d}E'}\right)_{\lambda,\sigma\rightarrow\lambda',\sigma'}=\frac{k'}{k}\left(\frac{m_n}{2\pi\hbar^2}\right)^2\mid\langle\mathbf{k}'\lambda'\boldsymbol{\sigma}'\mid V_{int}(\mathbf{r})\mid\mathbf{k}\lambda\boldsymbol{\sigma}\rangle\mid^2\delta(E_\lambda-E_{\lambda'}+E-E'). \tag{3.29}$$

Here $\mathbf{k}$ and $\mathbf{k}'$ are the wavenumbers of the incoming and outgoing neutrons, respectively, m_n is the mass of the neutron, $V_{int}(\mathbf{r})$ is the interaction potential. The Dirac delta function on the right-hand side of the formula ensures energy conservation.

In magnetic neutron scattering the magnetic moment of the neutron $\boldsymbol{\mu}_n$ interacts with the magnetic field generated by the electrons of the sample $\mathbf{B}_e$

$$V_{int}(\mathbf{r})=\boldsymbol{\mu}_n\cdot\mathbf{B}_e(\mathbf{r}), \tag{3.30}$$

where $\boldsymbol{\mu}_n=-\gamma\frac{e\hbar}{2m_n}\boldsymbol{\sigma}$, e denotes the elementary charge and $\boldsymbol{\sigma}$ represent the Pauli spin matrices, and $\gamma=1.913$.

Substituting the interaction potential (3.30) in the expression (3.29) and assuming that the incoming and outgoing neutrons are plane-waves the scattering matrix element has the form

$$\langle\mathbf{k}'\mid V(\mathbf{r})\mid\mathbf{k}\rangle=\int\mathrm{d}^3\mathbf{r}V(\mathbf{r})e^{i(\mathbf{k}'-\mathbf{k})\mathbf{r}}=-\boldsymbol{\mu}_n\int\mathrm{d}^3\mathbf{r}\mathbf{B}_e(\mathbf{r})e^{i\mathbf{qr}}, \tag{3.31}$$

where $\mathbf{q}=\mathbf{k}'-\mathbf{k}$ is the momentum transfer vector. The magnetic field $\mathbf{B}_e(\mathbf{r})$, created by the electrons can be related to the dipole moment distribution of the electrons $\mathbf{M}(\mathbf{r})$:

$$\mathbf{B}_e(\mathbf{r})=\frac{\mu_0}{4\pi}\nabla\times\int\mathrm{d}^3\mathbf{r}'\mathbf{M}(\mathbf{r}')\frac{\mathbf{r}-\mathbf{r}'}{\mid\mathbf{r}-\mathbf{r}'\mid^3}. \tag{3.32}$$

After performing the Fourier transformation in Eq. (3.31) the matrix element has the form

$$\langle\mathbf{k}'\mid V(\mathbf{r})\mid\mathbf{k}\rangle=-\mu_0\boldsymbol{\mu}_n\frac{\mathbf{q}\times[M(\mathbf{q})\times\mathbf{q}]}{\mathbf{q}^2}=\mu_0\gamma\frac{e\hbar}{2m_n}\boldsymbol{\sigma}\cdot\mathbf{M}_\perp(\mathbf{q}), \tag{3.33}$$

where μ_0 is the vacuum permeability, and $\mathbf{M}(\mathbf{q})=\int\mathrm{d}^3\mathbf{r}\mathbf{M}(\mathbf{r})e^{i\mathbf{qr}}$ is the Fourier transform of the magnetization, from which $\mathbf{M}_\perp(\mathbf{q})$ is its component perpendicular to the momentum transfer $\mathbf{q}$:

$$\mathbf{M}_\perp(\mathbf{q})=\mathbf{q}\times[\mathbf{M}(\mathbf{q})\times\mathbf{q}]. \tag{3.34}$$

Using the formula for the matrix element in Eq. (3.33) the double differential cross section has the form

$$\left(\frac{\mathrm{d}^2\boldsymbol{\sigma}}{\mathrm{d}\Omega\mathrm{d}E'}\right)_{\lambda,\boldsymbol{\sigma}\rightarrow\lambda',\boldsymbol{\sigma}'}=\left(\frac{\gamma r_0}{2\mu_B}\right)^2\frac{k'}{k}|\langle\boldsymbol{\sigma}'\lambda'|\boldsymbol{\sigma}\mathbf{M}_\perp(\mathbf{k})|\boldsymbol{\sigma}\lambda\rangle|^2\delta(E_\lambda-E_{\lambda'}+\hbar\omega), \tag{3.35}$$

where $r_0 = e^2/(4\pi\varepsilon_0 mc^2)$ is the classical electron radius, which is about $r_0 \approx 2.82\,\mathrm{fm}$, and μ_B is the Bohr-magneton.

After the summation over all possible initial states in Eq. (3.35), restricting ourselves only to elastic processes and averaging for the neutron polarizations by assuming an unpolarized beam, the formula of the cross section is

$$\begin{aligned}\left(\frac{\mathrm{d}\sigma}{\mathrm{d}\Omega}\right) &= \left(\frac{\gamma r_0}{2\mu_B}\right)^2 |\mathbf{q}\times(\langle\mathbf{M}(\mathbf{q})\rangle\times\mathbf{q})|^2 \\ &= \left(\frac{\gamma r_0}{2\mu_B}\right)^2 |\mathbf{M}(\mathbf{q})_\perp|^2.\end{aligned} \tag{3.36}$$

The picturesque meaning of this result is that the magnetic neutron scattering is only sensitive to the component of Fourier transform of the magnetization perpendicular to the momentum transfer vector **q**.

Small-angle neutron scattering (SANS) is a special variant of neutron scattering in the sense that it resolves the structures that are large compared with atomic distances (from ~1 nm to even 1 μm), hence the scattering occurs at small angles. Various branches of science use this technique, from polymer chemistry, protein complex biology, through condensed matter physics studying type-II superconductivity, to material sciences and metallurgy. In this thesis, large-scale, magnetically modulated structures are studied with SANS.

3.2.1 Practical aspects of SANS experiments

A difficult part of conducting neutron scattering experiments is to obtain a neutron beam with large enough flux, as they are not so easily available as X-ray sources. Neutrons can come from fission reactors or spallation sources. In a fission source, neutrons are generated as a result of bombarding heavy nuclei, which, in turn, will split, and emit more neutrons. This is done in a nuclear reactor for scientific research. For producing neutrons with spallation, a heavy metal target, usually mercury or lead, is bombarded with a high-energy proton beam. Following the impact, the heavy nucleus emits numerous nucleons including neutrons. A particle accelerator is needed for this type of neutron harvesting.

The high-energy neutrons produced in these processes are slowed down to have longer wavelength suitable for SANS experiments. For this, neutrons pass through a moderator (heavy water, tank of liquid hydrogen), where, by numerous collisions, they become thermal or cold neutrons following a Maxwell-Boltzmann distribution. The standard thermal neutron with $T = 293\,\mathrm{K}$, has a wavelength of 1.798 Å. Neutron energy ranges are summarized in Table 3.3.

In order to have a beam with well defined energy and momentum the beam is guided through a monochromator and multiple collimators, usually several meters

Source	Energy [meV]	Temperature [K]	Wavelength [Å]
cold	0.1 – 10	1 – 120	30 – 3
thermal	5 – 100	60 – 1000	4 – 1
hot	100 – 500	1000 – 6000	1 – 0.4

Table 3.3: Energy, temperature and wavelength ranges for different sources of neutrons. Table reproduced from [97].

long. The beam scatters on the sample and the diffracted neutrons are counted typically by ^{3}He detectors.

As the momentum transfer is inversely proportional to the real-space lengths of the investigated structure, for large periodic real-space objects, a very small scattering range has to be measured compared to regular crystallographic scattering ranges (10^{-4}Å^{-1}vs ~ 0.5Å^{-1}). For that, an instrument with good angular resolution is needed to resolve the diffraction images.

In order to meet the Bragg condition even for a periodic structure with long correlation length ξ, and to measure the correlation length corresponding to the broadening of the peaks along the beam, the scattered intensity is measured by slightly tilting the sample away from the perfect orientation. I introduce this method using Ewald's construction in the reciprocal space shown in Fig 3.10.

The Ewald sphere is a concept and a visualization tool based on the Laue condition for diffraction

$$\mathbf{k}' - \mathbf{k} = \mathbf{G}, \tag{3.37}$$

which states that the difference of the incident and the scattered beam (described by the wave vector $\mathbf{k}$ and $\mathbf{k}'$) must be a reciprocal lattice vector $\mathbf{G}$, to produce a Bragg peak.

To draw an Ewald sphere, one needs to consider the reciprocal lattice of the crystal. Then, the incident wave vector $\mathbf{k}$ is drawn on the lattice so that its tip points to a reciprocal lattice point. The starting point of $\mathbf{k}$ is the center of the Ewald sphere, whose surface contains all points that are at a distance $|\mathbf{k}|$ from the center. This sphere represents the possible final states after an elastic scattering event. All the reciprocal lattice points that this sphere intersects with, satisfy the condition in Eq. (3.37), and thus correspond to the directions where a Bragg peak emerges. In a magnetically modulated sample, where the modulation vector is $\mathbf{q}$, the condition is $\mathbf{k}' - \mathbf{k} = \mathbf{q}$. In Fig. 3.10 (a), a magnetic sample with two in-plane modulation vectors, $\mathbf{q}_1$ and $\mathbf{q}_2$ is placed perpendicular to an incoming neutron beam. As $|\mathbf{k} + \mathbf{q_i}| > |\mathbf{k}'|$ violates the principles of elastic scattering (energy conservation), the scattering is forbidden. In a perfect lattice, where the correlation length is infinite, the reciprocal lattice points and diffraction peaks are point-like objects with no extent, and the Laue condition is satisfied only for one incident beam direction. In real conditions however, where the sample has finite dimensions and the correlation lengths are also finite, the Bragg peaks broaden, and the Laue condition is satisfied for a range of incident beam directions. However, the scattered intensity decreases for an incident neutron beam perpendicular to $\mathbf{q}$. To enhance the intensity of the diffraction peaks, the sample is rotated by a few degrees step-by-step around the vertical [Fig. 3.10 (b)] and horizontal [Fig. 3.10 (c)] axes, and the intensity is collected in each step. This way, the relative orientation of the incident beam and the crystallographic axes are changed, allowing for scattering on the whole finite Bragg peak. This technique is called sample rocking. The images recorded upon the rocking procedure are then added up, and the result is the scattering image. The measured intensity as a function of the rocking angle is called a rocking curve. In neutron facilities, SAN rocking means rotating around the vertical axis, measured as the polar angle ψ in Fig. 3.10 (b), while PHI rocking is rotating around the horizontal axis, measured as the azimuthal angle φ in Fig. 3.10 (c).

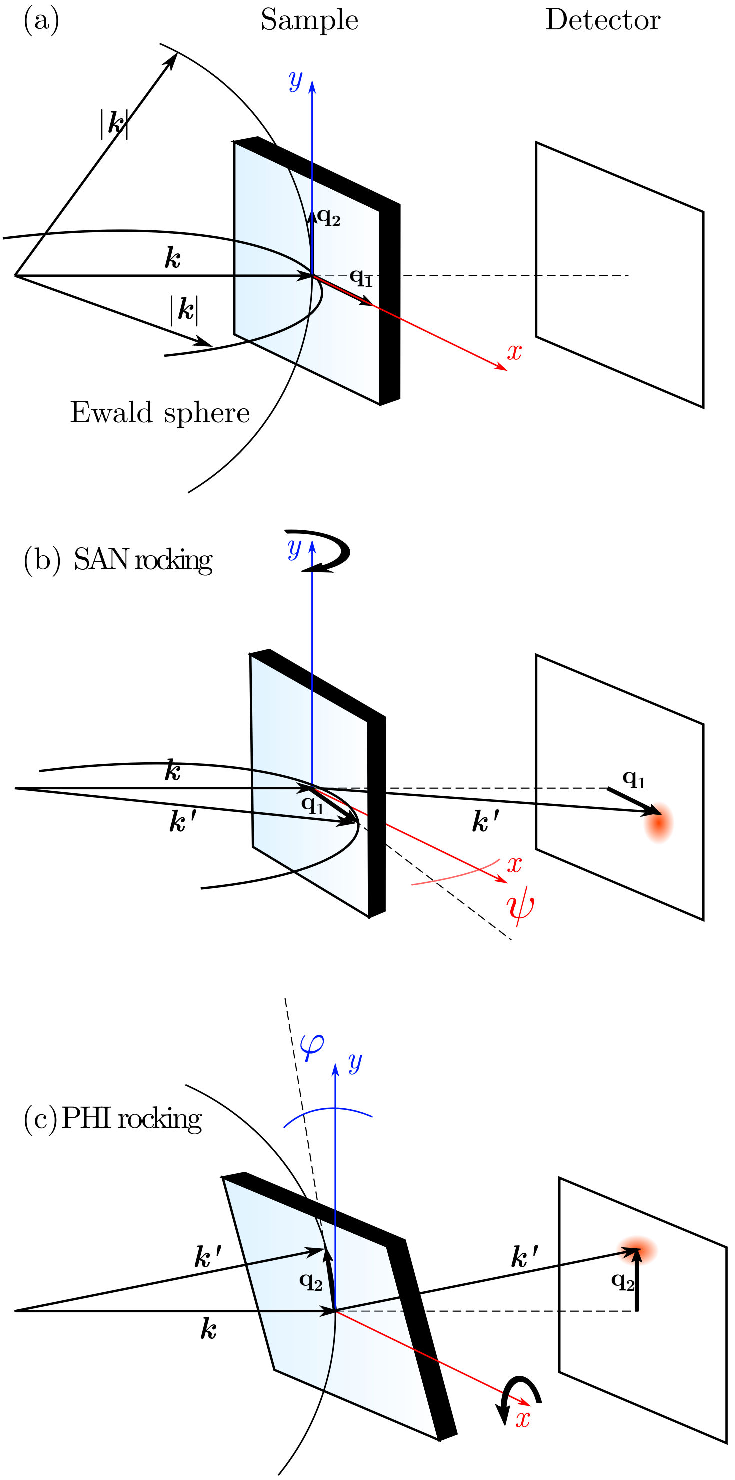

Figure 3.10: (a) Illustration of Ewald's sphere. The surface of the sphere contains all possible scattered wavevector directions. Touching the Ewald's sphere is magnetically modulated sample with two in-plane modulation vectors, $\mathbf{q}_1$ and $\mathbf{q}_2$. (b) SAN rocking, i.e. rotating around the vertical axis, to match the horizontal modulation vector $\mathbf{q}_1$ to the Ewald's sphere. (c) PHI rocking, i.e. rotating around the horizontal axis, to match the vertical modulation vector $\mathbf{q}_2$ to the Ewald's sphere. Figure adapted from Ref. [98].

Chapter 4

Non-reciprocal light absorption in the antiferromagnetic $LiCoPO_4$

Detecting antiferromagnetic (AFM) domains has been a challenge right from the discovery of antiferromagnets [31, 99]. Due to the compensated nature of the magnetic structure, these materials are resistant to stray fields, but also hard to detect with optical methods or probing with magnetometers. There exist however, techniques, that can serve with spatial information about AFMs [32], such as second harmonic generation (SHG) [100–102], spin-polarized scanning tunneling microscopy (SP-STM) [103–106], magnetic force microscopy (MFM) [107], X-ray magnetic linear dichroism with photo-emission electron microscopy (XMLD-PEEM) [13, 108, 109], nitrogen-vacancy (NV) diamond based scanning probe microscopy [106, 110, 111], or Lorentz transmission electron microscopy (L-TEM) for long-wavelength modulated structures [112, 113].

Magneto-optical (MO) studies, that can probe the AFM order both spatially as well as temporally are based on linear optical effects described by the dielectric permittivity tensor ε_{ij} [114]. In AFM's, even without net magnetization the ordering of the spins breaks rotational symmetries of the paramagnetic state leading to linear birefringence and dichroism, corresponding to anisotropies in the symmetric part of ε_{ij}. These optical effects are quadratic in the AFM order parameter, and they are not sensitive to the reversal of the spins. The MO Faraday and Kerr effects, which depend on the antisymmetric part of ε_{ij}, are usually proportional to the magnetization, thus, absent in the ground state. However, they can be utilized to probe the magnetization dynamics induced by an external stimulus [115–117].

A nonlinear effect quadratic in the electric field $\mathbf{E}$ of the incident light is a powerful technique to detect AFM domains. In this process, two incident photons with frequency ω create a photon with double frequency, 2ω. This phenomenon is termed as second-harmonic generation (SHG). Macroscopically, the second order non-linear susceptibility χ_{ijk} describes this phenomenon

$$P_i^{\omega} = \chi_{ijk} E_j^{\omega} E_k^{\omega}, \tag{4.1}$$

where **P** is the induced polarization and the **E** is the electric field of light. From the expression in 4.1 it is clear that SHG is allowed only when the inversion symmetry is broken [118]. As the intensity of the SHG signal depends on the amplitude of the incident electric field, to obtain good signal-to-noise ratio, a powerful laser is needed. With this method, the AFM domains of LiCoPO$_4$ were identified [101, 102].

When a magnetic order simultaneously breaks time-reversal and inversion symmetries, the ME effect becomes allowed. The measurement of the ME susceptibility tensor χ_{ij}^{me} gives information about the orientations, as well as the sign of the AFM order parameter, as shown for example in Cr$_2$O$_3$ [24, 119, 120]. Furthermore, the mixing of electric and magnetic dipole excitations through the ME effect provide further possibilities to detect and image AFM domains. Such effects were used by imaging the spatial variation of the nonreciprocal linear dichroism in Pb(TiO)Cu$_4$(PO$_4$)$_4$ [121], and the electric field-induced magnetic circular dichroism in Cr$_2$O$_3$ [47]. Additionally, nonreciprocal directional dichroism (NDD), the absorption difference for counter-propagating beams, can be used to image domains, when the corresponding magnetic states are connected via time-reversal symmetry.

LiCoPO$_4$ is widely studied by chemists as a cathode material for high-voltage lithium ion batteries [122–124], but also is an antiferromagnet, that hosts two types of AFM domains. Since the AFM order breaks the inversion symmetry, LiCoPO$_4$ becomes magnetoelectric below its Néel temperature with one of the largest ME coupling coefficient known. I performed spectroscopic experiments in the visible and near infrared range, and found a large absorption difference between the two AFM domains of LiCoPO$_4$ (NDD). Then I utilized this difference to image domains. In this chapter, I am going to present my spectroscopic studies on LiCoPO$_4$ and discuss the results of the imaging.

4.1 Structural and magnetic properties of LiCoPO$_4$

LiCoPO$_4$ belongs to the family of orthophosphates. Just like other members of this family, it crystallizes in the orthorhombic olivine structure (space group *Pnma*) [125], shown in Fig. 4.1 (a). The crystallographic a, b and c axes are labeled as x, y and z axes in this work. The magnetic Co^{2+} ions, occupying mirror plane sites with Wyckoff positions 4h, are coordinated by distorted octahedra of oxygen atoms. The low symmetry of the Co sites (C_S) allows a local electric dipole moment, however, the net polarization vanishes due to compensation in the unit

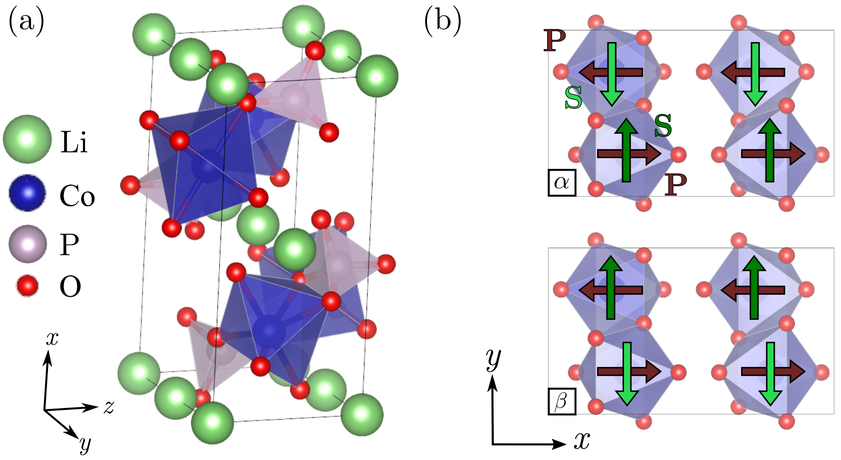

Figure 4.1: (a) Olivine crystal structure of LiCoPO$_4$. (b) The two types of antiferromagnetic domains in LiCoPO$_4$, labeled with α and β. Spins on the Co^{2+} sites are noted with green arrows, while local polarization is symbolized by brown arrows. Panel (b) is adapted from Ref. [48].

cell containing 4 sites [48]. Below $T_\mathrm{N} = 21.8\,\mathrm{K}$, the $S = 3/2$ spins of the Co^{2+} ions order into a two-sublattice collinear antiferromagnetic (AFM) structure, where spins are parallel to the y axis [126], as illustrated in Figs. 4.1 (b) and 4.2. The magnetic ordering modifies the overall symmetry to be consistent with $Pnma'$ [127–129]. In the AFM phase, the inversion and time-reversal symmetries are simultaneously broken, thus the ME effect is allowed [127, 130].

Despite the lack of total polarization in the unit cell, the linear ME susceptibility tensor in LiCoPO$_4$ has two, rather large nonvanishing terms: $\chi^{me}_{xy}/c = 15\,\mathrm{ps/m}$ and $\chi^{me}_{yx}/c = 32\,\mathrm{ps/m}$, where χ_{ij} components are divided with the speed of light c [26, 130]. The origin of the ME effect in LiCoPO$_4$ is explained with the non-zero ferrotoroidal moment that is also allowed in the $Pnma'$ symmetry [127–129]. The ferrotoroidal moment, as explained in Chapter 2, is the cross-product of local electric and magnetic polarizations, which, in the case of LiCoPO$_4$, add up to a finite value in the unit cell. Neutron scattering experiments revealed a small, 4.6°, uniform canting of the spins from the y axis [131], lowering the symmetry and allowing finite χ^{me}_{xz} and χ^{me}_{zx} components in the ME susceptibility tensor, nevertheless, these effects are small and most of the time can be neglected [101, 127, 128].

There are two possible AFM domains in LiCoPO$_4$, which are differentiated from each other by the direction of the ferrotoroidal moment pointing along the $\pm z$ direction, shown in Fig. 4.1 (b). These domains are both spatial inversion and time-reversal pairs of each other, i.e., they can be transformed to each other

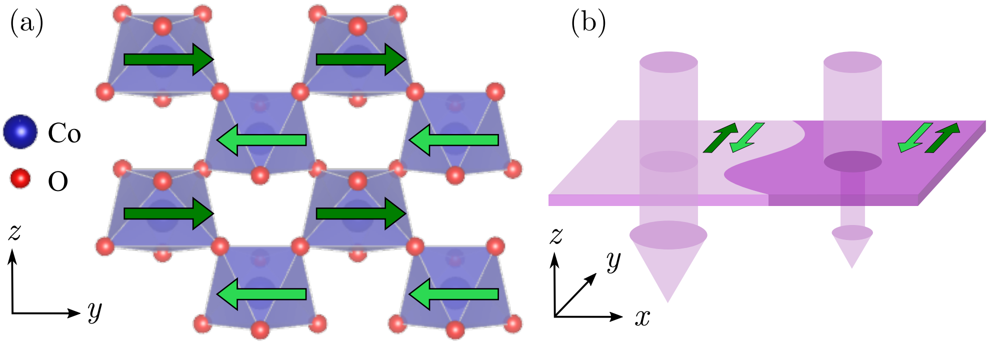

Figure 4.2: (a) Crystal and magnetic structure of LiCoPO$_4$ as viewed from the x direction. Lighter and darker green arrows represent spins on one or the other antiferromagnetic (AFM) sublattice. (b) Illustration of absorption difference of the two time-reversal pair AFM domains.

by either inversion or time-reversal operations. As these operations reverse the sign of the ME susceptibility, the domains have ME response with opposite sign [48, 130, 132]. As a result of the ME coupling, the free energy of one of the AFM domains can be lowered compared to the other with the application of both the corresponding magnetic and electric fields upon cooling through T_N. The free energy difference is $\Delta F = 2\chi_{ij}E_iH_j$. This process is referred to as ME poling, and with the help of this procedure, a single AFM domain can be stabilized [48]. For poling LiCoPO$_4$, relatively small fields are sufficient: $E_y \approx 1$ kV/cm and $B_x \approx 100$ mT are enough to select one domain. Furthermore, the switching of the AFM domains near the Néel temperature was also demonstrated in Ref. [133], where the authors described the connection between the coercive fields and the sample temperature as $(EH)_C \sim (T_N - T)^{3/2}$ when $\mathbf{B} \parallel x$.

For my experiments, I used single crystals of LiCoPO$_4$ grown by V. Kocsis using the floating zone method [134]. For the microscopy measurements, the sample was polished to the appropriate surface quality by D. Vieweg at the University of Augsburg.

4.2 Optical spectroscopy in LiCoPO$_4$

I performed optical spectroscopy on LiCoPO$_4$ in a broad frequency range, using a Newport Cornerstone 260 diffraction grating spectrometer and a Varian 670 Fourier-transform infrared spectrometer in an Oxford continuous flow optical cryostat. I explain the basic principles of the spectroscopic instruments in Chapter 3. The most interesting effect I studied in these experiments was NDD, which appears, when the light propagation vector $\mathbf{k} \parallel z$ [48], thus, samples were xy cuts, and the light propagation was perpendicular to the plane.

The spectra are obtained by measuring the transmission for a sample and a reference hole above the Néel temperature, at $T = 30\,\mathrm{K}$, and below T_N at the lowest temperature, 5 K, then calculating α as described in Chapter 3. I recorded the absorption spectra of the two AFM domains in LiCoPO$_4$ between 0.08 eV and 3.1 eV. For the poling, I used fields with magnitude $\mathbf{B} = \pm 200\,\mathrm{mT}$ and $\mathbf{E} = \pm 1\,\mathrm{kV/cm}$, and directions $\mathbf{B} \parallel x$, $\mathbf{E} \parallel y$. The selected domain was identified by the sign of the product of the poling field values. The incoming light was linearly polarized, set to be parallel to one of the main crystallographic axes $\mathbf{E}^\omega \parallel x$ or $\mathbf{E}^\omega \parallel y$. Figure 4.3 summarizes my main achievements: the absorption spectra of LiCoPO$_4$ for the two domains. On panel (a), the spectra of the two domains are plotted blue and green for incident light polarization $\mathbf{E}^\omega \parallel x$, red and yellow lines are absorption spectra for incident light polarization $\mathbf{E}^\omega \parallel y$. I measured the absorption spectra in all four combinations of the poling fields, and found that the spectra corresponding to the same domains overlap within the experimental noise. A series of absorption peaks can be observed on panel (a), which, between 1.55 eV and 3 eV are in accord with the reports of Ref. [135]. There are two very sharp and very strong absorption peaks at low energies, at $\sim 80\,\mathrm{meV}$ and $\sim 120\,\mathrm{meV}$, where the sample becomes completely opaque.

On panel (b) of Fig. 4.3, the absorption difference $\Delta\alpha$ of the two domains in the same polarization is plotted. This difference is essentially the NDD signal, i.e., equivalent to the absorption difference for a single domain for light propagation $\pm\mathbf{k}$, since the two AFM domains are the time-reversed pairs of each other as explained above [29, 48, 129]. I observed the strongest NDD for light polarization $\mathbf{E}^\omega \parallel y$ at 0.776 eV, which corresponds to the wavelength of 1597 nm, that is in the vicinity of the telecommunication wavelength of 1550 nm. At 1550 nm, there is a strong NDD effect as well. The absorption difference can be quantified following Ref. [137] as $|\Delta\alpha/\alpha_0|$ [%], where $\alpha_0 = \alpha_\mathrm{dom1} + \alpha_\mathrm{dom2}$. In this definition, 100% corresponds to true one-way transparency. For the 0.776 eV absorption of LiCoPO$_4$, it results in $|\Delta\alpha/\alpha_0| = 34\,\%$ [P1], which is among the largest observed NDD in the near infrared range [137].

The observed absorption peaks are in agreement with the crystal field excitations of Co^{2+} ions coordinated by distorted oxygen octahedra reported in former publications [135–137]. The energy level scheme based on crystal field splitting calculations is presented in Ref. [136]. The lowest-lying excitations in the spectra, which originate from the split ^{4}F term are presented in Fig. 4.3 (a). These excitations are predicted to be at 0.08, 0.16, 0.64, 0.65, 0.95 and 1.59 eV, which correspond well with the actual absorption positions at 0.08, 0.12, 0.6, 0.7, 0.95 and 1.6 eV. It cannot be excluded though, that the lowest-lying excitations at 0.08 and 0.12 eV may be ascribed to infrared active phonon modes. The two weaker features

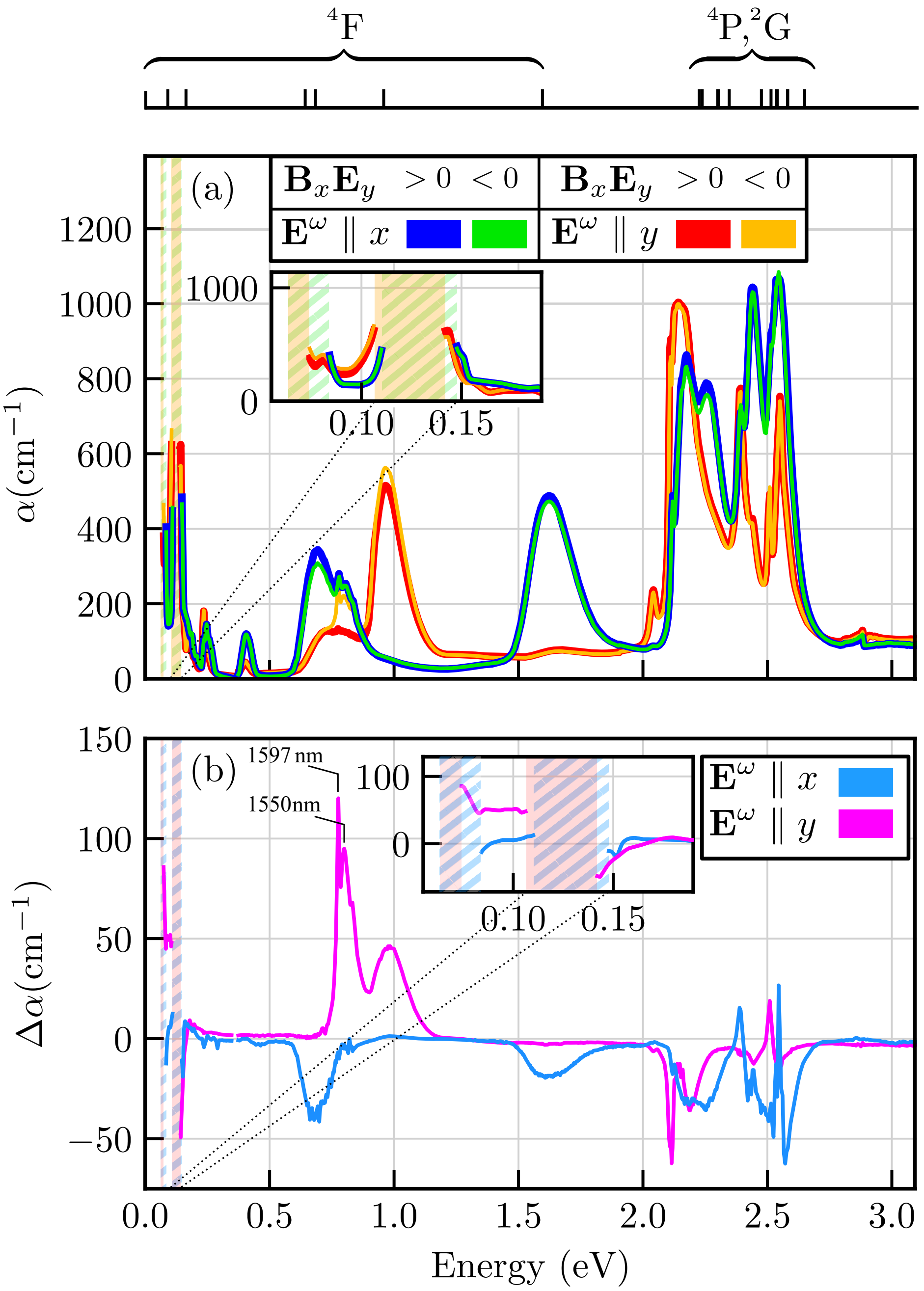

Figure 4.3: (a) Absorption spectra of the two domains in LiCoPO$_4$ for two polarizations: $\mathbf{E}^\omega \parallel x$ plotted with blue and green, and with red and orange for $\mathbf{E}^\omega \parallel y$. The two domains are selected with the combination of poling fields. The product $\mathbf{B}_x\mathbf{E}_y > 0$ selects one domain, and $\mathbf{B}_x\mathbf{E}_y < 0$ selects the other. On top, the excitations predicted by crystal field calculations [136] are shown. (b) Absorption difference of the two AFM domains for light polarizations $\mathbf{E}^\omega \parallel x$ (blue) and $\mathbf{E}^\omega \parallel y$ (magenta). The largest absorption differences are at 0.776 eV (1597 nm) and at 0.8 eV (1550 nm).

appearing at 0.25 and 0.4 eV may come from impurities as they do not overlap with the crystal field calculations. Calculated transitions to the higher-energy ^{4}P and ^{2}G terms are consistent with the series of absorption peaks observed between 2 and 2.6 eV, however, the assignment of the specific fine structure in this range is a difficult task because of overlapping transitions and the numerous excitations close in energy predicted by the crystal field model.

The C_S symmetry of the Co^{2+} sites, namely a single mirror plane normal to the y axis, introduces a selection rule to the above discussed excitations [136]. Taking the weak spin-orbit limit, a parity label belongs to the wavefunctions, as they either preserve or change sign under mirror symmetry. These wavefunctions transform according to the A' and A'' irreducible representations of C_S, respectively. The $\mathbf{E}^{\omega} \parallel y$ oscillating electric field excites transitions between states with different parity (as this polar vector is normal to the mirror plane), thus it transforms as A''. An electric field oscillating perpendicular to y induces parity-conserving transitions corresponding to A'. According to calculations in Ref. [136], the 0.08, 0.6 and 1.6 eV excitations are active for $\mathbf{E}^{\omega} \parallel x$, while transitions at 0.12, 0.7 and 0.95 eV are excited by $\mathbf{E}^{\omega} \parallel y$. The two lowest-lying excitations have too high intensities to draw any conclusions, the other four excitations follow the dipole selection rules in the sense that their intensity is strong in the allowed polarization. For the orthogonal directions however, the cancellation is not complete. Moreover, the absorption peak at 0.7 eV has a large spectral weight for $\mathbf{E}^{\omega} \parallel x$ as well, that may happen due to spin-orbit mixing.

The non-centrosymmetric local environment of the Co^{2+} site makes its crystal field excitations good candidates for emergence of NDD at simultaneously electric and magnetic dipole active transitions [138–140]. $\mathbf{E}^{\omega}_x$ and $\mathbf{B}^{\omega}_y$ belong to the irreducible representation A', while $\mathbf{E}^{\omega}_y$ and $\mathbf{B}^{\omega}_x$ belong to the irreducible representation A'' of the site symmetry, meaning that when a transition is electric dipole active, the corresponding magnetic field component can also excite it. Most importantly, the electric and magnetic field components that transform the same way are perpendicular to each other, thus can be considered as the electric and magnetic component of an electromagnetic wave (light). Thus when light is shone on the sample, both of the electric and magnetic components couple to the transitions in the studied geometry. From these symmetry considerations we can explain the emergence of NDD in $LiCoPO_4$, however, to explain the absorption strengths and the magnitude of the NDD signal, microscopic model calculations that include spin-orbit coupling are needed, which was not in the scope of my experimental work.

4.2.1 Imaging of AFM domains based on NDD

I utilized the absorption contrast of the AFM domains, i.e. the NDD around 0.776 eV to visualize them. For that I used a laser diode with the wavelength of

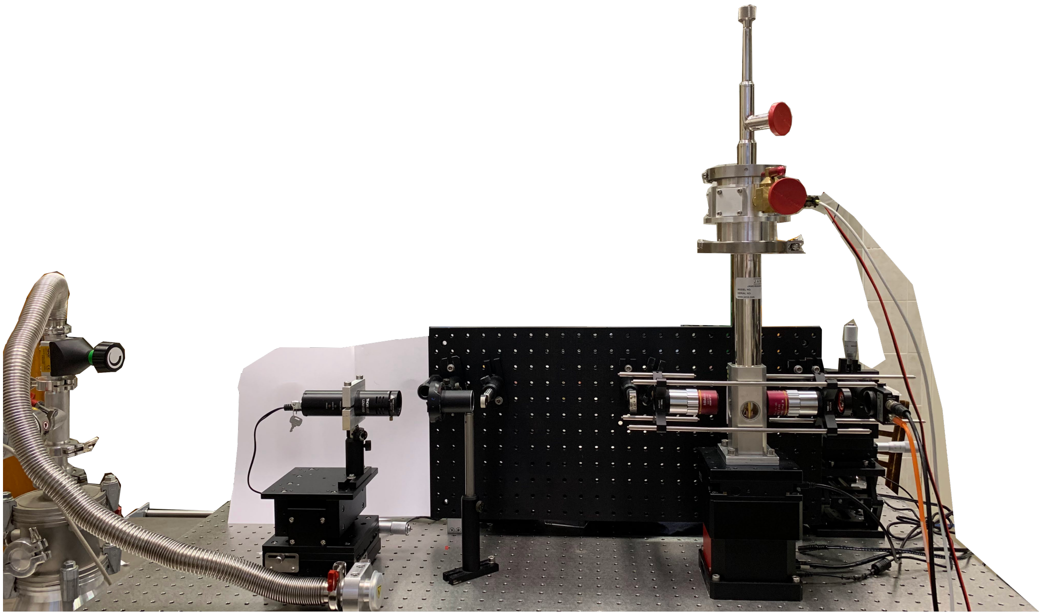

Figure 4.4: The setup used for imaging the 180° antiferromagnetic domains of $LiCoPO_4$. From left to right: The 1550 nm laser source, a polarizer, two lenses that act together as a beam expander, to illuminate completely the entrance pupil of the next component, the long working distance objective. Then the optical cryostat with the sample inside. The laser beam is focused onto the sample, and the transmitted light is collected with another long working distance objective, then focused onto a semiconductor detector with a lens. The cryostat is fixed to motorized stages that move in the x, y and z directions, achieving the movement of the sample in the focus.

1550 nm (0.8 eV) as a light source, with $\mathbf{E}^{\omega} \parallel y$ polarization, since those are the parameters at which the absorption contrast is the largest. The light beam was focused onto the sample, and then the transmitted beam was collected with long working distance objectives (MY10X-823 Mitutoyo Plan Apochromat Objective), as shown in Fig. 4.4. The spotsize in the focus was 4 μm. The transmitted intensity was collected with an InGaAs detector. An image was recorded pixel-by-pixel in a raster fashion, where the transmitted intensity at one position of the focused beam on the sample corresponded to one pixel. The position of the focused laser light was fixed, and the sample was moved by motorized stages in the focal plane. The detector had a slow drift, which was compensated by subtracting the value of the first datapoint of each row, where the aperture of the sample holder covered the laser beam, and only a background voltage was measured..

Images were recorded at 300 K and after zero-field cooling (ZFC) at 5 K, shown in Fig. 4.5. In the image taken at room temperature [Fig. 4.5 (a)], the topographic features of the sample can be observed, that serve as a baseline, or reference to the low-temperature images. Compared to that, in Fig. 4.5 (b), which was taken at 5 K, lighter and darker shaded regions appear, showing lower and higher absorbing areas in the sample. These regions correspond to the emergent AFM domains in the magnetically ordered phase below T_{N}. I highlighted the domains by marking the changes in the intensity in Fig. 4.5 (c). Based on the ZFC image, the typical domain size is a few 10 μm, smaller than reported formerly in Refs. [101, 102, 128].

This transmission microscopy experiment proved its potential to map the two AFM domains in the bulk $\mathrm{LiCoPO_4}$. It is a simpler approach to tackle the problem of visualizing AFM domains than SHG, that requires an intense laser source. However, SHG probes a three-index tensor, providing more information on the magnetic symmetry. Interestingly, the mmm' symmetry forbids some elements in the SHG tensor that appear to have small, but finite values below T_{N} [101, 102, 128]. A reduced symmetry would increase the number of domains, however, with my imaging technique based on NDD, I could not distinguish them unambiguously.

Experimenting further, I also recorded transmitted intensity images after poling in magnetic fields only. The magnetic field was applied with a permanent magnet as $\mathbf{B} \parallel y$ with a magnitude of 55 mT. I took images in zero-field after poling with $+55$ mT and -55 mT, but with zero electric fields. The results are shown in Figs. 4.6 (a) and 4.6 (b), respectively. These images are surprising, as a large area of the sample was turned into a single AFM domain, corresponding to the lighter region in Fig. 4.6 (a) and the same region but darker in Fig. 4.6 (b). In smaller patches the intensity is reversed, suggesting that a single monodomain state is not reached over the entire thickness of the sample. This partial control of AFM domains is consistent with the findings of J.-P. Rivera [141], who observed butterfly-shaped $\mathbf{P}-\mathbf{H}$ loops in the vicinity of T_{N}. He ascribed the selection of domains to the

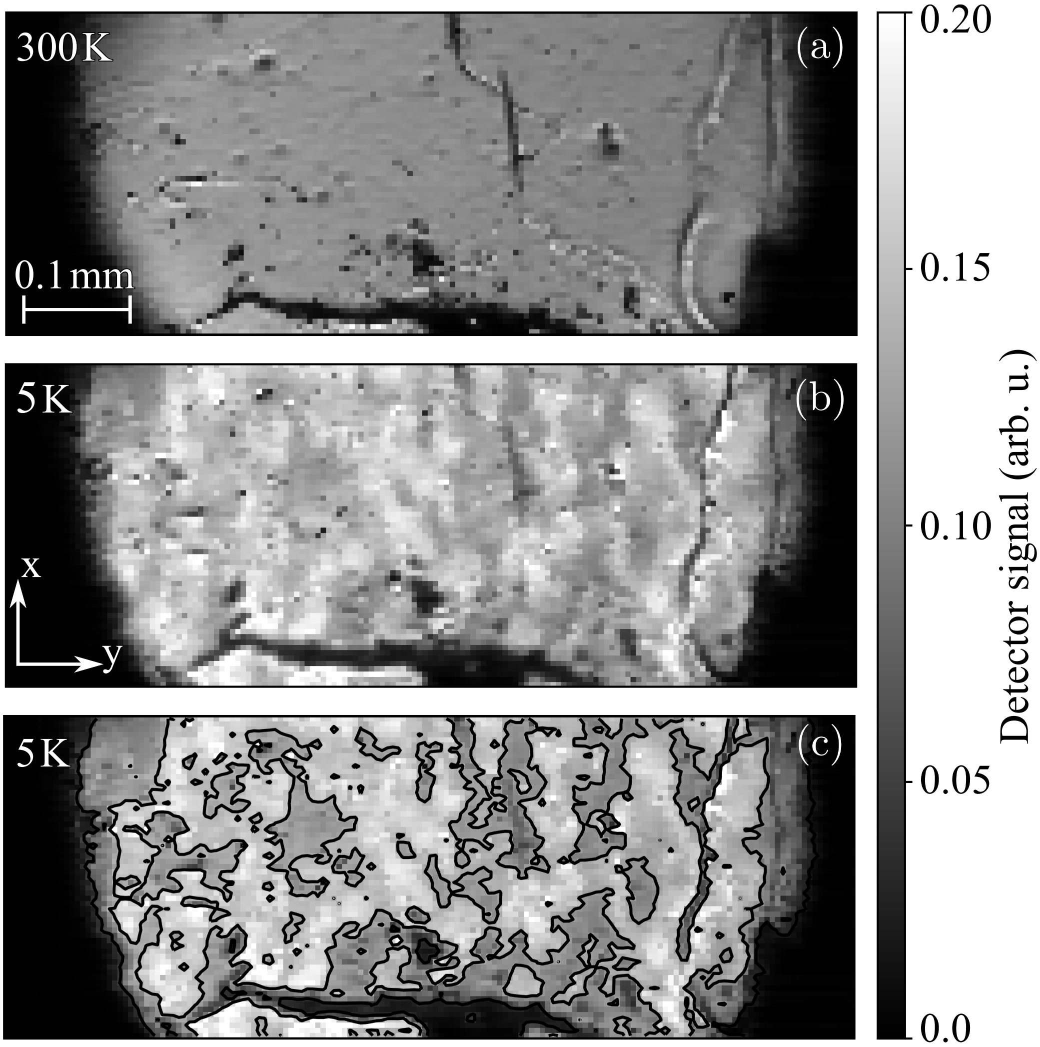

Figure 4.5: Transmission microscopy images of $LiCoPO_4$ taken with a laser with wavelength of 1550 nm. (a) Image taken at $T = 300\,\mathrm{K}$, at which temperature the material is paramagnetic. (b), (c) Images recorded at $T = 5\,\mathrm{K}$, after zero-field cooling. The lighter and darker regions stem from the antiferromagnetic domains absorbing less and more light according to the spectra in Fig. 4.3. On panel (c), black lines are drawn between less and more absorbing regions as a guide to the eye.

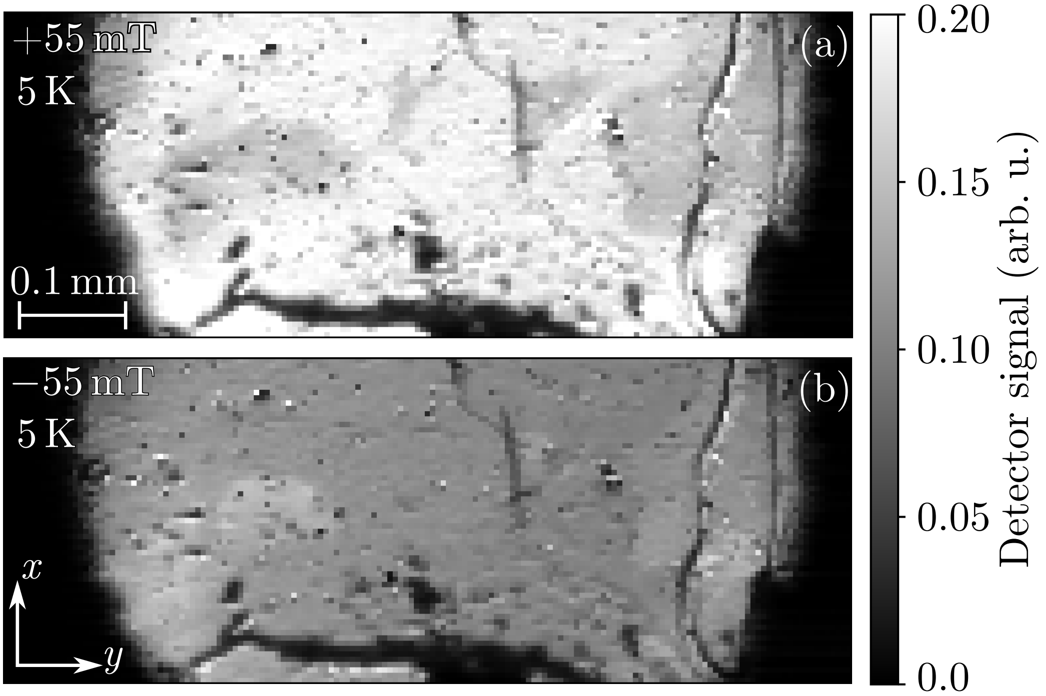

Figure 4.6: Transmission images of $LiCoPO_4$ taken at 5 K cooled in (a) magnetic field of +55 mT and in (b) magnetic field of −55 mT. Partial domain stabilization was achieved.

combination of surface charges and the external magnetic field. In the case of my imaging experiments though, surface charge accumulation can be discarded, since the sample was directly grounded by the DC power source through the electrical contacts used for poling. Neutron diffraction experiments [131] mentioned earlier in this chapter suggested that weak ferromagnetism can be consistent with the small rotation of the moments away from the *y* axis, might also cause the observed magnetic field effects in my experiments. This explanation however is contradictory with the fact that if the paramagnetic state possesses spatial inversion symmetry, linear coupling between the axial vector of the ferromagnetic moment and the inversion-symmetry-breaking AFM order parameter is not possible. Thus, the origin of the effect I observed remains open for further investigations.

4.2.2 Summary

The study of the absorption spectrum of the AFM domains of $LiCoPO_4$ was a rewarding project. The optical absorption spectra recorded in the infrared and visible ranges revealed an absorption difference between the two time-reversal-pair AFM domains of $LiCoPO_4$ as high as 34 % at 0.776 eV (1597 nm). This large

NDD near the telecommunication wavelength of 1550 nm can be ascribed to the crystal-field excitations of the Co^{2+} ions. This experiment makes an addition to the list of transition metal ions that enable large NDD, preferred from the point of view of applications, e.g., for optical components like isolators or switchable optical diodes [29, 137]. Furthermore, I utilized this absorption difference to visualize AFM domains. The use of a transmission microscopy setup that I assembled may simplify the mapping of AFM domains in various ME materials.

Chapter 5

Magnetic phases of $BiFeO_3$ and their spin excitations at and above room temperature

One of the most studied magnetoelectric multiferroics is $BiFeO_3$. This exceptional interest owes to the fact that it has multiferroic properties even at room temperature, making it a promising candidate for applications. Despite the many research conducted on $BiFeO_3$, its relatively simple magnetic phase diagram has recently been extended at around room temperature [143]. A new, high-temperature field-induced magnetic phase was discovered showing an unusually high magnetoelectric susceptibility. To utilize the potential of this phase, however, one needs to observe and understand its characteristics. In this chapter, I present my experiments at high temperatures, namely, at and above room temperature, to study the newly introduced magnetic phase. I carried out SANS experiments to study the magnetic-field induced changes in the magnetic structure, and THz absorption spectroscopy to characterize the spin excitations in this part of the phase diagram.

5.1 Structural and magnetic phase transitions in $BiFeO_3$

$BiFeO_3$ crystallizes below 1300 K in a cubic perovskite crystal structure (space group $Pm\overline{3}m$) [144]. The material is paraelectric down to $T_C = 1100\,K$, where a first order ferroelectric phase transition occurs [145]. This transition is accompanied by distortions in the crystal structure: Bi and Fe cations shift along the pseudocubic [111] direction, as illustrated with orange and blue arrows in Fig. 5.1. At the same time, the oxygen octahedra enclosing the Fe ions rotate out-of-phase

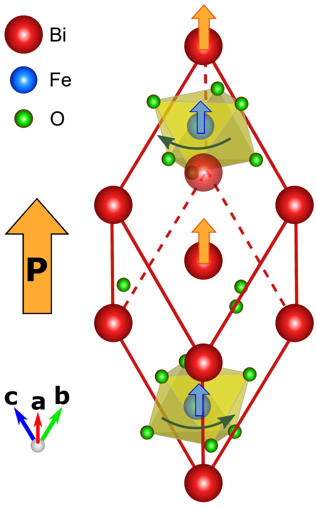

Figure 5.1: Rhombohedral unit cell of $BiFeO_3$, that includes two formula units. Oxygen octahedra rotate in opposite directions (out-of-phase). Polarization (P) induced along the elongated body diagonal is marked by large orange arrow outside the structure. Displacement of Bi and Fe atoms are illustrated by yellow and blue arrows, respectively at the atomic sites. Reproduced from Ref. [142].

also along the [111] direction, which is called antiferrodistortive (AFD) rotation. The final space group after these distortions is the rhombohedral $R3c$ [146] with electric polarization $\mathbf{P} \approx 80\mu\mathrm{C}/\mathrm{cm}^2$ along a $\langle 111 \rangle$-type axis, as shown in Fig. 5.1.

At such high crystallization temperatures, another secondary stoichiometric phase is easily stabilized, namely $Bi_2Fe_4O_9$ [144]. To avoid the formation of unwanted compounds, modern crystal growers utilize the incongruent melting method. For my experiments, I used large, high quality, ferroelectric monodomain samples grown by Ito et al. using the laser diode floating zone technique as described in Ref. [147].

5.1.1 Magnetic structures in $BiFeO_3$

The Fe^{3+} ions have $S = 5/2$ spins, i.e., a half-filled d shell, thus, the direct spin-orbit coupling is zero. Magnetic interactions originate from superexchange paths. The strongest exchange interaction originates from the nearly 180° nearest-neighbor Fe-O-Fe superexchange path. This antiferromagnetic interaction gives rise to a G-type antiferromagnetic structure [148], meaning that every spin is antiparallel to all its nearest neighbors in all spatial directions. As the inversion symmetry is broken in the ferroelectric phase, a weaker DM interaction becomes allowed in $BiFeO_3$. The microscopic spin Hamiltonian is[149]

$$
\begin{aligned}
\mathcal{H} =& J_1 \sum_{\langle i,j\rangle} \mathbf{S}_i \cdot \mathbf{S}_j + J_2 \sum_{\langle i,j\rangle'} \mathbf{S}_i \cdot \mathbf{S}_j \\
&+ D_1 \sum_{\langle i,j\rangle} \left(\mathbf{Z} \times \mathbf{e}_{ij}/a\right) \left(\mathbf{S}_i \times \mathbf{S}_j\right) + D_2 \sum_{\langle i,j\rangle} (-1)^{h_i} \mathbf{Z} \cdot \left(\mathbf{S}_i \times \mathbf{S}_j\right) \\
&- K_Z \sum_i S_{iZ}^2 - \frac{1}{2} K_H \sum_i \left[(S_{iX} + iS_{iY})^6 + (S_{iX} - iS_{iY})^6 \right] \\
&+ g\mu_{\mathrm{B}} \sum_i \mathbf{S}_i \cdot \mathbf{B} \qquad (5.1)
\end{aligned}
$$

where $a \approx 3.96\,\text{Å}$ is the pseudocubic lattice constant [146], Fe^{3+} ions are on the $\mathbf{R}_i$ sites, with $\mathbf{S}_i$ classical spin vectors, for which $S = 5/2$. Nearest neighbors $\langle i,j \rangle$ are connected: $\mathbf{R}_j = \mathbf{R}_i + \mathbf{e}_{ij}$. J_1 and J_2 are nearest and next-nearest neighbor interaction exchange coupling terms, both antiferromagnetic in nature. From elastic and inelastic neutron scattering measurements [150–152], the values for exchange interactions are $J_1 \approx 4.5\,\text{meV}$ and $J_2 \approx 0.2\,\text{meV}$. D_1 and D_2 are the homogeneous and the staggered components of the nearest-neighbor DM interaction. The nearest-neighbor exchange interaction J_1 is Heisenberg-like, and favors parallel alignment of neighboring spins. As opposed to that, the DM interaction is minimal for neighboring spins perpendicular to each other, and the competition with the exchange interaction leads to an incommensurate magnetic structure. D_1 determines the modulation wavelength [153]. The resulting AFM spin cycloid has a long wavelength of 62 nm, about 150 times larger than the lattice constant, setting $D_1 = 0.18$. Since the emergence of D_1 is the result of the polarization, the plane of the cycloid is defined by the polarization axis [111] and the ordering wave vector $\mathbf{q}$, that points to $\langle 1\bar{1}0 \rangle$-type directions. The cycloidal structure is illustrated schematically in Fig. 5.2 (b). As a result of the antiferrodistortive component of the structural distortion a staggered component of the DM interaction also appears. This $D_2 = 6 \times 10^{-2}\,\text{meV}$ staggered component makes the local AFM order cant [154, 155] by about 1°, which was measured by polarized neutron scattering [154]. Hexagonal layers of Fe^{3+} ions are labeled with $h_i = \sqrt{3}\mathbf{R}_i \cdot \mathbf{Z}/a$, and the tilt alternates in sign from one hexagonal plane to the next. The external magnetic field is $\mathbf{B}$, μ_{B} is the Bohr-magneton, and the g-factor is $g = 2$. The easy-axis coupling constant, i.e., the uniaxial magnetic anisotropy is denoted by K_Z, whose sign determines the easy-axis ($K > 0$) or easy-plane ($K < 0$) nature of the anisotropy. Its value can be determined from spectroscopy [156, 157], neutron diffraction [158], inelastic neutron scattering [151, 155] or NMR [159, 160] experiments, resulting in an easy-axis parallel [111], $K \approx 4 \times 10^{-3}\,\text{meV}$. The uniaxial anisotropy is also what renders the cycloids anharmonic, since it introduces a preferred direction for the rotating spins. The term including K_H describes the pinning of the cycloidal plane and the cycloidal wavevector **q** to one of the hexagonal $\langle 1\bar{1}0 \rangle$ axes.

The temperature - magnetic field phase diagram is displayed in Fig. 5.2 (e) for fields applied in the (111) plane. The cycloidal state is stable in the blue region. With circularly polarized X-ray diffraction measurements, the chirality of the cycloids was also established: the spins rotate clockwise viewing in the plane where polarization points down and the magnetic propagation vector to the right [108]. The canting of the cycloids does not result in a net macroscopic ferromagnetic moment, but a spin density wave (SDW) emerges. The SDW of the cycloids was first proven to exist via high-resolution time-of-flight diffraction experiments [161], and was further confirmed by polarized small-angle neutron scattering experiments [154].

A sufficiently high external magnetic field can suppress the cycloidal modulation, and via a metamagnetic phase transition, the spins flop to lie in the hexagonal plane in a canted antiferromagnetic (CAFM) fashion [162], shown in Fig. 5.2 (d). On the phase diagram of Fig. 5.2 (e), the temperature and magnetic field region corresponding to the CAFM phase is colored white.

At low temperatures, the magnetic phase diagram has been known for long. In the last decade, new magnetization and field-induced polarization measurements near room temperature revealed a new modulated phase between the cycloidal and the canted antiferromagnetic phases [143], shown as a gray region of the phase diagram in Fig. 5.2 (e). In line with the theoretical predictions [163], this phase was identified as the transverse conical phase. In this state, a homogeneous local antiferromagnetic order parameter develops perpendicular to the q vector besides the cycloidal modulation. Neutron diffraction experiments confirmed the cone structure [164]. Both magnetization [143] and neutron scattering data show a hysteresis of the phase between increasing and decreasing of the field, indicated as a blue-gray hatched region in Fig. 5.2 (e). The hysteresis indicates that the transition from cycloidal to cone structure is of first order, which also suggests that the transition comes with a structural distortion. This hysteresis also shows up in magnetostriction measurements [143]. In contrast, the phase transition from the conical state to the CAFM is continuous, with the cone angle closing as the magnetic field increases, without changing the period, as shown by neutron scattering experiments [164].

In thin films, the large epitaxial strain lowers the symmetry of the crystal to monoclinic. In this phase, the ferroelectric polarization is rotated from the [111] direction to the [001] direction [165, 166]. The modulated magnetic structure of the bulk crystal is suppressed under these circumstances, but the DM interaction still causes the spins to cant, resulting in a weak ferromagnetic moment [167].

In order to simplify the discussion, throughout this chapter, I will use the notation of $\{\mathbf{X},\mathbf{Y},\mathbf{Z}\}$ as $[1\bar{1}0] \parallel \mathbf{X}$, $[11\bar{2}] \parallel \mathbf{Y}$ and $[111] \parallel \mathbf{Z}$, as shown in Fig. 5.2, to indicate the principal directions.

Magnetoelectric coupling in BiFeO$_3$

In BiFeO$_3$, ferroelectric polarization develops at higher temperatures, independent of the magnetic order, thus it is classified as a type-I multiferroics. Nevertheless, changes in the magnetic order for example by application of a magnetic field alter the electric polarization. The origin of this magnetoelectric coupling is still not fully understood. Most importantly, the cycloidal plane, thus the propagation vector **q** is locked to the polarization. This allows the electric field control of the cycloids by changing the direction of the net polarization using an electric field [106, 168–170].

Polarization studies by Y. Tokunaga et al. [171] have revealed an additional polarization, perpendicular to the main polarization axis **Z**, and demonstrated the magnetic control of the electric polarization up to 300 K. More recent polarization and magnetization measurements reported an exceptionally high value of the ME coupling coefficient of 210 ps/m in the transverse conical phase [143]. As the coupling between the cycloidal plane and the ferroelectric polarization can be formulated in terms of the spin-current mechanism, the main contribution in the magnetically induced polarization is also often interpreted in terms of this mechanism. However, the magnetic Fe sites and Fe-Fe bonds have such low symmetry, that a local polarization can emerge from the magnetic order through exchange-striction, the spin-current, and single ion mechanisms as well [156, 157, 172, 173]. For example, the electrically induced shift of the spin resonances was explained by single-ion mechanisms [155, 174].

Spin waves in BiFeO$_3$

Spin waves (not to be confused with spin *density* waves [SDW]) are the collective excitations of the fluctuations in the magnetic structure, whose quasi-particles are the magnons. From the measurement of the magnon spectrum, the interactions governing the spin dynamics can be unraveled. The high-energy magnon spectrum of BiFeO$_3$ was measured by inelastic neutron scattering [150, 151]. As expected in an antiferromagnet, the magnon energies linearly decreasing toward the (π,π,π) point of the Brillouin zone corresponding to the G-type antiferromagnetic order. From the magnon dispersion, the exchange interaction parameters in Eq. (5.1) were deduced.

From low-energy spectroscopy, the parameters of the DM interaction and the single-ion anisotropy can be determined. A Raman study of BiFeO$_3$ revealed a series of low-energy excitations identified as magnon excitations [175]. Based on the theoretical work of R. de Sousa and J. E. Moore [176], these excitations are assigned to spin waves. Importantly, some of them were interpreted as electromagnons, which are electric dipole active spin waves. Temperature dependent Raman [177] and THz experiments [156, 178] combined with selection rule analysis [176] confirmed the electrical activity of magnons.

Following the continuum model developed in [176], I provide an intuitive picture of the spin-wave modes. For a two-sublattice antiferromagnet with sublattice magnetizations $\mathbf{M}_1$ and $\mathbf{M}_2$, the cycloidal ground state is described by

$$\mathbf{L}_0(x) = L_0[\cos(qx)\hat{\mathbf{z}} + \sin(qx)\hat{\mathbf{x}}], \tag{5.2}$$

where $\mathbf{L}_0 = \mathbf{M}_1 - \mathbf{M}_2$ is the antiferromagnetic Néel vector for a commensurate isotropic Heisenberg antiferromagnet. This antiferromagnetic moment rotates in a plane that contains $\hat{\mathbf{z}}$, and propagates along $\hat{\mathbf{x}}$. The spin-wave energies are calculated from a linearized equation of motion derived from a free energy functional. The free energy has terms equivalent to the Hamiltonian in Eq. (5.1) except the hexagonal anisotropy, which is not included in the continuum model. The fluctuations above the cycloidal ground state [Eq. (5.2)] are expanded in terms of two fields: $\Phi(\boldsymbol{r})$ and $\Psi(\boldsymbol{r})$, which refer to phase fluctuations of the cycloidal ground state and spin fluctuations out of the cycloid (xz) plane, respectively. These are the two kinds of motion of the spin excitations. For the case $k \to 0$, the Φ mode introduced an additional phase to the harmonic functions in Eq. (5.2), which corresponds to the rotation of $\mathbf{L}_0$. Since this is a symmetry of the model, it costs zero energy, and the Φ_0 mode is a Goldstone mode. In contrast, the Ψ_0 mode is gapped due to the pinning of the cycloid plane by the ferroelectric moment. At higher energies, modes at n multiples of the wavenumber q appear at the zone center ($k = 0$, i.e., the Γ point) because of the zone folding, which results in a series of excitations. These optical resonance can be probed by Raman or THz spectroscopy.

The ME effect gives rise to multiple phenomena at finite frequencies, among others, NDD. With a sum-rule, the magnetoelectric susceptibility and the optical excitations of electromagnons can be connected [72]. Previously, the NDD in the low temperature cycloidal phase was observed by Kézsmárki et al. [29] and Farkas et al. [179]. These works suggest that technologically interesting non-reciprocal absorption is present even at room temperature, though, its systematic study has not been carried out. In the simplest approach, the spin-current mechanism (also known as the inverse Dzyaloshinskii-Moriya coupling) induces polarization perpendicular to the plane of the cycloid at the Ψ_1 mode corresponding to the homogeneous rotation of the cycloidal plane around the q vector. However, the experiments show NDD, thus, electric dipole moment for other Ψ as well as for Φ modes. Therefore, this term alone cannot capture the dynamic magnetoelectric effect. The modulation of the magnetocrystalline anisotropy or anisotropies in the spin-current mechanism should be taken into account [179].

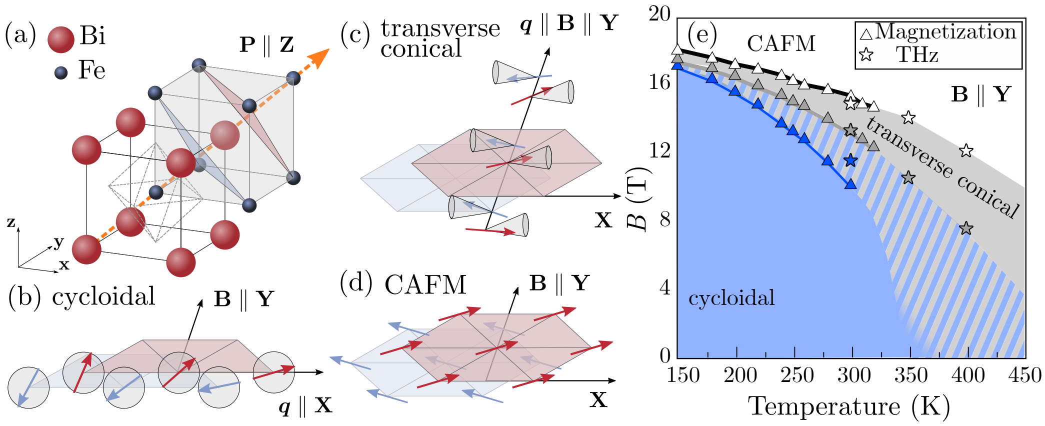

Figure 5.2: (a) Cubic structure of $BiFeO_3$ with the emergent ferroelectric polarization **P** along the body diagonal. Fe^{3+} ions form a simple cubic lattice. The antiferromagnetic sublattices are noted with pale red and blue triangles. (b)–(d) Schematic drawings of spin orderings in the (b) cycloidal, (c) transverse conical and (d) canted antiferromagnetic (CAFM) phases in $BiFeO_3$. (e) Temperature and magnetic field dependent magnetic phase diagram of $BiFeO_3$. Upon increasing the magnetic field, a first-order phase transition between the cycloidal and the transverse conical state takes place at the gray symbols, and the second-order transition from transverse conical to the CAFM phase at the white symbols. In decreasing fields, the change from CAFM to conical state happens at the same fields as in increasing fields, while the transition from conical to cycloidal phase occurs at lower field values, noted by blue symbols. Thus, the transverse conical state has a hysteresis, which broadens as the temperature increases. The magnetization data in the temperature range from 150 to 300 K are adapted from Ref. [143].

5.2 SANS experiments

As described previously in Chapter 3, scattering experiments are the principal tool to get information about spatially periodic structures. SANS probes modulated magnetic structures that have a characteristic length above 10 Å, thus, it is ideal to study the modulated magnetic states of $BiFeO_3$. Since the SDW in $BiFeO_3$ is induced by the antiferromagnetic structure, the magnetic scattering peaks at small-angles provides high resolution information on the modulated magnetic structures. With my colleague D. G. Farkas we probed the cycloidal and the transverse conical structure of $BiFeO_3$ at high temperatures at the Paul Scherrer Institut with the help of J. S. White, who was the local instrument scientist.

For the experiments, we used the SANS-I instrument. The probing wavelength was 8 Å, the collimator and detector lengths were 15 m, the incoming neutron beam was set to be nearly parallel to the **Z** axis. The sample was in a cryostat equipped with a superconducting magnet. The part where the neutron beam enters the cryostat is made of aluminum, which is transparent for neutrons. The cryostat itself is installed on top of a goniometer, to allow the rocking of the sample together with the magnetic field around the horizontal (called PHI, to which the angle of rotation φ belongs) and the vertical (called SAN, to which the angle of rotation ψ belongs) axes. The $BiFeO_3$ sample was installed so that horizontal axis is parallel the crystallographic direction **X** and the vertical axis is parallel the crystallographic direction **Y**, illustrated in Fig. 5.8 (a). Below is my analysis of the results of the high-temperature SANS experiments.

5.2.1 Analysis of diffraction patterns

The cycloidal structure of a bulk crystal at low temperatures has been analyzed by my research group before. In these ferroelectric monodomain samples, the three cycloidal domains produce six spots in the scattering image, corresponding to the $\pm\mathbf{q}$ domains, as can be seen in Fig. 5.3 (a). They found that with the application of magnetic field, one cycloidal domain can be stabilized, with q vector perpendicular to the in-plane field direction, as shown in Fig. 5.3. The spots corresponding to the selected domains remain at around the high field positions even after decreasing the field to zero, thus, this magnetic field treatment can align the cycloidal domains.

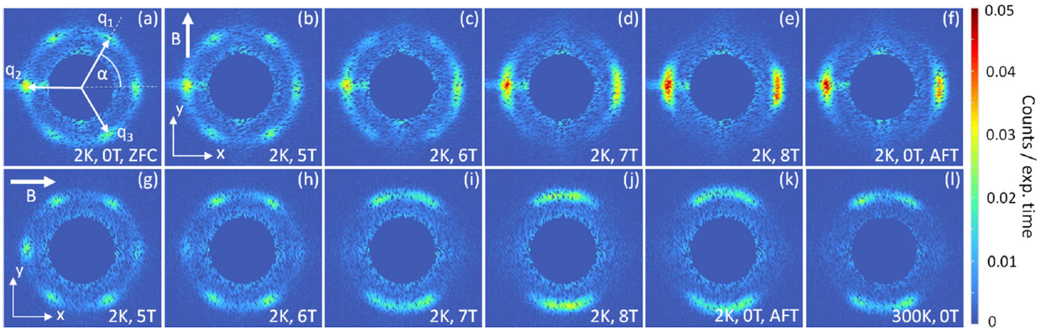

Figure 5.3: (a)–(f) SANS images of $BiFeO_3$ recorded at 2 K. (a) In the zero-field cooled (ZFC) state. (b)–(e) In increasing fields for $\mathbf{B} \parallel \mathbf{Y}$, and (f) in zero-field after field treatment (AFT). (g)–(j) SANS images recorded at 2 K after zero-field cooling the sample, and increasing the external fields in the direction $\mathbf{B} \parallel \mathbf{X}$. (k) SANS image of the zero-field state of the sample after field treatment at 2 K, and (l) at 300 K. Reproduced from Ref. [180].

I investigated the field dependence of the scattering pattern at and above room temperature. Scattering images were recorded at 400, 500 and 600 K on a **Z**-cut sample with an incoming beam parallel with the Z axis (apart from small tilt for rocking). The diffraction patterns in Figs. 5.4, 5.5 and 5.6 are the result of

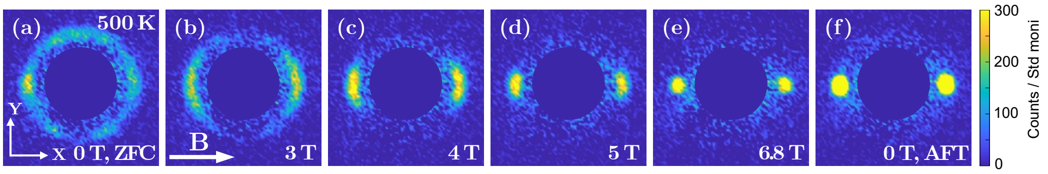

Figure 5.4: SANS images of $BiFeO_3$ at 500 K. The order of the images represents the sequence of the measurement: starting from (a) the zero-field cooled (ZFC) state, (b)–(e) the $\mathbf{B} \parallel \mathbf{X}$ field is applied, and (f) ramped down to zero again, resulting in a diffraction image after field treatment (AFT).

subtracting a reference scattering image collected in zero-field at 635 K. For easier understanding of the data, I start with the discussion of the dataset recorded at 500 K. The magnetic field dependence of the Bragg peaks at 500 K is shown in Fig. 5.4. On panel (a), the six Bragg spots corresponding to the cycloidal phase can be observed after zero-field cooling, though the orientation of the q vectors is smeared, indicated by the finite intensity ring. On panels (b)–(e), a magnetic field along the X direction is applied. As the field strength is increased, unlike in the low temperature results, the scattering intensity gathers in the horizontal spots, parallel with the external field. This behavior suggests a different modulated magnetic structure, for which the parallel alignment with the field is energetically more favorable, i.e., the magnetic suscpetibility is larger when the field is along the q vector. This is an indication of the transverse conical state. Unlike the cycloidal state with largest susceptibility perpendicular to the cycloidal planes, i.e., to the q vectors, the conical state has larger susceptibility along the q vector. After driving the field back to zero, the intensity stays at the horizontal spots [panel (f)]. At 600 K, in Fig. 5.5, we can observe a similar field dependence, with the difference that no Bragg peaks are resolvable at and above 4 T [panel (e)]. The absence of the Bragg peaks at small angle suggests that the CAFM phase is reached. When the field is decreased, the scattering intensity is concentrated in the two horizontal spots, even in zero magnetic fields as shown in Fig. 5.5 (f). The asymmetry in the intensity of the horizontal spots may be attributed to the slight misalignment (few degrees) of the sample.

At 400 K, the pattern is more complex. The scattering image series in Fig. 5.6 show two kinds of q vector reorientation processes. Up to 3 T, the diffraction pattern does not change from the 3 cycloidal domain image. Then from 4 T, the scattering peak intensities and positional distributions start to change. On one hand, the scattering intensity starts to gather at the vertical positions, perpendicular to the applied field direction, typical for cycloids. On the other hand, the horizontal peaks do not disappear, and as a result, at the highest field, at 6.8 T [panel (e)], the scattering intensity is distributed in four positions, indicating a phase coexistence.

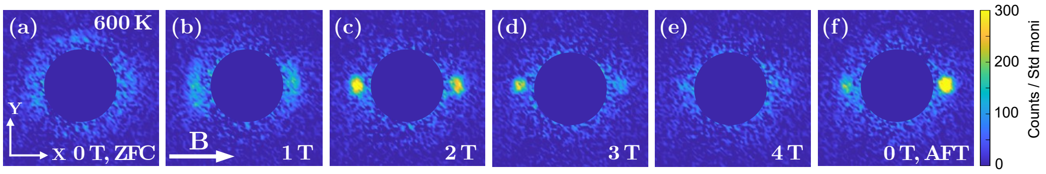

Figure 5.5: SANS images of $BiFeO_3$ at 600 K. The order of the images represents the sequence of the measurement: starting from (a) the zero-field cooled (ZFC) state, (b)–(e) the $\mathbf{B} \parallel \mathbf{X}$ field is applied, and (f) ramped down to zero again, resulting in a diffraction image after field treatment (AFT).

The temperature is low enough to overcome the pinning field and start to orient the cycloidal q vector, but at the same time, high enough for the transverse conical phase to appear. These two phenomena can be observed simultaneously in Fig. 5.6.

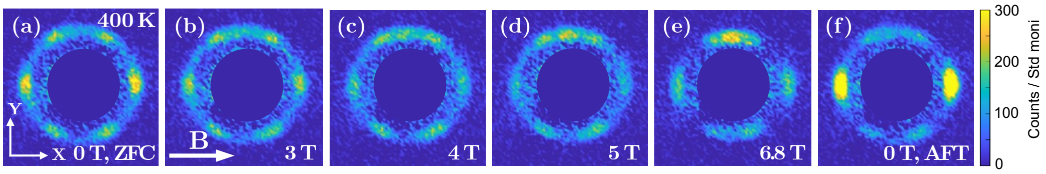

Figure 5.6: SANS images of $BiFeO_3$ recorded at 400 K. The order of the images represents the sequence of the measurement: starting from (a) the zero-field cooled (ZFC) state, (b)–(e) the $\mathbf{B} \parallel \mathbf{X}$ field is applied, and (f) ramped down to zero again, resulting in a diffraction image after field treatment (AFT).

5.2.2 Quantitative analysis of the diffraction pattern

In this section, I present the quantitative analysis of the diffraction patterns to gain further insights to the variation of the magnetic order over the temperature-magnetic field phase diagram.

First, I checked how the length of the modulation vector, q changes as a function of the temperature in the zero-field-cooled state. I angularly integrated the intensity on the image plates and plotted its $|q|$ dependence in Fig. 5.7 (a). As shown in the figure, the total intensity of the diffraction peaks decreases as the temperature increases, a result of the thermal fluctuations that disrupt the cycloidal modulation. The length of the q vector is obtained as the peak position of a Gaussian fit to the intensity distribution data. The q vector length is plotted as a function of temperature (2018. October, PSI) with earlier data obtained by my group (2016. September, ILL) in Fig. 5.7 (b). From 2 K to 600 K, the modulation vector shortens, thus, the period increases, by $\sim 14\%$. The high temperature reduction of $|q|$ implies that the DM interaction strength is reduced relative to the Heisenberg exchange, which may be the consequence of the weaker polar distortion.

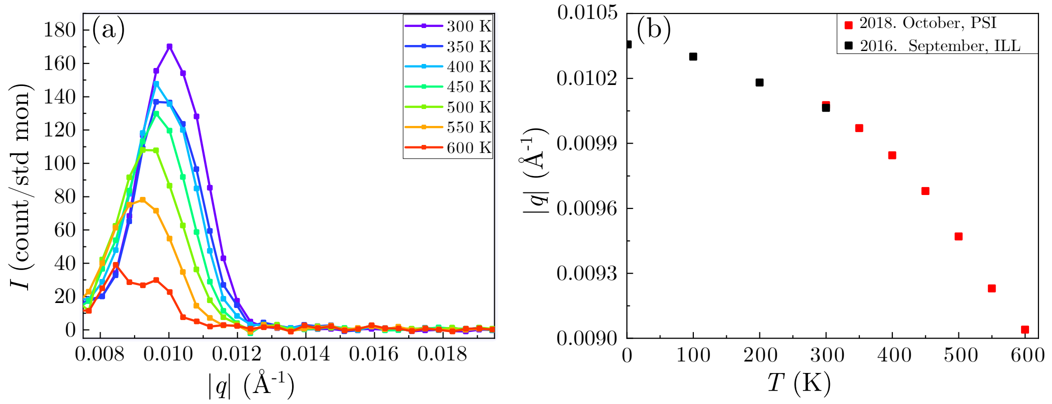

Figure 5.7: (a) Radial distribution of diffraction intensity, from 300 K to 600 K. (b) Temperature dependence of the q vector length.

The analysis of the rocking curves also provides information about the out-of-plane correlations. A simple pair of rocking curves at $T = 300$ K in zero-field is shown in Fig. 5.8 (b), where intensity is integrated in the black and red boxes in Fig. 5.8 (a). The rocking curves are useful in determining the out-of-plane correlation length, as their full width at half maximum (FWHM) is inversely proportional to that quantity. The connection with the rocking angle ψ (assuming that it is small) is given by $\xi = 2/(\psi|\mathbf{q}|)$. From the Lorentzian fit to the two peaks shown in Fig. 5.8 (b), the two correlation lengths are $1 \pm 0.1\ \mu$m and $1.3 \pm 0.2\ \mu$m for the horizontal left (at $-q_x$) and right (at $+q_x$) peaks, respectively. I calculated the correlation length for 300, 350, 400, 450, 500 and 550 K by taking the average FWHM of the two rocking peaks in the $\mathbf{X}$ direction, since they belong to the same q vector. The temperature dependence of the correlation length shown in Fig. 5.9 (a) has a bump around 500 K. No traces of this anomaly can be found in the temperature-dependent susceptibility curve in Fig. 5.9 (b).

Taking a closer look at the rocking curves of the transverse conical patterns serves with an unanticipated phenomenon. The observed horizontal peaks with q vector parallel $\mathbf{X}$ in Figs. 5.4, 5.5 and 5.6 are actually two peaks averaged together. The ψ dependence of the intensity in Fig. 5.10 shows a clear splitting of the rocking peaks both for the $+X$ (red) and $-X$ (black) directions. The peak positions in the $\mathbf{XZ}$ plane, and their evolution in magnetic fields are presented in Fig. 5.11. The peaks split in magnetic fields, and the splitting is enhanced by the field. This behavior suggests that the q vector has a very small out-of-plane canting, which is increased by the external field. I found no reports on this field-induced rotation of the cycloidal q vector in the literature so far, neither a theory predicting (or

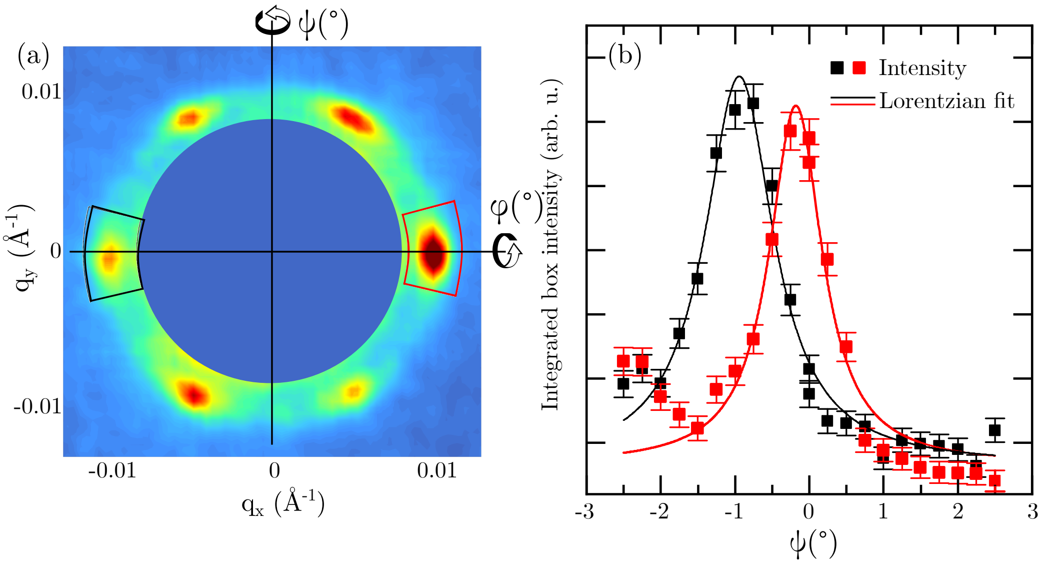

Figure 5.8: (a) SANS pattern of a **Z**-plane $BiFeO_3$ sample at $T = 300$ K in zero-field. The axes of rocking are marked with φ and ψ. (b) Rocking curves of the two horizontal scattering peaks marked on panel (a). The squares are the intensity integrated in the respective sections at each rocking angle, the solid lines are Lorentzian fits to these datapoints. Red symbols correspond to data obtained from the red box, black symbols correspond to data from the black box on panel (a).

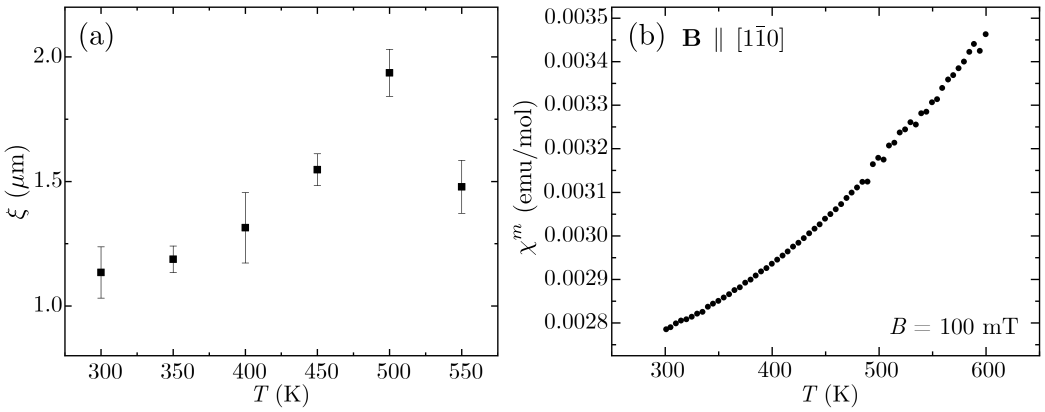

Figure 5.9: (a) Temperature dependence of the out-of-plane correlation length in $BiFeO_3$ in zero-field. (b) Temperature dependence of the magnetic susceptibility in $BiFeO_3$. Susceptibility was measured in decreasing temperatures from 600 K, after the application of 5 T magnetic field, then reducing it to 100 mT. (Measured by D. Vieweg at the University of Augsburg.)

explaining) this behavior.

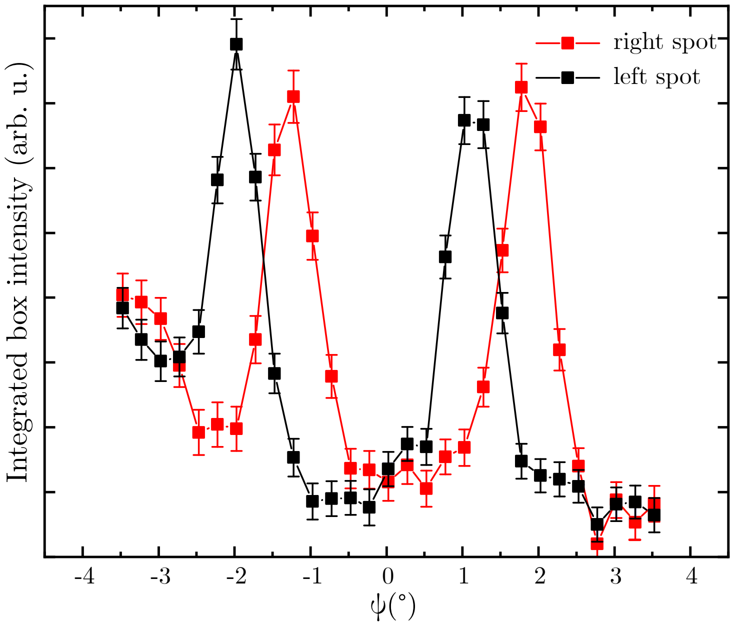

Figure 5.10: The rocking curves of the two horizontal zero-field scattering spots in $BiFeO_3$ at $T = 500$ K in 6.8 T magnetic field parallel **X** [See Fig. 5.4 (e)].

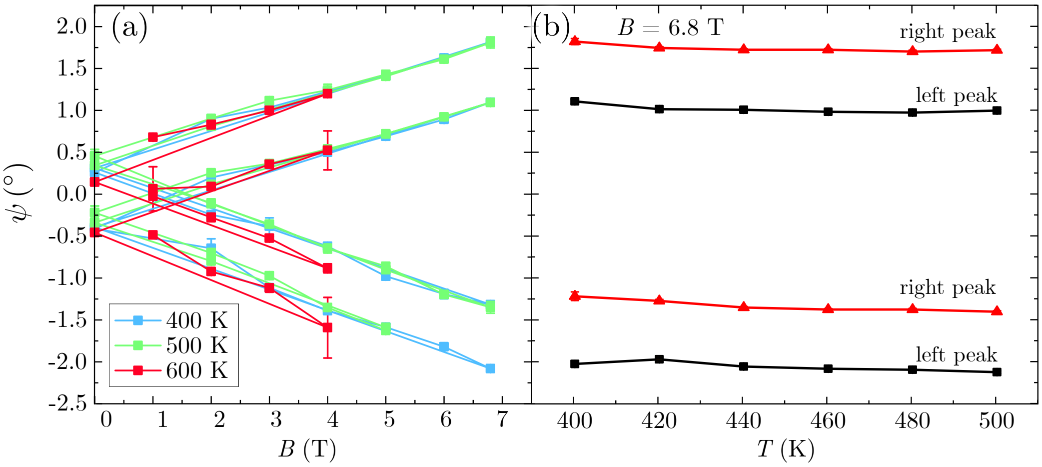

Figure 5.11: (a) Angular splitting of the scattering peaks in the transverse conical phase as a function of external magnetic field. (b) Temperature dependence of the angular splitting of the zero-field left and right scattering peaks [see Figs. 5.8 (a) and 5.4] at 6.8 T. The splitting angle does not depend on the temperature.

5.3 High temperature THz studies

The spin excitations of the cycloidal phase at low temperatures in $BiFeO_3$ have been exhaustively investigated by my colleague, D. G. Farkas [179]. The goal of my research was the observation of the collective spin-wave modes at high temperatures where the newly discovered transverse conical phase is stable. We studied the spin-wave excitations by THz spectroscopy in high magnetic fields at and above room temperature in cooperation with Estonian colleagues at the KBFI in Tallinn. The experimental technique and the setup is detailed in Section 3.1.2.

5.3.1 Spin-wave excitations

We measured the field dependence of the THz absorption spectrum at 300, 350 and 400 K for field directions $\mathbf{B} \parallel \mathbf{X}$ and $\mathbf{B} \parallel \mathbf{Y}$, up to 17 T. At these temperatures, the magnetic fields' range covers all the three known magnetic phases of $BiFeO_3$.

In order to follow the temperature dependence of the spin-wave resonances of the cycloidal phase, first, we measured spectra between 5 and 350 K upon warming up the sample. We oriented the cycloidal domains at the lowest temperature by applying 17 T along the **Y** axis and then decreased the field to zero again before the temperature dependent experiments. The temperature evolution of the zero-field absorption peaks is shown in Fig. 5.12. The excitations shift to lower frequencies as the sample temperature increases, in agreement with former Raman and THz spectroscopy studies [156, 175, 181]. The identification of the modes will prove useful later on, when cross-checking the selection rules of the cycloidal phase at high temperatures.

Magnetic field dependence of the spin resonances of$BiFeO_3$ at 300 K are plotted for fields parallel **X** and **Y** in Fig. 5.13 and Fig. 5.14, respectively. Because of the hysteretic nature of the transverse conical phase, all high-temperature measurements consist of an increasing and decreasing strength magnetic field sweep. Spectra measured in increasing fields are plotted in red, while spectra measured in decreasing fields are plotted in blue. The state of the sample was always initialized, i.e., sufficiently high magnetic fields were applied to the sample to select one cycloidal domain. As the SANS experiments showed, the domain selection works not only at low temperatures [180], but near room temperature as well. In Figs. 5.13 and 5.14, three regions can be distinguished based on the spin resonances, separated from each other by critical field values B_{c1} and B_{c2}. The first region, corresponding to the cycloidal phase starts from zero-field and in increasing fields (red spectra), persists up to $B_{c1} \sim 13-13.5\,\mathrm{T}$ for $\mathbf{B} \parallel \mathbf{Y}$, and up $B_{c1} \sim 12-13\,\mathrm{T}$ for $\mathbf{B} \parallel \mathbf{X}$. The difference in the critical field values may come from the in-plane anisotropy [149, 179, 180]. At these field values, the course of the resonances changes suddenly, some modes simply disappear. Above B_{c1}, the resonances of the

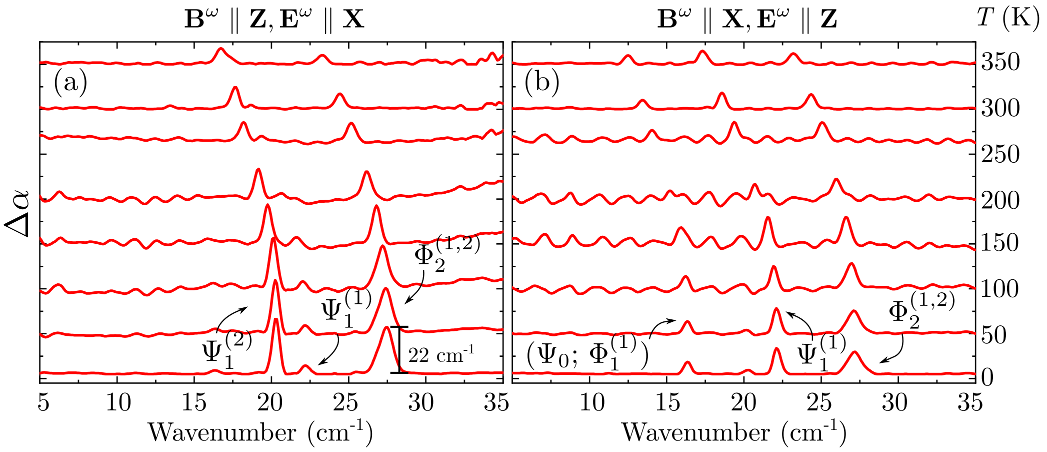

Figure 5.12: Zero-field absorption spectra measured at increasing temperatures for (a) polarization $\mathbf{B}^\omega \parallel \mathbf{Z}, \mathbf{E}^\omega \parallel \mathbf{X}$, and (b) polarization $\mathbf{B}^\omega \parallel \mathbf{X}, \mathbf{E}^\omega \parallel \mathbf{Z}$. The absorption curves are vertically shifted by a constant proportional to the sample temperature. The excitations are identified and labeled following Ref. [172].

transverse conical phase are observable until the next sudden change at $B_{c2} = 15\,\mathrm{T}$, above which the two strongest modes transform into the resonances of the CAFM phase. In decreasing fields, the transition from CAFM to transverse conical phase takes place at the same B_{c2} field in agreement with its second order nature. The field region of the transverse conical phase is broader, i.e., for decreasing fields, B_{c1} occurs at a lower field value, $\sim 12\,\mathrm{T}$, indicating the hysteresis of the conical phase.

Spectra recorded at 350 K and at 400 K are shown in Fig 5.15. At 350 K, the external field was $\mathbf{B} \parallel \mathbf{Y}$, while at 400 K, $\mathbf{B} \parallel \mathbf{X}$. The critical field goes lower as the temperature increases, in agreement with Ref. [143]. In increasing fields, at 350 K, Fig. 5.15 (a), (b), the cycloidal to conical transition is at 10 T, while the phase transition from conical to CAFM phase is at 14 T. At 400 K, Fig. 5.15 (c), (d), these transition fields are at ~8 T and ~12 T, respectively. In decreasing fields, the CAFM-to-conical transition occurs at the same value, just like at 300 K, but there is no discontinuous change that indicates a transition back from conical to cycloidal phase. This shows that the conical state persists to lower fields, but at zero-field, the spin excitations, although with different intensities, have the same frequency before and after the application of high fields. We can assume that at these temperatures, the conical phase remained metastable after high-field treatment. Another option would be that the conical structure is continuously deformed back to cycloidal. The first scenario, a zero-field conical state would be advantageous, because of the reported high ME coefficient of 210 ps/m [143]. Stabilizing a high-field magnetic phase at zero-field is not without precedence. In

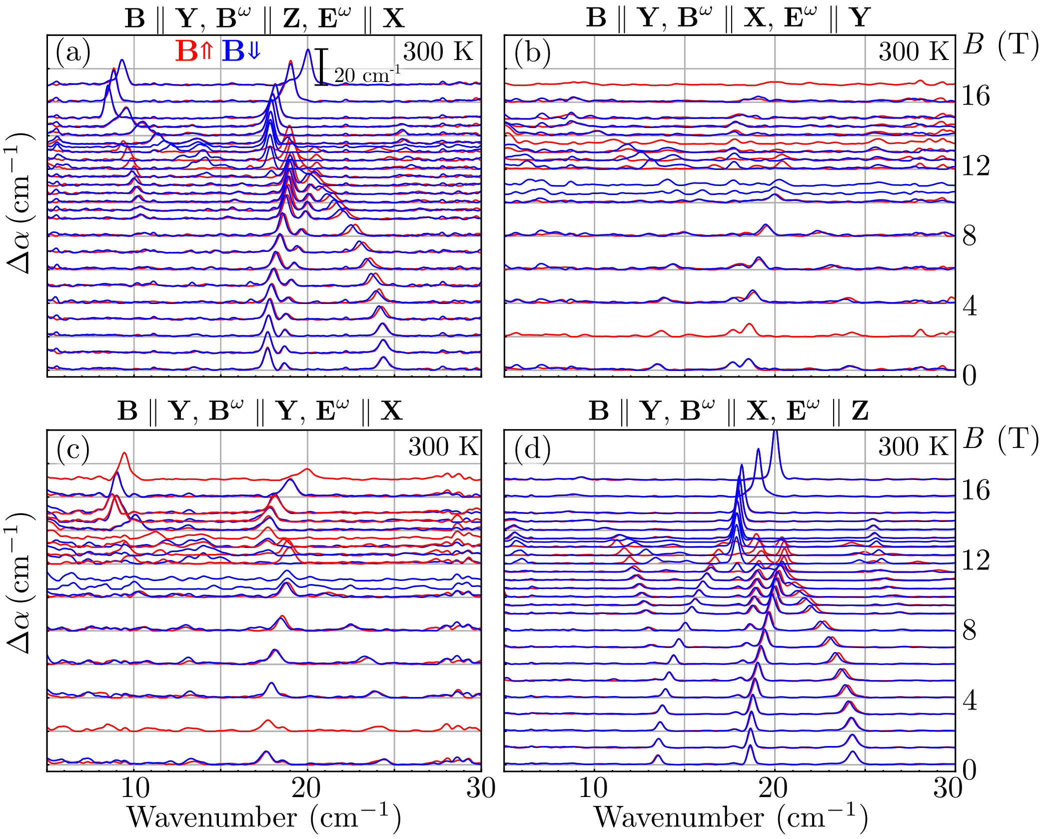

Figure 5.13: Absorption spectra measured at 300 K, for external field direction along **Y**, with different active modes present in different polarizations. Spectra measured in increasing (decreasing) fields are plotted in red (blue). The absorption curves are vertically shifted by a constant proportional to the magnetic field **B**.

$Fe_2Mo_3O_6$, the high-field ferrimagnetic state becomes metastable in zero field and replaces the antiferromagnetic structure after a magnetic field is cycled through the ferrimagnetic phase. [182, 183].

In the following, I analyze the spin wave resonances based on the data collected at 300 K in increasing magnetic fields. It is the temperature with the most recorded field and polarization configurations, as well as the dataset with clear phases and phase boundaries. I took the resonance positions and intensities, as well as the polarization configurations, and plotted the modes in a common graph for different external field directions in Fig. 5.16. Gray horizontal dashed lines indicate the critical fields B_{c1} and B_{c2}. The data points in Fig. 5.16 come from different measurements, with different field steps. This is the reason why some symbols are only at every fourth Tesla, some are at every .5 T.

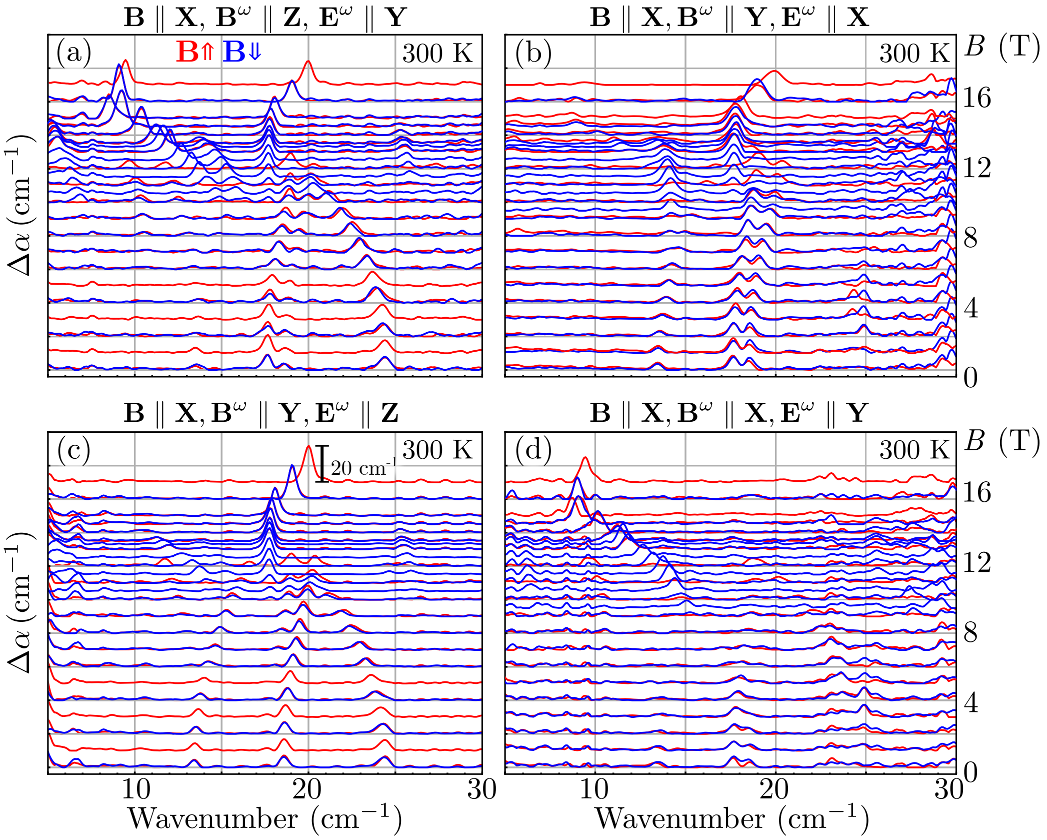

Figure 5.14: Absorption spectra measured at 300 K, for external field direction along **X**, with different active modes present in different polarizations. Spectra measured in increasing (decreasing) fields are plotted in red (blue). The absorption curves are vertically shifted by a constant proportional to the magnetic field **B**.

5.3.2 Cycloidal phase

In the cycloidal phase, we observed seven modes. With the help of the temperature dependent data, the identification of modes was fairly straightforward, using Refs. [172, 179]. At low energies, the first two observable modes, $\Phi_1^{(2)}$ and $\Phi_1^{(1)}$ appear only in finite fields, around ∼9 T. They are followed by modes Ψ_0, $\Psi_1^{(2)}$, $\Psi_1^{(1)}$, and $\Phi_2^{(1,2)}$, appearing in zero-field at 13.4, 17.6, 18.5, and 24.3 cm^{-1}, respectively. The highest-energy observable mode is $\Psi_2^{(1,2)}$, that gains strength in finite fields, but remains very weak nonetheless. The selection rules are mostly in agreement with those reported at low temperatures in [179], except for the $\Phi_1^{(1)}$ mode, that is present in Ref. [179] for $\mathbf{B} \parallel \mathbf{X}$ when $\mathbf{B}^{\omega} \parallel \mathbf{Y}$ and $\mathbf{E}^{\omega} \parallel \mathbf{X}$. This resonance however, is weak, gaining strength with field, and might stay under

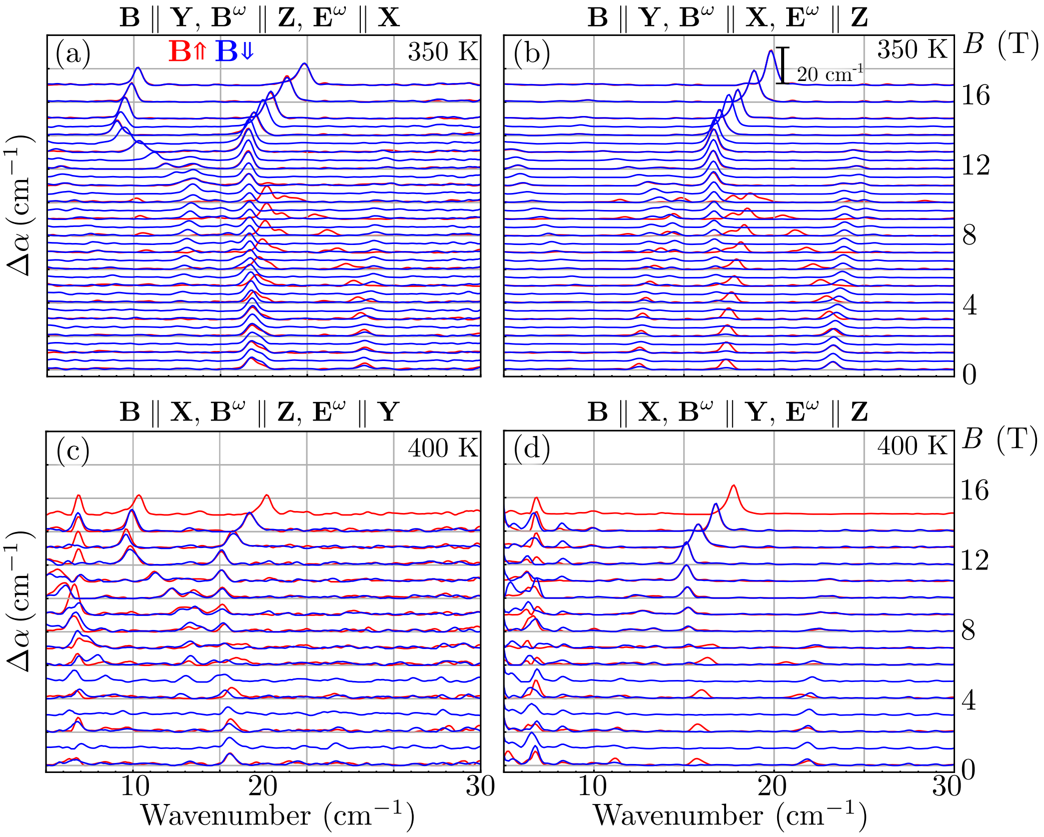

Figure 5.15: (a), (b) Absorption spectra measured at 350 K, for external field direction along **Y**, and (c), (d) at 400 K for **B** ∥ **X**. Spectra measured in increasing (decreasing) fields are plotted in red (blue). The absorption curves are vertically shifted by a constant proportional to the magnetic field **B**.

the detection limit in my high-temperature measurements, due to the reduced signal-to-noise ratio.

5.3.3 Transverse conical phase

We observed five modes in the transverse conical phase present between $B_{\mathrm{c}1}$ and $B_{\mathrm{c}2}$. Mode #1 appears at 5.5 cm^{-1} , and is weak and almost field independent. Mode #2 appears at 12 cm^{-1} , and shifts to lower energies as the field is increased, finally evolving into the lower-energy mode of the CAFM phase. Mode #3 is again very weak, losing intensity with the field. It is followed by mode #4, a strong, nearly field independent mode, that continues as the higher-frequency mode of the CAFM phase. The last observable mode at high energies is mode #5, which is again weak, that loses intensity with the magnetic field.

The two strongest modes, mode #2 and mode #4, that evolve into the two modes in the CAFM phase, are present in all polarization configurations. The intensity of mode #2 increases with the field, except for when $\mathbf{B} \parallel \mathbf{X}$ and $\mathbf{B}^{\omega} \parallel \mathbf{Y}$, and when $\mathbf{B} \parallel \mathbf{Y}$ and $\mathbf{B}^{\omega} \parallel \mathbf{X}$, the black and green symbols in Fig. 5.16 (a), red and green symbols in Fig. 5.16 (b), respectively. In these circumstances, the intensity decreases with the field, indicating that the in-plane $\mathbf{B}^{\omega}$ perpendicular to $\mathbf{B}$ does not couple strongly to mode #2. Mode #4 is weak when the polarizations is $\mathbf{B}^{\omega} \parallel \mathbf{X}, \mathbf{E}^{\omega} \parallel \mathbf{Y}$ for both external field directions.

The other three modes remain weak and even lose intensity with the external field as the cone angle is closed. Mode #1 is active in all polarization configurations when $\mathbf{B} \parallel \mathbf{Y}$. For $\mathbf{B} \parallel \mathbf{X}$, this mode is observable only in two polarization configuration, but we cannot draw conclusions from that, since this mode is very close to the low-frequency cutoff of the experimental setup. Mode #3 stays silent in only one configuration for both $\mathbf{B} \parallel \mathbf{X}$ and $\mathbf{B} \parallel \mathbf{Y}$. For the former case, the polarization is $\mathbf{B}^{\omega} \parallel \mathbf{Y}, \mathbf{E}^{\omega} \parallel \mathbf{Z}$, for the latter it is $\mathbf{B}^{\omega} \parallel \mathbf{X}, \mathbf{E}^{\omega} \parallel \mathbf{Z}$, both cases are represented with green triangle symbols in Fig. 5.16. Mode #5 is similar to mode #1 in the sense that it is close to the high-frequency cutoff of the setup and may lie undetected in some of the measurements presented here.

5.3.4 CAFM phase

In the CAFM phase, two resonances are expected [184]. The theoretical calculations of P. Pincus [184] considered a two-sublattice antiferromagnet, where the sublattices were canted due to the DM interaction that introduced anisotropy in the system. The effect of canting is a weak ferromagnetic moment. The model also considered a uniaxial anisotropy, and additionally to such already existing calculations, a small anisotropy in the basal plane. This model was used to describe hematite (αFe$_2$O$_3$), but is a good description of BiFeO$_3$ as well. One of the resultant modes, the lower-frequency one, is an oscillation of the weak ferromagnetic moment in the basal plane. The other, higher-frequency mode is the simple antiferromagnetic resonance discussed earlier in Chapter 3.

The lower-frequency mode in BiFeO$_3$ is strong for both external field directions in two polarizations: in the case of $\mathbf{B} \parallel \mathbf{X}$, these polarizations are $\mathbf{B}^{\omega} \parallel \mathbf{X}, \mathbf{E}^{\omega} \parallel \mathbf{Y}$, and $\mathbf{B}^{\omega} \parallel \mathbf{Z}, \mathbf{E}^{\omega} \parallel \mathbf{Y}$. When $\mathbf{B} \parallel \mathbf{Y}$, the favored polarizations are $\mathbf{B}^{\omega} \parallel \mathbf{Y}, \mathbf{E}^{\omega} \parallel \mathbf{X}$, and $\mathbf{B}^{\omega} \parallel \mathbf{Z}, \mathbf{E}^{\omega} \parallel \mathbf{X}$. In theory, the lower energy mode can be excited by magnetic fields oscillating perpendicular to the static field. This is in agreement with the experiments, when $\mathbf{B}^{\omega} \parallel \mathbf{Z}$, however, the other polarization, $\mathbf{B}^{\omega} \parallel \mathbf{B}$ should not couple to the magnetization oscillation of this mode. This inconsistency can be resolved if this mode has an in-plane electric dipole moment perpendicular to the magnetic field. This lower-frequency mode also appears when $\mathbf{B} \parallel \mathbf{X}$ and $\mathbf{B}^{\omega} \parallel \mathbf{Y}, \mathbf{E}^{\omega} \parallel \mathbf{X}$, but much weaker than the cases mentioned above. Thus, this mode couples weakly to in-plane oscillating magnetic field $\mathbf{B}^\omega$, that is at the same time perpendicular to the external field $\mathbf{B}$. The higher-frequency mode is present in all measured polarization configurations, however, its intensity is weak both when $\mathbf{B}^\omega \parallel \mathbf{X}, \mathbf{E}^\omega \parallel \mathbf{Y}$, for both $\mathbf{B} \parallel \mathbf{X}$ and $\mathbf{B} \parallel \mathbf{Y}$. From Fig. 5.16 it is visible, that the frequencies of the modes in the CAFM phase are not different for the directions of the external magnetic field in the hexagonal plane (**X** and **Y** directions). This is in contrast with what has been reported at low temperatures, where the higher-frequency mode shifted to higher energies when the magnetic field changed from $\mathbf{B} \parallel \mathbf{X}$ to $\mathbf{B} \parallel \mathbf{Y}$ [185] due to different strain in the different field directions. Therefore, the in-plane anisotropy has negligible effect on the resonances at room temperature, suggesting that it is vanishing at elevated temperatures.

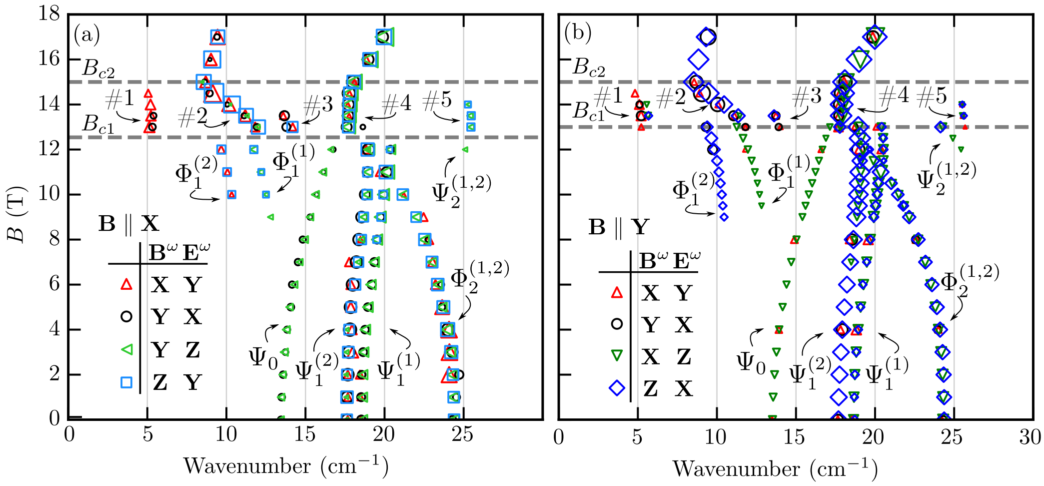

Figure 5.16: Resonance positions at $T = 300\,\mathrm{K}$, for different increasing field directions for different light polarizations, and identification of modes. (a) For external field $\mathbf{B} \parallel \mathbf{X}$, and (b), for external field $\mathbf{B} \parallel \mathbf{Y}$. The magnetic structure is cycloidal from 0 T to B_{c1}, transverse conical between B_{c1} and B_{c2}, and canted antiferromagnetic above B_{c2}. Marker sizes are proportional to the absorption line areas.

5.3.5 Directional dichroism

As discussed earlier in Chapter 1, at finite frequencies the ME effect shows up as NDD, the nonreciprocal absorption of light. In $BiFeO_3$, the reversal of light propagation direction is symmetry equivalent to reversing the external magnetic field direction [29]. Therefore, we recorded spectra in positive and negative magnetic fields to deduce NDD as the difference of the absorption [29]. The results are summarized in Fig. 5.17, where absorption spectra at 300 K are plotted for increasing field magnitudes, positive fields plotted in red and negative fields black. The dichroism was then identified as the difference between the absorptions in positive and negative fields. NDD was measured in Voigt configuration, **k** $\parallel$ **Z**, for two field directions, **B** $\parallel$ **X** and **B** $\parallel$ **Y**. We can observe dichroism in all three phases, but it is most prominent in the conical phase for the configuration **B** $\parallel$ **X**, $\mathbf{B}^{\omega} \parallel \mathbf{Y}$, $\mathbf{E}^{\omega} \parallel \mathbf{X}$ near the upper phase boundary $B_{c2} \approx 15\,\mathrm{T}$.

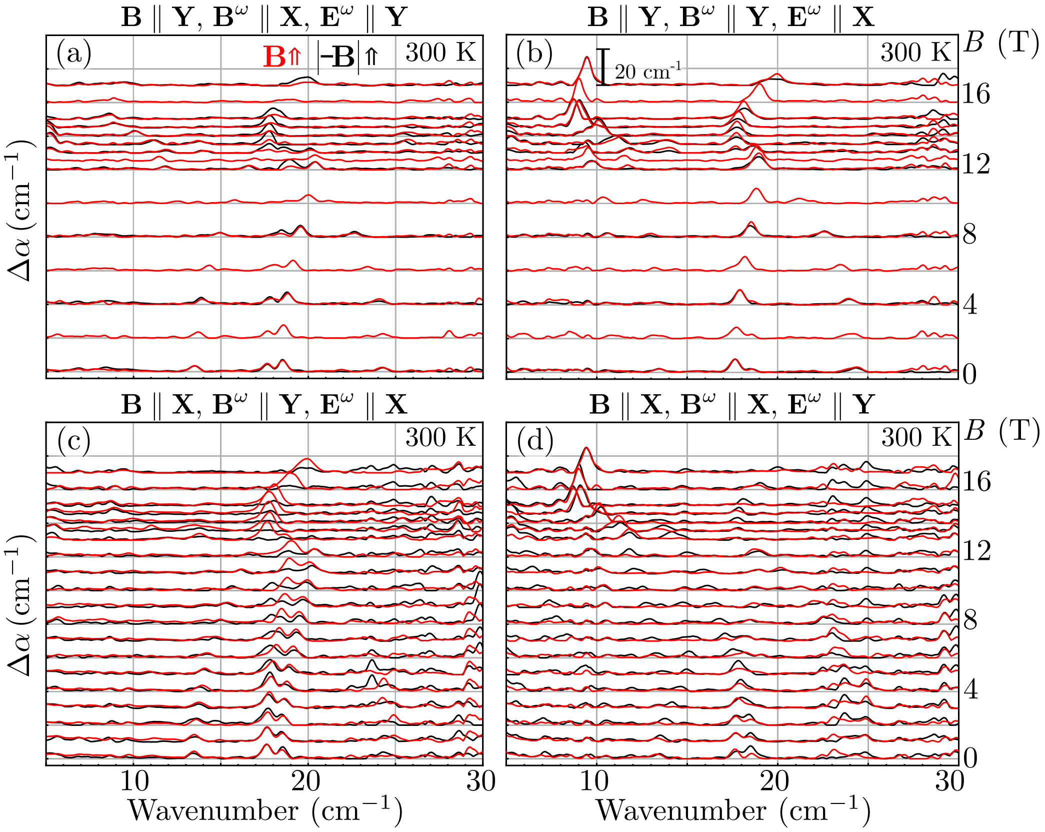

Figure 5.17: Magnetic field dependent spectra in positive and negative fields to measure nonreciprocal directional dichroism for different magnetic field directions and light polarizations. Spectra measured in positive increasing fields are plotted with red, spectra recorded in negative fields with increasing magnitude are plotted with black. The absorption curves are vertically shifted by a constant proportional to the magnitude of the magnetic field **B**.

The magnetoelectric sum rule discussed in Chapter 2, Eq. (2.21) connects the NDD observed at finite frequencies to the static ME susceptibility, thus, it allows the identification of resonances responsible for the DC response. There is a $1/\omega^2$ dependence of the susceptibility, meaning that the strongest contributions to the static ME effect come from low-frequency excitations. In the present case, when the effect is the highest, [configuration $\mathbf{B} \parallel \mathbf{X}$, $\mathbf{B}^{\omega} \parallel \mathbf{Y}$, $\mathbf{E}^{\omega} \parallel \mathbf{X}$, panel (c) in Fig. 5.17] the contribution at 14 T is 3.3 ps/m, calculated from Eq. (2.21). This is far less, than the value of 210 ps/m, that was reported in Ref. [143], where the ME response of $\mathrm{BiFeO_3}$ is measured. That measurement was sensitive to χ^{me}_{YY}: increasing the magnetic field in the $\mathbf{Y}$ direction, and measuring the electric polarization also in the $\mathbf{Y}$ direction. In my case, the measurement corresponding to χ^{me}_{YY} can be seen on panel (b) of Fig. 5.17, where the effect is even smaller than in the largest case, panel (c), which probes χ^{me}_{YX}. To see the deviation more clearly, we would need electric polarization measurements that also probe χ^{me}_{YX}. This may be done by either the rotation of a static field or by adding a small oscillatory field perpendicular to the static field. According to Eq. (2.21), a resonance at lower frequencies can account for the missing contribution, as a smaller ω resonance frequency in the denominator would result in a large value. Domain wall effects, for example, happen at lower frequencies [186–188], our measurements however were already initialized in a monodomain state, meaning there are no expected domain walls. The simulations discussed in the next section do not predict any resonance frequencies that lie lower than the low-frequency cutoff of our experiments either.

5.3.6 Modeling of excitations

Our theoretician colleagues – L. Rózsa, L. Szunyogh and L. Udvardi – developed a spin dynamics simulation to explain the resonances in the transverse conical phase. I took part in the discussions and include these results in my thesis to provide a complete picture for the reader. A more detailed description can be found in our publication [P2] and further in Ref. [189].

The simulations are based on the Hamiltonian in Eq. (5.1) with the approximation $K_H = 0$, which is often used in the literature [173]

$$\begin{aligned}\mathcal{H} =& J_1 \sum_{\langle i,j\rangle} \mathbf{S}_i \cdot \mathbf{S}_j + J_2 \sum_{\langle i,j\rangle'} \mathbf{S}_i \cdot \mathbf{S}_j \\ &+ D_1 \sum_{\langle i,j\rangle} \left(\mathbf{Z} \times \mathbf{e}_{ij}/a\right)\left(\mathbf{S}_i \times \mathbf{S}_j\right) \\ &+ D_2 \sum_{\langle i,j\rangle} (-1)^{h_i} \mathbf{Z}\left(\mathbf{S}_i \times \mathbf{S}_j\right) \\ &- K \sum_i S_{iZ}^2 + g\mu_\mathrm{B} \sum_i \mathbf{S}_i \cdot \mathbf{B},\end{aligned} \tag{5.3}$$

where a is the pseudocubic lattice constant. The Fe ions are on the $\mathbf{R}_i$ sites, with a $\mathbf{S}_i$ classical spin vectors, for which $S = 5/2$. Nearest neighbors $\langle i,j\rangle$ are connected: $\mathbf{R}_j = \mathbf{R}_i + \mathbf{e}_{ij}$. J_1 and J_2 are nearest and next-nearest neighbor antiferromagnetic interaction exchange coupling terms. D_1 and D_2 are the homogeneous and the

	J_1 (meV)	J_2 (meV)	D_1 (μeV)	D_2 (μeV)	K (μeV)
set #1	4.9	0	177	77.3	3.1
set #2	4.9	0.17	177	77.3	3.1

Table 5.1: Exchange (J_1, ,J_2), Dzyaloshinskii-Moriya (D_1, D_2) and anisotropy (K) parameters used in the simulations.

staggered components of the nearest-neighbor DM interaction. The hexagonal layers are labeled with $h_i = \sqrt{3}\mathbf{R}_i \cdot \mathbf{Z}/a$, the easy-axis coupling constant is denoted by K. The external magnetic field is $\mathbf{B}$, μ_B is the Bohr-magneton, and the g-factor is $g = 2$. The model parameters are displayed in Table 5.1.

The simulations were done on 6 layers along the $\mathbf{Z}$ direction, while periodic boundary conditions were applied along all directions, containing one period of the cycloid. The system size was larger in the direction of the wavevector, i.e., $\mathbf{X}$ perpendicular to the field direction for modeling the cycloidal structure and $\mathbf{Y}$ along the field for the conical spiral, while kept minimal in the perpendicular directions. The spiral period, which is the length of the cell's long side, was optimized at each magnetic field value.

The energies were then found by taking the harmonic spin cycloid as the initial state of the system. The energy of this state was first minimized by the numerical solution of the Landau-Lifshitz-Gilbert equation, then, by aligning the spins with the direction of the local effective magnetic field, speeding up the relaxation. The relaxation was stopped when the torque sensed by the spins were negligibly small. This optimized state was used as the ground state for the linear spin-wave calculations. From the spin-wave eigenvectors, the response function $|\chi_0^\mathrm{n}|^2$ proportional to the magnetic dipole strength of the mode was determined [189].

The spin-wave resonances obtained from these calculations are compared to the experimental data in Fig. 5.18. On panel (a), the excitations are calculated with parameter set #1, given in Table 5.1. These coupling constants are optimized to fit the cycloidal wavelength of 62 nm, the zero-field frequencies of the cycloidal excitations, and the high-field two-sublattice antiferromagnetic resonance frequencies [184, 185] given by

$$\omega_{\nu_2} = \gamma\sqrt{B^2 + BB_D} \tag{5.4}$$

$$\omega_{\nu_1} = \gamma\sqrt{BB_D - 2B_EB_A + B_D^2}, \tag{5.5}$$

where γ is the gyromagnetic ratio, and the effective fields are $B_D = \frac{z_1 D_2 S}{g\mu_B}$, $B_E = \frac{z_1 J_1 S}{g\mu_B}$, $B_A = \frac{2KS}{g\mu_B}$, where $z_1 = 6$ is the number of nearest neighbors. The Φ_n in-plane, and Ψ_n out-of-plane excitation frequencies of the zero-field cycloidal state may be well approximated by $\omega_{\Phi_n} \approx \gamma\sqrt{B_E B_L^2/(2B_S)n^2}$ and $\omega_{\Psi_n} \approx \gamma\sqrt{B_E B_L^2/(2B_S)\left(n^2+1\right)}$, respectively, with $B_L = \frac{2D_1 S}{g\mu_B}$ and $B_S = \frac{(J_1-4J_2)S}{g\mu_B}$ [173, 176]. Index n is a non-negative integer, that labels the spin-wave modes at nQ; $Q = 2\pi/\lambda$, where $\mathbf{Q}$ is the cycloidal ordering vector. The ratio $2\pi\left(2B_S\right)/B_L$ is the period of the cycloid in units of a in $\mathbf{B} = 0$. The period and the frequencies are perturbed in combination by the anisotropy $B_E B_A$. For dealing with fewer free parameters, first, J_2 was set to zero, $J_2 = 0$. The remaining four parameters describe the magnetic field dependence of the modes in the cycloidal and in the CAFM phases well, along with the lower critical field B_1. The model also describes correctly the spin motions in the cycloidal phase labeled with Φ_n and Ψ_n, as they are indeed in-plane and out-of-plane oscillations. The parameter values in set #1 are close to, although somewhat lower than the ones that describe the low-temperature resonances [29, 179, 185]. The lowered values of the interaction parameters are in agreement with the lowered excitation frequencies obtained from the high-temperature experiments.

In the transverse conical state, the field dependence of the resonances is qualitatively described by set #1, the resultant q vector is almost field-independent, supported by neutron scattering experiments discussed earlier in this chapter, as well as in Ref. [164]. The set #1, however, with all the good qualitative agreements, gives systematically lower frequencies for the resonances compared to the experimental data, and predicts a considerably lower upper transition field $B_{c2} \approx 13.8\,\mathrm{T}$. The critical field B_{c2} is the threshold, below which the CAFM phase becomes unstable against periodic modulations [190]. The equation for this criterion can be formally expressed with the frequencies of the modes in the CAFM phase at B_{c2} and the zero field cycloidal frequency Ψ_0:

$$\omega_{V_2}\left(B_{c2}\right) + \omega_{V_1}\left(B_{c2}\right) = 2\omega_{\Psi_0}. \tag{5.6}$$

As a consequence, the zero-field spin-wave frequencies and the frequencies of the modes in the CAFM phase fix the critical field B_{c2}, no tuning of the other parameters will have effect on its value. A finite value of J_2 introduced in the original parameter set , called set #2 in Table 5.1, extends the stability range of the modulated phases, and the CAFM phase appears only above $B_{c2} \approx 15\,\mathrm{T}$. At the same time, the magnetic field range where the energy of the conical state is lower than the cycloidal, is very narrow, between 14.9 and 15 T. Even though the conical state is not a global energy minimum below 14.9 T, it is a local minimum, that allows the calculation of the excitations of this metastable state. In Fig. 5.18 (b), these calculated spin-wave resonances of the conical state are shown in the $13-15\,\mathrm{T}$ range. The modes are shifted to higher frequencies and thus the correspondence with the experimental data is improved. On the other hand, increasing

J_2 reduces exchange stiffness, and that leads to longer cycloidal q vector and thus increased spin-wave frequencies in the cycloidal phase.

In the conical phase, two kinds of eigenvectors come from the calculations. One group possesses an oscillating magnetic moment parallel to the static field, labeled by Λ_n, the other group, labeled by Σ_n, has the oscillating magnetic moment perpendicular to the external field. The lowest-energy mode of the conical phase, Λ_1, that is mode #1 in Fig. 5.16, corresponds to the opening and closing of the cone angle. It decreases in frequency, and loses strength with the field increasing toward B_{c2}. Experimentally it was found, that mode #2 is not very sensitive to an in-plane $\mathbf{B}^{\omega}$, it is assigned to Λ_2. Mode #3, with a similar behavior, can likely be assigned to Λ_3, though it may overlap with Σ_1, that appears at a very close energy according to the calculations. I could not deduce selection rules for mode #4, but by checking its field dependence, or the lack thereof, it is clearly Σ_2 of the calculations. Mode #5 could be either the pair (Σ_3,Λ_4) or (Σ_4,Λ_5), since they are almost degenerate in the calculations. In Fig. 5.18 (a), the intensity of (Σ_3,Λ_4) is so low, that they are not visible, but experimentally, $\Sigma_3,\Sigma_4,\Lambda_4$ and Λ_5 cannot be distinguished. Moreover, some of these modes are present in experimental configurations where the magnetic dipole selection rules do not predict their appearance. These modes may be excited by the oscillating electric field through the strong magnetoelectric effect detected in the conical phase.

A unique optimal parameter set that describes the resonances in all three phases as well as the critical fields quantitatively was not found. Magnetostriction was observed through the phase transition [143], that is not accounted for in the field-independent parameter set might explain these discrepancies. However, at low temperatures, the introduced magnetostriction parameters were used to explain the anisotropy of the resonances in the CAFM phase [185]. In my high temperature experiments, the resonances of the CAFM phase were not sensitive to the in-plane rotation of the static magnetic field, as it is visible in Fig. 5.16. Furthermore, additional anisotropy parameters should also not change the result of Eq. (5.6), i.e., the upper critical field B_{c2}. Since sufficient data is lacking to determine the change of the model parameters caused by the magnetostriction, we propose the model presented above, with two values of J_2 to quantitatively describe the critical fields and the spin-wave frequencies in the three phases.

5.3.7 Summary

During my work with $BiFeO_3$, I mostly investigated the high-temperature transverse conical phase. Initially motivated by preliminary neutron scattering data, I used SANS experiments to reveal a field-induced modulated structure at high temperatures, where the modulation vector aligns parallel to the external field, unlike the cycloidal phase. By connecting these findings with magnetization

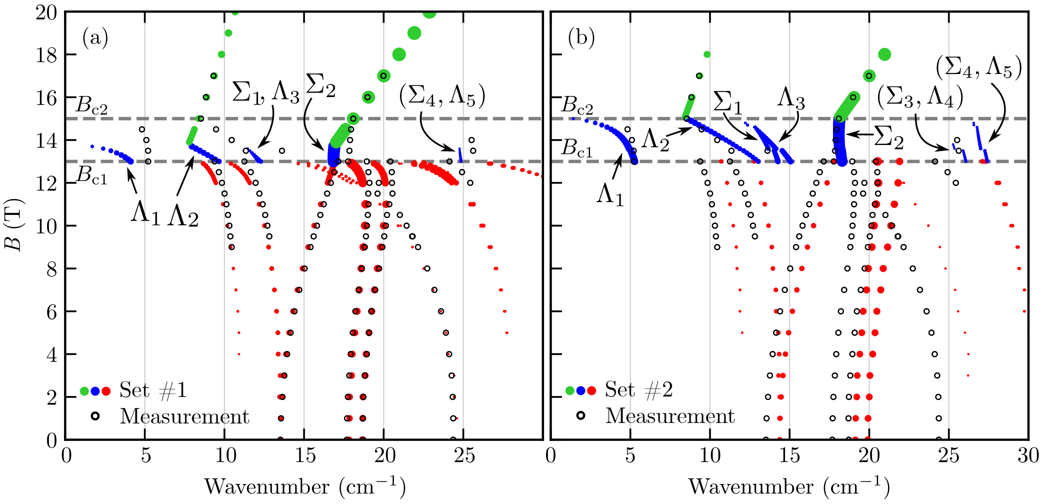

Figure 5.18: Colored and empty circles show the resonance positions of the three magnetic phases in BiFeO$_3$ obtained from simulations using the model Hamiltonian of Eq. (5.3) and from THz absorption experiments done in external magnetic fields parallel **Y**, respectively. Panel (a) and (b) show simulations ran with parameter set #1 and set #2, plotted together with the same experimental data. Red, blue and green dots show the theoretical frequencies in the cycloidal, transverse conical and canted antiferromagnetic (CAFM) phases, respectively. The size of the dots is proportional to the magnetic dipole strength of the given mode. Λ_n and Σ_n correspond to excitations with oscillating magnetic moments parallel and perpendicular to the external static field, respectively. Gray dashed horizontal lines mark the transition fields between the cycloidal and conical (B_{c1}), and the conical and CAFM (B_{c2}) phases in the experiments.

measurements, we established the existence of a transverse conical phase, as previously proposed by S. Kawachi et al. [143]. Next, we explored the spin excitations in this phase, identifying at least five distinct modes, two of which evolve into the excitations of the CAFM phase. Notably, we observed directional dichroism for certain modes, a direct consequence of the magnetoelectric coupling. Through collaboration with theorists, we successfully modeled the field dependence of these modes providing parameters for the microscopic interactions.

Chapter 6

Broadband microwave spectroscopy in $MnSc_2S_4$

$MnSc_2S_4$ is a prominent example of a magnetically frustrated material, showcasing interesting phenomena as a consequence. Frustration in a magnetic system means that not all interactions can be satisfied completely at the same time, i. e., the global energy minimum is not the sum of the local minimal energies. It hinders the formation of a long-range ordered ground state, and instead, a manifold of degenerate ground states forms. Frustration can originate from the lattice geometry. One of the simplest example is realized on a single equilateral triangle of Ising spins with antiferromagnetic interaction between them [191]. It is not possible to arrange the spins so that the pairwise interaction energy is minimal for all three spins. Instead, there are six equivalent configurations that can be the ground state. For Heisenberg spins, the arrangement where the spins point 120° with respect to each other is a compromise where the system reaches the global energy minimum.

Frustration can also emerge from conflicting exchange interactions, e.g., considering spins as classical vectors on a one-dimensional chain with $J_1 < 0$ ferromagnetic nearest-neighbor (NN) and $J_2 > 0$ antiferromagnetic next-nearest-neighbor (NNN) interactions: $\mathcal{H} = J_1 \sum_i \mathbf{S}_i \cdot \mathbf{S}_{i+1} + J_2 \sum_i \mathbf{S}_i \cdot \mathbf{S}_{i+2}$. When the ratio of of $|J_2|/J_1|$ exceeds a certain threshold, which, for the present Hamiltonian is 1/4, the ground state is an incommensurate non-collinear spin-spiral [192]. There are two degenerate spiral solutions, with clockwise and counter-clockwise rotation of the neighboring spins.

The cubic spinel $MnSc_2S_4$ realizes the latter case. Although the magnetic Mn^{2+} ions form a bipartite diamond lattice, magnetic order sets in only below 2.3 K despite that the Curie-Weiss temperature is an order of magnitude larger [193]. The competing exchange interactions between the Mn spins lead to a manifold of spin spiral states [194]. As it will be discussed below, the fluctuating state of these spirals can be classified as a spiral spin-liquid whereas, below the

Néel temperature, a complex magnetic phase diagram with helical order and antiferromagnetic skyrmion lattice were identified [195, 196]. Magnetic skyrmions are topologically non-trivial spin vortices that emerge due to magnetic frustration [197–202]. They are topologically protected, i.e., characterized by a topological integer that cannot be changed upon continuous deformation, and have localized, particle-like properties [203].

In this chapter, the reader is going to get an insight to my efforts to detect the excitations of the intriguing magnetic structures in $\mathrm{MnSc_2S_4}$. I performed THz spectroscopy down to the mK temperature range up to 17 T and 100 $\mathrm{cm^{-1}}$, as well as microwave transmission spectroscopy up to 50 GHz above and below the ordering temperature. The broad temperature and magnetic field range that my experiments covered allowed me to search for the collective modes in each phase.

6.1 The magnetic phase diagram of $\mathrm{MnSc_2S_4}$

$\mathrm{MnSc_2S_4}$ is an insulating material, that crystallizes in the spinel structure shown in Fig. 6.1 (a). This structure (space group $Fd\overline{3}m$) is known originally from the gemstone $\mathrm{MgAl_2O_4}$ named spinel. The general formula for the structure is AB_2X_4, where A and B are metals, and X is usually a chalcogen, such as oxygen or sulfur. In normal spinels, B cations occupy the octahedral sites, which form a pyrochlore lattice, whereas the A cations sit on the tetrahedral sites realize a diamond lattice. The pyrochlore lattice has geometric frustration, however, in this compound, the non-magnetic Sc ions occupy these sites. As half-filled $3d$ shell $\mathrm{Mn^{2+}}$ ions with $S = 5/2$ spins and zero orbital moment form the bipartite diamond lattice [see Fig. 6.1 (b)], the frustration is not geometrical, it rather originates from the competing interactions.

The magnetic susceptibility has been measured between 1.7 and 400 K [193], shown in Fig. 6.2 (a). From that, the Néel temperature was determined $T_\mathrm{N} = 2.3\,\mathrm{K}$. The susceptibility χ^m is fitted using the Curie-Weiss formula

$$\chi^m = \frac{C}{T - \Theta_\mathrm{CW}}, \tag{6.1}$$

where C is the Curie-constant related to the size of the magnetic moments, and Θ_CW is the Curie-Weiss temperature, which measures the dominant magnetic interaction. The sign of Θ_CW indicates the type of the magnetic ordering of the material. If $\Theta_\mathrm{CW} > 0$, the material in question is a ferromagnet, and for antiferromagnets, $\Theta_\mathrm{CW} < 0$. The fit to the inverse susceptibility of $\mathrm{MnSc_2S_4}$ yields $\Theta_\mathrm{CW} = -22.9 \pm 0.8\,\mathrm{K}$, indicating antiferromagnetic interactions. The inverse susceptibility curve reveals more than just the typical strength of the interactions and the antiferromagnetic ordering temperature. An additional downturn of the

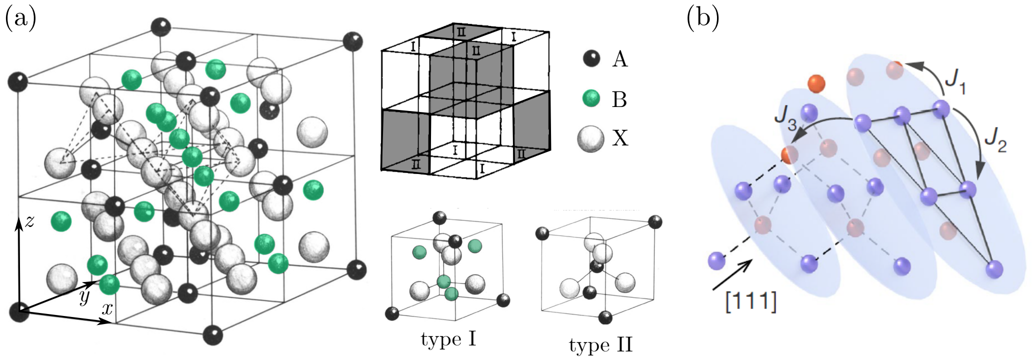

Figure 6.1: (a) Normal spinel structure AB_2X_4. The large cubic unit cell contains eight octants of type I and type II cubic cells. The type I octant contains A cations, that are tetrahedrally coordinated. Type II octant contains B cations in octahedral coordination so that the octahedron extends beyond the boundaries of the octant. The octants are placed in a checkerboard pattern [204]. (b) Bipartite diamond lattice of the Mn^{2+} ions in MnSc$_2$S$_4$. One sublattice is one triangular layer as viewed from the [111] direction. Reproduced from Ref. [195].

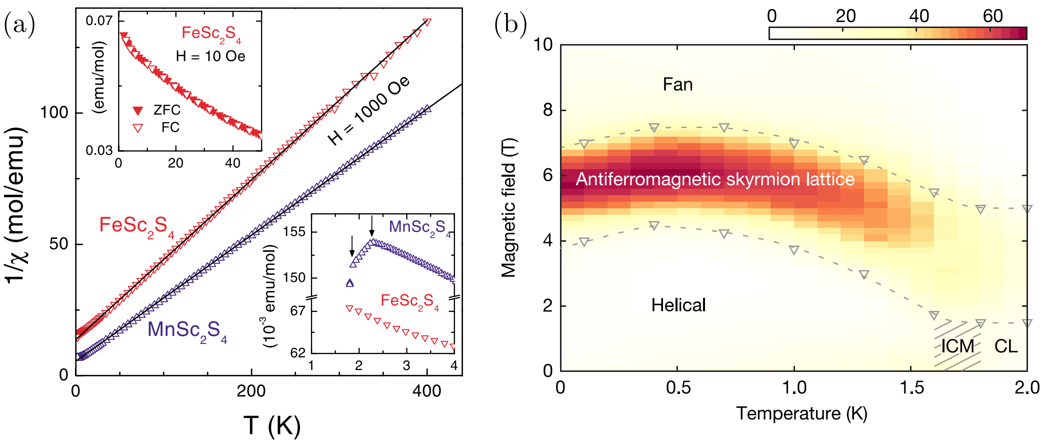

Figure 6.2: (a) Inverse magnetic susceptibility curves of MnSc$_2$S$_4$ and FeSc$_2$S$_4$ up to 400 K. Lower inset: Temperature dependent susceptibility between 2 K and 4 K. Reproduced from Ref. [193]. (b) Magnetic phase diagram of MnSc$_2$S$_4$ for external field direction $\mathbf{B} \parallel [111]$ based on neutron scattering data. CL stands for the collinear, ICM for incommensurate phases. Reproduced from Ref. [195].

susceptibility below T_N suggests potentially more complex structures to emerge in MnSc$_2$S$_4$.

The comparison of $|\Theta_{CW}|$ to the actual ordering temperature T_N gives a parameter for the level of frustration $f = \frac{\Theta_{CW}}{T_N}$, in MnSc$_2S_4$ $f \approx 10$ [193]. A material with no frustration would have $f = 1$, as the ordering happens at the Curie-Weiss temperature. Typical realistic materials with no significant frustration usually have f between $2-5$, because of the effect of further neighbor interactions. We talk about a strongly frustrated magnet, when the transition temperature is suppressed so that $f > 10$ [205]. There are even reported cases for $f > 100$ [205, 206], such as 2D magnets SrCr$_8$Ga$_4$O$_{19}$ with $f = 150$ [207], or NaTiO$_2$, with $f > 500$ [208], but for FeSc$_2$S$_4$, the sister compound of MnSc$_2$S$_4$, $f > 900$ as no ordering temperature was found down to 50 mK [193].

The frustration index of MnSc$_2$S$_4$ already indicates strong frustration. This was also confirmed by neutron diffraction and diffuse scattering experiments [194], where they found the ratio $|J_2/J_1| = 0.85$, the highest value among A-site spinels. Elastic neutron scattering experiments, combined with inelastic neutron scattering (INS) experiments [195] revealed a multi-step ordering process of the spiral spin-liquid. The obtained magnetic phase diagram of MnSc$_2$S$_4$ is shown in Fig. 6.2. Above T_N, the fluctuations are correlated on the mesoscopic scale, and the material is in a novel, so-called spiral spin liquid state, but essentially paramagnetic. This state then orders to a sinusoidally modulated collinear phase at T_N, which becomes incommensurate below 1.64 K, and subsequently transforms to a helical state below 1.46 K, in agreement with the predictions of the susceptibility curve. Neutron scattering experiments conducted in finite magnetic fields also reveal a multi-**q** state. Based on the different magnetic Bragg peak selection of this multi-**q** state under external fields parallel [100], [110] and [111] directions, this state was proposed to be a triple-**q** phase between approximately 4 and 6 T. Based on Monte Carlo simulations, the triple-**q** phase was assigned to an antiferromagnetic skyrmion lattice (AF SkL) structure [195, 196]. This structure illustrated in Fig. 6.3 consists of three sublattices, that form a 120°-type antiferromagnetic order. The magnetic unit cell of AF SkL consists of six triangular layers. One layer hosts the three sublattices of the 120°-type antiferromagnetic order.

INS measurements [195] measured the magnetic interaction parameters to be $J_1 = -0.31$ K, $J_2 = 0.46$ K, $J_3 = 0.087$ K as labeled in Fig. 6.1 (b). Therefore, the ferromagnetic nearest neighbor (NN) interaction J_1 competes with the antiferromagnetic next nearest neighbor (NNN) interaction J_2, which leads to a spin spiral state with massive frustration [210], however, in order to explain the neutron spectrum and the stability of the phases even the third neighbor interaction J_3 should be included.

Very recently, thermal Hall-effect measurements were also carried out in

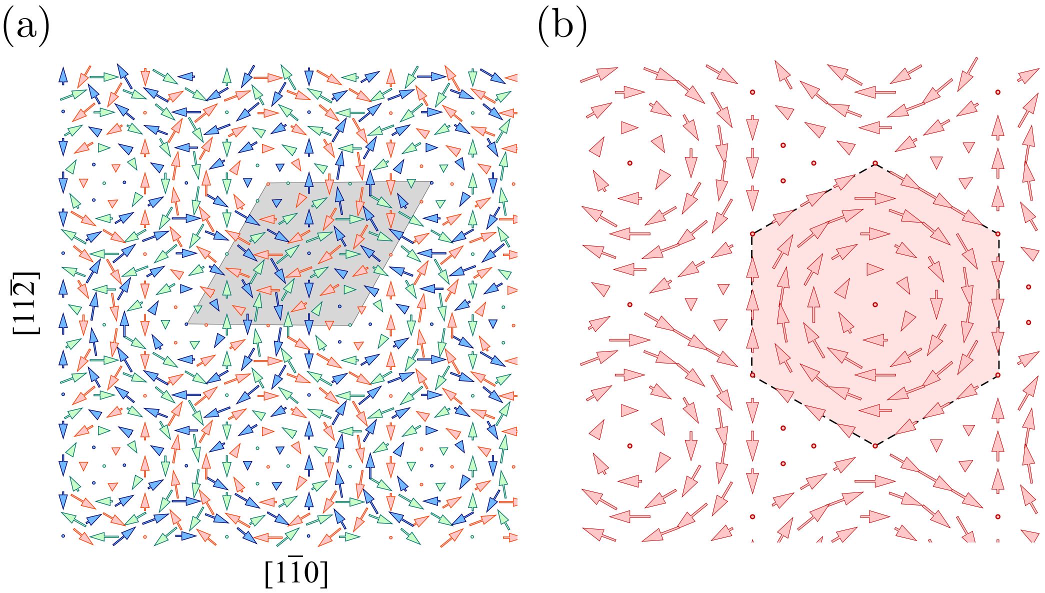

Figure 6.3: (a) Antiferromagnetic (AFM) skyrmion lattice formed on three sublattices colored with red, blue and green arrows (b) One sublattice of the three sublattices that form the AFM skyrmion. Both panels reproduced from Ref. [209].

MnSc$_2$S$_4$ [209]. The magnetic field dependence of the longitudinal thermal conductivity κ_{xx} is sensitive for the different magnetic phases and it shows anomalies at the phase transitions. Moreover, non-zero thermal Hall-effect shows up in the antiferromagnetic skyrmion phase. The authors attribute the transverse thermal response to the non-trivial topology of the antiferromagnetic spin texture, which leads to finite Berry curvature for magnons carrying heat.

6.2 Magnetic resonance spectroscopy in MnSc$_2$S$_4$

A spin spiral has a periodicity larger than the chemical unit cell, causing the spin-wave dispersion to fold into the smaller magnetic Brillouin-zone, and may show up as a series of excitations at the Γ-point. Such modes associated with the distortion of the phase or collective tilt of the spiral-plane have been identified in many material families. From the perspective of my thesis, the most important compound is BiFeO$_3$ [156, 157, 175], as it was discussed in Chapter 5. Other examples are reported in orthorhombic manganites [211], cubic chiral helimagnets [212, 213] or Cu$_2$OSeO$_3$ [214]

Multi-**q** states can show up as additional modes in the excitation spectrum, which is the case for skyrmions, where a breathing, a clockwise and a counterclockwise (i.e., rotational) mode were predicted and observed [213–216]. Analytical calculations and numerical simulations were made on a synthetic antiferromagnet constructed as two thin ferromagnetic layers coupled antiferromagnetically, both of which host a ferromagnetic skyrmion lattice, thus hosting together an antiferromagnetic skyrmion lattice [217–221]. These calculations show that the coupling between the layers splits the breathing and rotational modes into in-phase and out-of-phase modes. An out-of-phase breathing mode means that the skyrmion is at a maximal size in one layer (sublattice), while it has minimal size in the other layer (sublattice), traces of the mode would be observable in the GHz range. Motivated by these former successful examples predicting modes in the microwave regime, I studied the spin excitations in $MnSc_2S_4$ to look for the collective modes of the proposed fractional antiferromagnetic skyrmions.

6.2.1 THz spectroscopy at mK temperatures

THz absorption measurements were done in collaboration with Estonian colleagues T. Rõõm, U. Nagel and K. Amelin at KBFI Tallinn, with an SPS-200 THz FTIR spectrometer, that is described in Chapter 3. Ultra-low temperatures in the mK range were reached in an Oxford TLE200 dilution refrigerator.

First, field dependent absorption spectra were recorded at 2.5 K between 100 GHz and 3 THz, for polarizations $\mathbf{B}^{\omega} \perp \mathbf{B}$ and $\mathbf{B}^{\omega} \parallel \mathbf{B}$, where $\mathbf{B}$ lies in the (111) plane. The differential absorption spectra are obtained as described in Section 3.1.2, and are shown in Fig. 6.4 (a). The graph shows the region between 100 GHz and 650 GHz only, because no magnetic field dependent spin excitations were found at higher frequencies up to 3 THz. According to the susceptibility measurement shown in Fig. 6.2 (a), 2.5 K is in the paramagnetic phase. A single excitation can be seen when the oscillating field is perpendicular to the external field, and none when the oscillating field is parallel to the external field, which is in agreement with a paramagnetic resonance. The wavy baseline of the spectra in the vicinity of the resonance peak is a sign that the interference pattern of the multiple reflections from the nearly plane-parallel sample is changed by the magnetic-field.

In order to fit the transmission spectrum, I model the sample as a parallel slab with dielectric constant ε and take into account the complex response of the resonance assuming a Lorentzian line in the magnetic susceptibility

$$\chi(\omega) = \frac{S}{\omega_0^2 - \omega^2 - i\omega\gamma}, \tag{6.2}$$

where ω_0 is the resonance frequency of the oscillator, S is the oscillator strength and γ is the damping parameter. Multiple reflections are taken into account as a Fabry-Perot etalon with infinite number of reflections. Considering the resonance absent in zero-field, this model provides an estimation for the THz dielectric constant

$\varepsilon = 12.1$. From the Lorentzian oscillator fits, I extracted the resonance peak positions and made a linear fit to them, that resulted in a slope of 27±0.6 GHz/T with a zero-field offset of 20.4±7.2 GHz. This slope corresponds to a g-factor of 1.93±0.05. I observed no deviations from the linear behavior of the resonance, suggesting very small anisotropy in the parameters of the spin Hamiltonian. The g-factor, also a measure of the spin-orbit coupling, of nearly the free electron value of 2, is consistent with the small anisotropy.

Below 1.5 K, the modulated magnetic structures emerge. We performed THz absorption spectroscopy at 300 mK for $\mathbf{B} \parallel [111]$, where neutron scattering signal assigned to the AFM skyrmion lattice phase was obtained between 4.2 and 7 T. Magnetic-field dependent absorption spectra were recorded with unpolarized light between 100 GHz and 2.1 THz. The differential absorption spectra are shown in Fig. 6.4 (b) between 100 and 650 GHz, following a similar field dependence as the spectra recorded at 2.5 K. I fitted these resonance positions as well; the linear fit gave a slope of 27.5 ±0.4 GHz/T, corresponding to a g-factor of 1.96 ± 0.02, with a zero-field offset of 9.5 ± 1.5 GHz. The g-factor appears to be the same value within the error of measurement, as the one in the paramagnetic phase, while the intercept is somewhat smaller.

I could not resolve any deviation from the linear behavior of the spin resonance observed in the absorption spectra. Furthermore, the resonance at 300 mK is not sensitive to the magnetic transition fields determined in Ref. [195], while no other resonances showed up in the experimentally covered frequency range. The absence of additional modes may be explained by the weak magnetic anisotropy of the Mn^{2+} ions. Without substantial anisotropy, the harmonic spin spiral modes that are folded into the Brillouin zone remain silent. The oscillation of the plane of the harmonic spiral may induce modulation of the electric polarization through the inverse Dzyaloshinskii-Moriya coupling, however, this mechanism is active only for spin cycloids, thus it cannot generate infrared active modes in the helical state of $MnSc_2S_4$.

From the absorption, the static magnetic susceptibility can be calculated using the Kramers-Kronig relations, assuming the dielectric function ε to be a constant, and that χ^m is small [222]

$$\chi^m(\omega \to 0) = \frac{2}{\pi} \frac{c}{\sqrt{\varepsilon}} \int_0^\infty \frac{\alpha(\omega)}{\omega^2} \mathrm{d}\omega, \tag{6.3}$$

where α is the absorption coefficient, ω is the angular frequency and c is the speed of light in vacuum. To calculate $\chi^m(\omega \to 0)$, I fitted the experimental differential absorption spectrum at 12 T with one resonance. By evaluating the integral in Eq. (6.3), I got $\chi^m(\omega \to 0) = 2.5 \times 10^{-3}$. Comparing this to the reported value of $\chi_0^m = 0.021$ at T_N [193], the difference is quite considerable, one order of magnitude. The susceptibility obtained from my measurements is a transverse

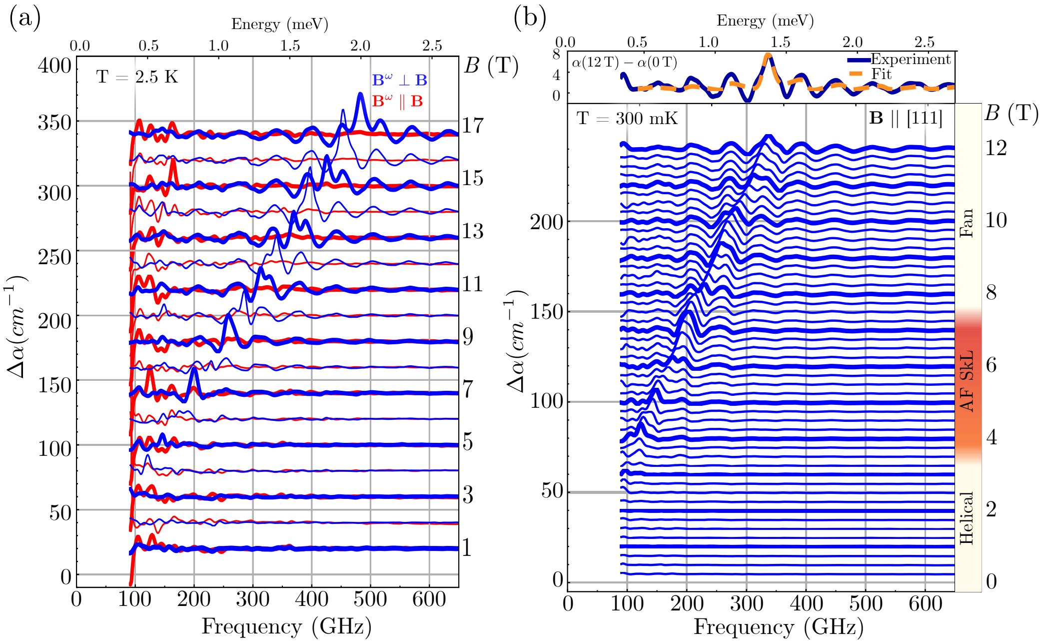

Figure 6.4: (a) Magnetic-field dependent THz absorption spectra of $MnSc_2S_4$ measured in Voigt configuration for two polarizations up to 17 T at $T = 2.5$ K. Bold lines are spectra measured at odd magnetic field values. The undulation of the spectra in the vicinity of the resonance is the result of the distorted multiple reflections of the nearly plane-parallel sample, because of changes in the refractive index of the sample near the spin resonance. (b) *Bottom panel:* Magnetic-field dependent THz absorption spectra of $MnSc_2S_4$ measured in Faraday configuration for unpolarized light up to 12 T at $T = 300$ mK. Spectra measured at integer valued fields are plotted with bold lines. *Top panel:* Blue curve is the differential absorption spectrum measured at 12 T, the red dashed curve is the fit of the Lorentzian model. *Side bar:* Magnetic phase diagram at 300 mK: helical, antiferromagnetic skyrmion lattice (AF SkL), and fan structure, according to Ref. [195].

component, while the value of Ref. [193] is the longitudinal. However, as the anisotropy is weak and the magnetization curve is nearly linear in the magnetically ordered phases [193, 195], these two components are expected to be nearly equal in the static limit. The missing spectral weight from the THz measurements has to lie outside the frequency window of the experiment. This implies the presence of additional resonances below 100 GHz, the low-frequency cutoff of the THz experimental setup. An antiferromagnetic spin spiral emerging as a result of exchange frustration, that is a building block of an AF skyrmion, has three gapless modes in the absence of anisotropy. A phason mode that corresponds to rotations withing the spiral plane, and two additional modes related to out-of-plane rotations [223]. A magnetic anisotropy may introduce a gap to these modes, allowing to observe them with microwave spectroscopy. It is worth noting that in the case of $ZnCr_2O_4$ it was conjectured, that the missing spectral weight in the susceptibility may be explained by the presence of non-resonant relaxation modes [224].

6.2.2 Low-temperature microwave spectroscopy

To investigate lower frequency spin resonances, I performed broadband microwave spectroscopy measurements with a VNA in a dilution refrigerator as well as in a regular cryostat with a variable temperature insert (VTI). The experiments were done in Stuttgart, with the help of M. Scheffler, and A. Bauernfeind.

Measurements were done in the paramagnetic phase in the 10 MHz to 20 GHz frequency range between 0 and 1 T, at temperatures $T = 2$, 6, 10 and 20 K, shown in Fig. 6.5. The magnetic field was applied along $\mathbf{B} \parallel [111]$. At 6, 10 and 20 K, a single linear resonance is visible, whose g-factor calculated from the slope of a linear fit is 2.1, 2.08 and 2.07, respectively. As the temperature approaches the Néel temperature, the linewidth of the resonance broadens and the the resonance vanishes, making the magnetic field-frequency map of Fig. 6.5 (d) completely featureless.

Microwave experiments were also carried out at low temperatures, in the magnetically ordered phase, the results of which are shown in Fig. 6.6. The parameters were extended: the upper frequency limit of the equipment was 50 GHz, and the covered magnetic field range was the $0-8$ T range, all this in the $300-600$ mK temperature range. Despite the efforts to cover a very large parameter space, I did not observe any magnetic spin excitations in the ordered phases with these measurements.

Combining these results with the previous THz data, I suggest that the zero-field excitation of $MnSc_2S_4$ occurs between 50 and 100 GHz, so the spin gap opens in that range below T_N.

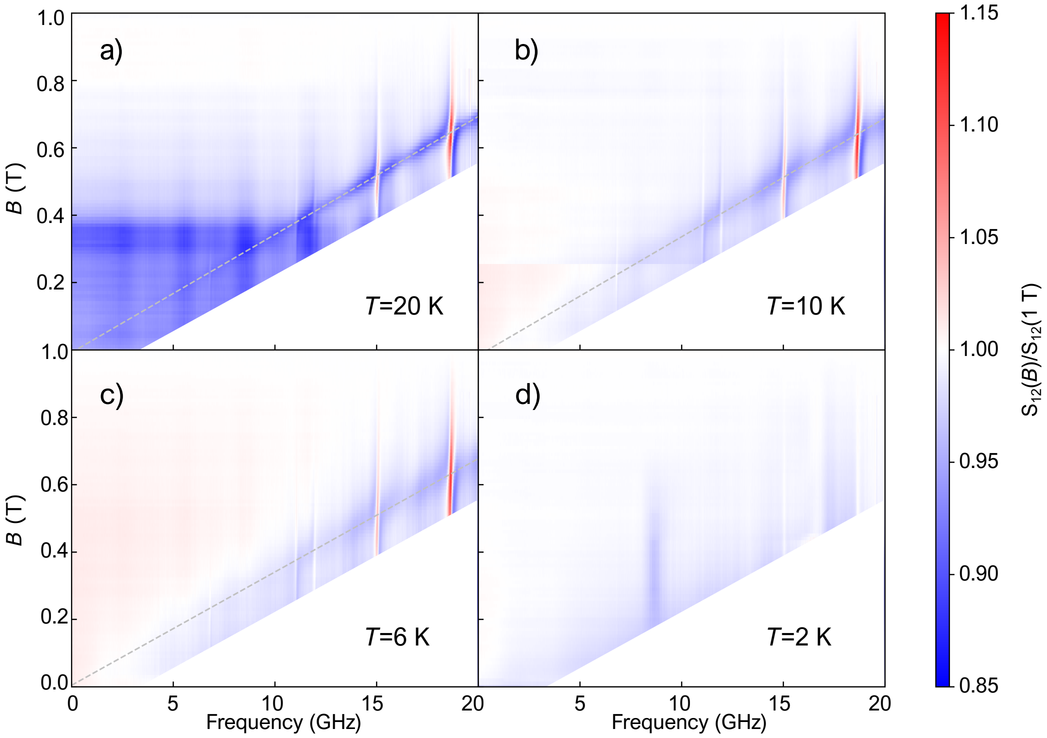

Figure 6.5: Low frequency broadband transmission divided by a reference spectrum at 1 T a)–c) in the paramagnetic temperature range, and d) below the magnetic ordering temperature. The gray dashed line in a)–c) is the linear fit to the resonance line.

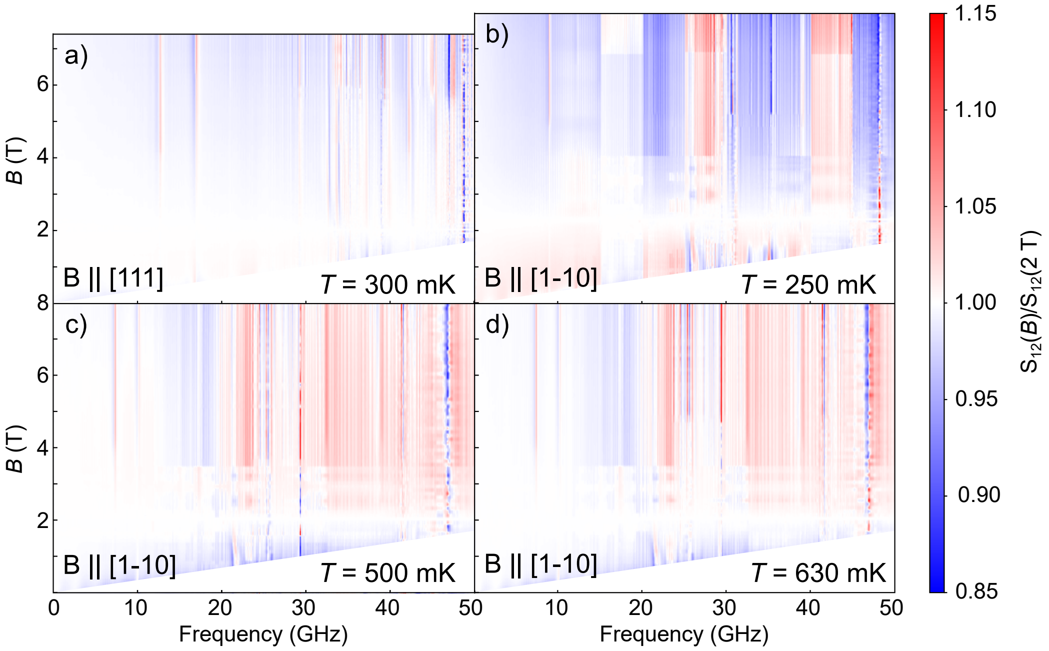

Figure 6.6: Low temperature broadband transmission divided by a reference spectrum at 2 T a) when **B** $\parallel$ [111], and b)–d) when **B** $\parallel$ $[1\bar{1}0]$. Even though all measurements were carried out below the ordering temperature, no resonance is observable in the 0–50 GHz–0–8 T parameter range.

6.2.3 Summary

The preceding elastic and inelastic neutron scattering experiments combined with Monte Carlo simulations reported a multi-**q** state in $MnSc_2S_4$. This possible realization of a fractional antiferromagnetic skyrmion lattice is not only an intriguing concept, but can serve with valuable information for the application aspects of antiferromagnetic topological objects. Motivated by these findings, I searched for the magnetic excitations of the ordered phases, the emphasis being on the antiferromagnetic skyrmions. The observed lack of additional spin resonances may be underwhelming, but it also serves useful information regarding the spin parameters.

Chapter 7

Summary

During my Ph.D., I studied three antiferromagnets, $BiFeO_3$, $MnSc_2S_4$, and $LiCoPO_4$. They either have nontrivial magnetic orderings, such as $MnSc_2S_4$, or are magnetoelectric, like $LiCoPO_4$, or both, as is the case for multiferroic $BiFeO_3$. They all host phenomena that are interesting either because of the technological promises or show novel effects on a fundamental level. The ME effect present both in $BiFeO_3$ and $LiCoPO_4$ makes them a playground for research on the spintronics application of this effect, as magnetic domains can be switched purely with electric fields with no current flow [27], as demonstrated in Refs. [133, 169, 170]. $BiFeO_3$ has the unique advantage that it is multiferroic and magnetoelectric even at room temperature. Experiments on $BiFeO_3$ in the past decade revealed a new phase, that has exceptionally large magnetoelectric constant $\chi_{YY}^{me}/c = 210\,\mathrm{ps/m}$, which is highly desirable for applications, since the higher the magnetoelectric coupling constant, the larger the electric field induced magnetization in the material.

Neutron scattering measurements combined with Monte Carlo simulations indicated the formation of antiferromagnetic skyrmions in $MnSc_2S_4$ at mK temperatures [194, 195]. Insensitive to stray fields, and topologically protected, antiferromagnetic skyrmions have the potential to be information carriers in spintronic devices [225, 226]. Very recent thermal Hall effect measurements in $MnSc_2S_4$ [209] also revealed anomalies in κ_{xx} at the magnetic phase transitions, implying that magnon heat transport is sensitive for such topological objects.

I summarize my results achieved related to the above materials in the following thesis points:

T1 Using THz absorption spectroscopy, I investigated the spin-wave excitations of a recently revealed high-temperature magnetic-field-induced transverse conical phase in $BiFeO_3$. I measured the magnetic field dependence of the mode frequencies in the cycloidal, conical and canted antiferromagnetic phases and also partially deduced the selection rules for the modes.

I analyzed and compared the magnetic field dependence of the resonance energies with the results of spin dynamics simulation developed by theoretician colleagues (L. Rózsa, L. Udvardi and L. Szunyogh). I also observed non-reciprocal light absorption for modes in the transverse conical phase, estimated their contributions to the static linear magnetoelectric effect and concluded that they contribute little to the large DC response [P2].

T2 I studied the field-dependent magnetic resonances of $MnSc_2S_4$ in its low-temperature, magnetically modulated phase with THz and microwave spectroscopy. With broadband microwave spectroscopy up to 50 GHz, I observed no resonances, while magnetic-field-dependent THz absorption spectra revealed one single resonance shifting linearly with the field. From the field dependence I determined the g-factor to be $g = 1.96 \pm 0.02$. Combining these two results I concluded that the anisotropy in $MnSc_2S_4$ is small and I propose that the anisotropy gap may open between 50 GHz, the upper limit of microwave spectroscopy measurements, and 100 GHz, the lower limit of THz absorption spectroscopy measurements [P3].

T3 In the magnetoelectric collinear antiferromagnet $LiCoPO_4$, I measured the absorption spectra of the two antiferromagnetic domains in the visible and near-infrared spectral ranges. To select a domain, I implemented the so-called magnetoelectric poling. I found an absorption difference as large as $\Delta\alpha/\alpha_0 = 34\%$ for the AFM domains of $LiCoPO_4$ at 1597 nm, and it is large even at the telecommunication wavelength 1550 nm. This absorption contrast is the manifestation of the non-reciprocal directional dichroism as time-reversal transforms one domain to another. I attributed the observed resonances to excitations between the electronic states of Co^{2+} ions split by the local crystal fields [P1].

T4 I built a simple, low temperature transmission scanning microscopy setup with which I observed the AFM domains of $LiCoPO_4$ formed upon zero-field cooling through the magnetic ordering temperature (T_N). The spotsize of the laser beam close to the diffraction limit determined the spatial resolution to 4 μm. I identified the contrast mechanism to be the non-reciprocal absorption of the domains. I determined the characteristic domain size in the sample to be on the scale of a few tens of μm. I achieved partial domain stabilization by cooling the sample through T_N only in magnetic fields [P1].

List of Publications

[P1] B. Tóth, V. Kocsis, Y. Tokunaga, Y. Taguchi, Y. Tokura, and S. Bordács, “Imaging antiferromagnetic domains in $LiCoPO_4$ via the optical magnetoelectric effect,” *Phys. Rev. B*, vol. 110, p. L100405, Sep 2024. [Online]. Available: https://link.aps.org/doi/10.1103/PhysRevB.110.L100405

[P2] B. Tóth, D. G. Farkas, K. Amelin, T. Rõõm, U. Nagel, L. Udvardi, L. Szunyogh, L. Rózsa, T. Ito, and S. Bordács, “Terahertz spin-wave excitations in the transverse conical phase of $BiFeO_3$,” *Phys. Rev. B*, vol. 109, p. 144424, Apr 2024. [Online]. Available: https://link.aps.org/doi/10.1103/PhysRevB.109.144424

[P3] B. Tóth, K. Amelin, T. Rõõm, U. Nagel, A. Bauernfeind, V. Tsurkan, L. Prodan, H.-A. Krug von Nidda, M. Scheffler, I. Kézsmárki, and S. Bordács, “Broadband magnetic resonance spectroscopy in $MnSc_2S_4$,” *Scientific Reports*, vol. 13, no. 1, p. 11069, Jul 2023. [Online]. Available: https://doi.org/10.1038/s41598-023-37911-6

Other publications not included in the thesis points

1. B. Molnár, G. Tolnai, B. Tóth, D. Légrády, A. Horváth "Guardyan – a novel GPU–based Monte Carlo code for simulating reactor transients (in Hungarian)" *Nukleon* XII., 1, 218, 2019. Available: https://nuklearis.hu/sites/default/files/nukleon/12_2_218_Molnar_3.pdf
2. M. Winkler, K. Geirhos, T. Tyborowski, B. Tóth, D. G. Farkas, J. S. White, T. Ito, S. Krohns, P. Lukenheimer, S. Bordács, and I. Kézsmárki "Anisotropic magnetocapacitance of antiferromagnetic cycloids in $BiFeO_3$" *Applied Physics Letters* vol. 125, no. 25, p. 252902, 2024. Available: https://doi.org/10.1063/5.0237659

Bibliography

[1] G. E. Moore, “Cramming more components onto integrated circuits,” *Proc. IEEE Inst. Electr. Electron. Eng.*, vol. 86, no. 1, pp. 82–85, Jan. 1998.

[2] K. J. Kuhn, “Considerations for ultimate CMOS scaling,” *IEEE Trans. Electron Devices*, vol. 59, no. 7, pp. 1813–1828, Jul. 2012.

[3] R. H. Dennard, F. H. Gaensslen, H.-N. Yu, V. L. Rideout, E. Bassous, and A. R. LeBlanc, “Design of ion-implanted MOSFET’s with very small physical dimensions,” *IEEE J. Solid-State Circuits*, vol. 9, no. 5, pp. 256–268, Oct. 1974.

[4] I. Ferain, C. A. Colinge, and J.-P. Colinge, “Multigate transistors as the future of classical metal-oxide-semiconductor field-effect transistors,” *Nature*, vol. 479, no. 7373, pp. 310–316, Nov. 2011.

[5] M. Schumacher, P. K. Baumann, and T. Seidel, “AVD and ALD as two complementary technology solutions for next generation dielectric and conductive thin-film processing,” *Chem. Vap. Depos.*, vol. 12, no. 2-3, pp. 99–108, Mar. 2006.

[6] P. E. Ross, “Why CPU frequency stalled,” *IEEE Spectrum*, vol. 45, no. 4, pp. 72–72, 2008.

[7] G. A. Stewart, W. Lampl, and for the ATLAS Collaboration, “How to review 4 million lines of ATLAS code,” *Journal of Physics: Conference Series*, vol. 898, no. 7, p. 072013, oct 2017. [Online]. Available: https://dx.doi.org/10.1088/1742-6596/898/7/072013

[8] M. Horowitz, “1.1 Computing’s energy problem (and what we can do about it),” in *2014 IEEE International Solid-State Circuits Conference Digest of Technical Papers (ISSCC)*. IEEE, Feb. 2014.

[9] S. A. Wolf, D. D. Awschalom, R. A. Buhrman, J. M. Daughton, S. von Molnár, M. L. Roukes, A. Y. Chtchelkanova, and D. M. Treger, “Spintronics:

a spin-based electronics vision for the future," *Science*, vol. 294, no. 5546, pp. 1488–1495, Nov. 2001.

[10] A. D. Kent and D. C. Worledge, "A new spin on magnetic memories," *Nature Nanotechnology*, vol. 10, no. 3, pp. 187–191, Mar 2015. [Online]. Available: https://doi.org/10.1038/nnano.2015.24

[11] A. V. Chumak, V. I. Vasyuchka, A. A. Serga, and B. Hillebrands, "Magnon spintronics," *Nature Physics*, vol. 11, no. 6, pp. 453–461, Jun 2015. [Online]. Available: https://doi.org/10.1038/nphys3347

[12] T. Jungwirth, X. Marti, P. Wadley, and J. Wunderlich, "Antiferromagnetic spintronics," *Nature Nanotechnology*, vol. 11, no. 3, pp. 231–241, Mar 2016. [Online]. Available: https://doi.org/10.1038/nnano.2016.18

[13] P. Wadley, B. Howells, J. Železný, C. Andrews, V. Hills, R. P. Campion, V. Novák, K. Olejník, F. Maccherozzi, S. S. Dhesi, S. Y. Martin, T. Wagner, J. Wunderlich, F. Freimuth, Y. Mokrousov, J. Kuneš, J. S. Chauhan, M. J. Grzybowski, A. W. Rushforth, K. W. Edmonds, B. L. Gallagher, and T. Jungwirth, "Electrical switching of an antiferromagnet," *Science*, vol. 351, no. 6273, pp. 587–590, 2016. [Online]. Available: https://www.science.org/doi/abs/10.1126/science.aab1031

[14] A. B. Shick, S. Khmelevskyi, O. N. Mryasov, J. Wunderlich, and T. Jungwirth, "Spin-orbit coupling induced anisotropy effects in bimetallic antiferromagnets: A route towards antiferromagnetic spintronics," *Phys. Rev. B*, vol. 81, p. 212409, Jun 2010. [Online]. Available: https://link.aps.org/doi/10.1103/PhysRevB.81.212409

[15] A. H. MacDonald and M. Tsoi, "Antiferromagnetic metal spintronics," *Philos. Trans. A Math. Phys. Eng. Sci.*, vol. 369, no. 1948, pp. 3098–3114, Aug. 2011.

[16] E. V. Gomonay and V. M. Loktev, "Spintronics of antiferromagnetic systems (review article)," *Low Temp. Phys.*, vol. 40, no. 1, pp. 17–35, Jan. 2014.

[17] O. Gomonay, T. Jungwirth, and J. Sinova, "Concepts of antiferromagnetic spintronics," *Phys. Status Solidi Rapid Res. Lett.*, vol. 11, no. 4, p. 1700022, Apr. 2017.

[18] V. Baltz, A. Manchon, M. Tsoi, T. Moriyama, T. Ono, and Y. Tserkovnyak, "Antiferromagnetic spintronics," *Rev. Mod. Phys.*, vol. 90, p. 015005, Feb 2018. [Online]. Available: https://link.aps.org/doi/10.1103/RevModPhys.90.015005

[19] C. Marrows, “APPLIED PHYSICS. Addressing an antiferromagnetic memory,” *Science*, vol. 351, no. 6273, pp. 558–559, Feb. 2016.

[20] X. Li, D. Kim, Y. Liu, and J. Kono, “Terahertz spin dynamics in rare-earth orthoferrites,” *Photonics Insights*, vol. 1, no. 11, p. R05, 2 2022. [Online]. Available: https://www.researching.cn/articles/OJ71e394d50dce845a

[21] N. A. Hill, “Why are there so few magnetic ferroelectrics?” *The Journal of Physical Chemistry B*, vol. 104, no. 29, pp. 6694–6709, Jun. 2000. [Online]. Available: https://doi.org/10.1021/jp000114x

[22] P. Curie, “Sur la symétrie dans les phénomènes physiques, symétrie d’un champ électrique et d’un champ magnétique,” *Journal de Physique Théorique et Appliquée*, vol. 3, no. 1, pp. 393–415, 1894. [Online]. Available: http://www.edpsciences.org/10.1051/jphystap:018940030039300

[23] L. D. Landau and E. M. Lifshitz, *Electrodynamics of Continuous Media*. New York: Pergamon Press, 1960.

[24] D. Astrov, “Magnetoelectric effect in chromium oxide,” *Sov. Phys. JETP*, vol. 13, no. 4, pp. 729–733, 1961. [Online]. Available: http://jetp.ras.ru/cgi-bin/dn/e_013_04_0729.pdf

[25] T. Kimura, T. Goto, H. Shintani, K. Ishizaka, T. Arima, and Y. Tokura, “Magnetic control of ferroelectric polarization,” *Nature*, vol. 426, no. 6962, pp. 55–58, 2003.

[26] M. Fiebig, “Revival of the magnetoelectric effect,” *Journal of Physics D: Applied Physics*, vol. 38, no. 8, p. R123, apr 2005. [Online]. Available: https://dx.doi.org/10.1088/0022-3727/38/8/R01

[27] S. Manipatruni, D. E. Nikonov, C.-C. Lin, T. A. Gosavi, H. Liu, B. Prasad, Y.-L. Huang, E. Bonturim, R. Ramesh, and I. A. Young, “Scalable energy-efficient magnetoelectric spin–orbit logic,” *Nature*, vol. 565, no. 7737, pp. 35–42, Jan 2019. [Online]. Available: https://doi.org/10.1038/s41586-018-0770-2

[28] M. Ghidini, R. Pellicelli, J. L. Prieto, X. Moya, J. Soussi, J. Briscoe, S. Dunn, and N. D. Mathur, “Non-volatile electrically-driven repeatable magnetization reversal with no applied magnetic field,” *Nature Communications*, vol. 4, no. 1, p. 1453, Feb 2013. [Online]. Available: https://doi.org/10.1038/ncomms2398

[29] I. Kézsmárki, U. Nagel, S. Bordács, R. S. Fishman, J. H. Lee, H. T. Yi, S.-W. Cheong, and T. Rõõm, “Optical diode effect at spin-wave excitations of the room-temperature multiferroic $BiFeO_3$,”

Phys. Rev. Lett., vol. 115, p. 127203, Sep 2015. [Online]. Available: https://link.aps.org/doi/10.1103/PhysRevLett.115.127203

[30] L. Néel, “Influence des fluctuations du champ moléculaire sur les propriétés magnétiques des corps,” *Ann. Phys. (Paris)*, vol. 10, no. 18, pp. 5–105, 1932.

[31] ——, “Magnetism and the local molecular field,” in *Nobel Lectures Physics 1963-1970*, Elsevier, Ed., Dec. 1972. [Online]. Available: https://hal.science/hal-02888357

[32] S.-W. Cheong, M. Fiebig, W. Wu, L. Chapon, and V. Kiryukhin, “Seeing is believing: visualization of antiferromagnetic domains,” *npj Quantum Materials*, vol. 5, no. 1, p. 3, Jan 2020. [Online]. Available: https://doi.org/10.1038/s41535-019-0204-x

[33] J. Goldstone, A. Salam, and S. Weinberg, “Broken symmetries,” *Phys. Rev.*, vol. 127, pp. 965–970, Aug 1962. [Online]. Available: https://link.aps.org/doi/10.1103/PhysRev.127.965

[34] P. Fazekas, *Lecture Notes on Electron Correlation and Magnetism*, ser. Series in Modern Condensed Mat. World Scientific, 1999, ch. 2.

[35] J. Solyom, *Fundamentals of the physics of solids*, 2007th ed. Berlin, Germany: Springer, Oct. 2007, ch. 14.

[36] J. Goodenough, *Magnetism and the Chemical Bond*, ser. Inorganic Chemistry Section / Interscience monographs on chemistry. Wiley, 1963.

[37] P. Anderson, “2 - Exchange in insulators: Superexchange, direct exchange, and double exchange,” in *Magnetism*, G. T. Rado and H. Suhl, Eds. Academic Press, 1963, pp. 25–83. [Online]. Available: https://www.sciencedirect.com/science/article/pii/B9780125753012500092

[38] M. A. Ruderman and C. Kittel, “Indirect exchange coupling of nuclear magnetic moments by conduction electrons,” *Phys. Rev.*, vol. 96, pp. 99–102, Oct 1954. [Online]. Available: https://link.aps.org/doi/10.1103/PhysRev.96.99

[39] T. Kasuya, “A theory of metallic ferro- and antiferromagnetism on Zener’s model,” *Progress of Theoretical Physics*, vol. 16, no. 1, pp. 45–57, 07 1956. [Online]. Available: https://doi.org/10.1143/PTP.16.45

[40] K. Yosida, “Magnetic properties of Cu-Mn alloys,” *Phys. Rev.*, vol. 106, pp. 893–898, Jun 1957. [Online]. Available: https://link.aps.org/doi/10.1103/PhysRev.106.893

[41] I. Dzyaloshinsky, “A thermodynamic theory of “weak” ferromagnetism of antiferromagnetics,” *Journal of Physics and Chemistry of Solids*, vol. 4, no. 4, pp. 241–255, 1958. [Online]. Available: https://www.sciencedirect.com/science/article/pii/0022369758900763

[42] T. Moriya, “New mechanism of anisotropic superexchange interaction,” *Phys. Rev. Lett.*, vol. 4, pp. 228–230, Mar 1960. [Online]. Available: https://link.aps.org/doi/10.1103/PhysRevLett.4.228

[43] ——, “Anisotropic superexchange interaction and weak ferromagnetism,” *Phys. Rev.*, vol. 120, pp. 91–98, Oct 1960. [Online]. Available: https://link.aps.org/doi/10.1103/PhysRev.120.91

[44] K. Aizu, “Possible species of ferromagnetic, ferroelectric, and ferroelastic crystals,” *Phys. Rev.*, vol. 2, no. 3, pp. 754–772, Aug. 1970.

[45] H. Schmid, “Multi-ferroic magnetoelectrics,” *Ferroelectrics*, vol. 162, no. 1, pp. 317–338, Jan. 1994. [Online]. Available: https://doi.org/10.1080/00150199408245120

[46] N. A. Spaldin, M. Fiebig, and M. Mostovoy, “The toroidal moment in condensed-matter physics and its relation to the magnetoelectric effect,” *J. Phys. Condens. Matter*, vol. 20, no. 43, p. 434203, Oct. 2008.

[47] T. Hayashida, K. Arakawa, T. Oshima, K. Kimura, and T. Kimura, “Observation of antiferromagnetic domains in Cr_2O_3 using nonreciprocal optical effects,” *Phys. Rev. Res.*, vol. 4, p. 043063, Oct 2022. [Online]. Available: https://link.aps.org/doi/10.1103/PhysRevResearch.4.043063

[48] V. Kocsis, K. Penc, T. Rõõm, U. Nagel, J. Vít, J. Romhányi, Y. Tokunaga, Y. Taguchi, Y. Tokura, I. Kézsmárki, and S. Bordács, “Identification of antiferromagnetic domains via the optical magnetoelectric effect,” *Phys. Rev. Lett.*, vol. 121, p. 057601, Aug 2018. [Online]. Available: https://link.aps.org/doi/10.1103/PhysRevLett.121.057601

[49] G. T. Rado and J. M. Ferrari, “Electric field dependence of the magnetic anisotropy energy in magnetite (Fe_3O_4),” *Phys. Rev. B*, vol. 12, pp. 5166–5174, Dec 1975. [Online]. Available: https://link.aps.org/doi/10.1103/PhysRevB.12.5166

[50] M. Alexe, M. Ziese, D. Hesse, P. Esquinazi, K. Yamauchi, T. Fukushima, S. Picozzi, and U. Gösele, “Ferroelectric switching in multiferroic magnetite (Fe_3O_4) thin films,” *Adv. Mater.*, vol. 21, no. 44, pp. 4452–4455, Nov. 2009.

[51] W. Eerenstein, N. D. Mathur, and J. F. Scott, “Multiferroic and magnetoelectric materials,” *Nature*, vol. 442, no. 7104, pp. 759–765, Aug. 2006.

[52] D. Khomskii, “Classifying multiferroics: Mechanisms and effects,” *Physics (College Park Md.)*, vol. 2, no. 20, Mar. 2009.

[53] Y. J. Choi, H. T. Yi, S. Lee, Q. Huang, V. Kiryukhin, and S.-W. Cheong, “Ferroelectricity in an Ising chain magnet,” *Phys. Rev. Lett.*, vol. 100, p. 047601, Jan 2008. [Online]. Available: https://link.aps.org/doi/10.1103/PhysRevLett.100.047601

[54] Y. Tokura, S. Seki, and N. Nagaosa, “Multiferroics of spin origin,” *Reports on Progress in Physics*, vol. 77, no. 7, p. 076501, jul 2014. [Online]. Available: https://dx.doi.org/10.1088/0034-4885/77/7/076501

[55] M. Fiebig, T. Lottermoser, D. Meier, and M. Trassin, “The evolution of multiferroics,” *Nat. Rev. Mater.*, vol. 1, no. 8, Aug. 2016.

[56] B. B. Van Aken, T. T. Palstra, A. Filippetti, and N. A. Spaldin, “The origin of ferroelectricity in magnetoelectric $YMnO_3$,” *Nature Materials*, vol. 3, no. 3, pp. 164–170, Mar 2004. [Online]. Available: https://doi.org/10.1038/nmat1080

[57] C. J. Fennie and K. M. Rabe, “Ferroelectric transition in $YMnO_3$ from first principles,” *Phys. Rev. B*, vol. 72, p. 100103, Sep 2005. [Online]. Available: https://link.aps.org/doi/10.1103/PhysRevB.72.100103

[58] N. Ikeda, H. Ohsumi, K. Ohwada, K. Ishii, T. Inami, K. Kakurai, Y. Murakami, K. Yoshii, S. Mori, Y. Horibe, and H. Kitô, “Ferroelectricity from iron valence ordering in the charge-frustrated system $LuFe_2O_4$,” *Nature*, vol. 436, no. 7054, pp. 1136–1138, Aug. 2005.

[59] N. Hur, S. Park, P. A. Sharma, J. S. Ahn, S. Guha, and S.-W. Cheong, “Electric polarization reversal and memory in a multiferroic material induced by magnetic fields,” *Nature*, vol. 429, no. 6990, pp. 392–395, May 2004. [Online]. Available: https://doi.org/10.1038/nature02572

[60] W. C. Röntgen, “Ueber die durch bewegung eines im homogenen electrischen felde befindlichen dielectricums hervorgerufene electrodynamische kraft,” *Ann. Phys.*, vol. 271, no. 10, pp. 264–270, Jan. 1888.

[61] H. A. Wilson, “III. On the electric effect of rotating a dielectric in a magnetic field,” *Philos. Trans. R. Soc. Lond.*, vol. 204, no. 372-386, pp. 121–137, Jan. 1905.

[62] D. Astrov, “The magnetoelectric effect in antiferromagnetics,” *Sov. Phys. JETP*, vol. 38, pp. 984–985, 1960. [Online]. Available: http://jetp.ras.ru/cgi-bin/dn/e_011_03_0708.pdf

[63] I. E. Dzyaloshinskiĭ, “On the magneto-electrical effects in antiferromagnets,” *Soviet physics, JETP*, vol. 10, pp. 628–629, 1960. [Online]. Available: https://api.semanticscholar.org/CorpusID:204303962

[64] T. Arima, “Magneto-electric optics in non-centrosymmetric ferromagnets,” *J. Phys. Condens. Matter*, vol. 20, no. 43, p. 434211, Oct. 2008.

[65] I. Kézsmárki, N. Kida, H. Murakawa, S. Bordács, Y. Onose, and Y. Tokura, “Enhanced directional dichroism of terahertz light in resonance with magnetic excitations of the multiferroic Ba_2CoGeO_7 oxide compound,” *Phys. Rev. Lett.*, vol. 106, p. 057403, Feb 2011. [Online]. Available: https://link.aps.org/doi/10.1103/PhysRevLett.106.057403

[66] S. Bordács, I. Kézsmárki, D. Szaller, L. Demkó, N. Kida, H. Murakawa, Y. Onose, R. Shimano, T. Rõõm, U. Nagel, S. Miyahara, N. Furukawa, and Y. Tokura, “Chirality of matter shows up via spin excitations,” *Nature Physics*, vol. 8, no. 10, pp. 734–738, Oct 2012. [Online]. Available: https://doi.org/10.1038/nphys2387

[67] D. Szaller, S. Bordács, and I. Kézsmárki, “Symmetry conditions for nonreciprocal light propagation in magnetic crystals,” *Phys. Rev. B*, vol. 87, p. 014421, Jan 2013. [Online]. Available: https://link.aps.org/doi/10.1103/PhysRevB.87.014421

[68] I. Kézsmárki, D. Szaller, S. Bordács, V. Kocsis, Y. Tokunaga, Y. Taguchi, H. Murakawa, Y. Tokura, H. Engelkamp, T. Rõõm, and U. Nagel, “One-way transparency of four-coloured spin-wave excitations in multiferroic materials,” *Nature Communications*, vol. 5, no. 1, p. 3203, Feb 2014. [Online]. Available: https://doi.org/10.1038/ncomms4203

[69] A. Cano, “Theory of electromagnon resonances in the optical response of spiral magnets,” *Phys. Rev. B*, vol. 80, p. 180416, Nov 2009. [Online]. Available: https://link.aps.org/doi/10.1103/PhysRevB.80.180416

[70] S. Miyahara and N. Furukawa, “Theory of magnetoelectric resonance in two-dimensional S = 3/2 antiferromagnet $Ba_2CoGe_2O_7$ via spin-dependent metal-ligand hybridization mechanism,” *Journal of the Physical Society of Japan*, vol. 80, no. 7, p. 073708, 2011. [Online]. Available: https://doi.org/10.1143/JPSJ.80.073708

[71] ——, “Nonreciprocal directional dichroism and toroidalmagnons in helical magnets,” *Journal of the Physical Society of Japan*, vol. 81, no. 2, p. 023712, Feb 2012. [Online]. Available: https://doi.org/10.1143/JPSJ.81.023712

[72] D. Szaller, S. Bordács, V. Kocsis, T. Rõ om, U. Nagel, and I. Kézsmárki, “Effect of spin excitations with simultaneous magnetic- and electric-dipole character on the static magnetoelectric properties of multiferroic materials,” *Phys. Rev. B*, vol. 89, p. 184419, May 2014. [Online]. Available: https://link.aps.org/doi/10.1103/PhysRevB.89.184419

[73] R. M. Hornreich and S. Shtrikman, “Theory of gyrotropic birefringence,” *Phys. Rev.*, vol. 171, pp. 1065–1074, Jul 1968. [Online]. Available: https://link.aps.org/doi/10.1103/PhysRev.171.1065

[74] S. Iguchi, R. Masuda, S. Seki, Y. Tokura, and Y. Takahashi, “Enhanced gyrotropic birefringence and natural optical activity on electromagnon resonance in a helimagnet,” *Nature Communications*, vol. 12, no. 1, p. 6674, Nov 2021. [Online]. Available: https://doi.org/10.1038/s41467-021-26953-x

[75] T. Roth and G. L. J. A. Rikken, “Observation of magnetoelectric Jones birefringence,” *Phys. Rev. Lett.*, vol. 85, pp. 4478–4481, Nov 2000. [Online]. Available: https://link.aps.org/doi/10.1103/PhysRevLett.85.4478

[76] P. T. Mahon and J. E. Sipe, “From magnetoelectric response to optical activity,” *Phys. Rev. Res.*, vol. 2, p. 043110, Oct 2020. [Online]. Available: https://link.aps.org/doi/10.1103/PhysRevResearch.2.043110

[77] *MCS260 Cornerstone 260 Monochromators*, Newport Corporation, Irvine, CA, 2015, available at https://www.newport.com/medias/sys_master/images/images/hae/h47/8797226926110/Oriel-Cornerstone-260-User-Manual-RevA.pdf.

[78] P. B. Fellgett, “On the ultimate sensitivity and practical performance of radiation detectors,” *J. Opt. Soc. Am.*, vol. 39, no. 11, pp. 970–976, Nov 1949. [Online]. Available: https://opg.optica.org/abstract.cfm?URI=josa-39-11-970

[79] L. Peedu, “Spin-waves in magnetoelectric materials with strong single-ion anisotropy,” Ph.D. dissertation, Tallinn University of Technology, Tallinn, Estonia, 2022.

[80] C. C. Homes, G. L. Carr, R. P. S. M. Lobo, J. D. Laveigne, and D. B. Tanner, “Silicon beam splitter for far-infrared and terahertz spectroscopy,” *Appl. Opt.*, vol. 46, no. 32, pp. 7884–7888, Nov. 2007.

[81] P. A. R. Ade, A. E. Costley, C. T. Cunningham, C. L. Mok, G. F. Neill, and T. J. Parker, "Free-standing grids wound from 5 μm diameter wire for spectroscopy at far-infrared wavelengths," *Infrared Phys.*, vol. 19, no. 5, pp. 599–601, Oct. 1979.

[82] D. Martin and E. Puplett, "Polarised interferometric spectrometry for the millimetre and submillimetre spectrum," *Infrared Physics*, vol. 10, no. 2, pp. 105–109, 1970. [Online]. Available: https://www.sciencedirect.com/science/article/pii/0020089170900060

[83] C. Kittel, "On the theory of ferromagnetic resonance absorption," *Phys. Rev.*, vol. 73, pp. 155–161, Jan 1948. [Online]. Available: https://link.aps.org/doi/10.1103/PhysRev.73.155

[84] K. Gupta, R. Garg, I. Bahl, and P. Bhartia, *Microstrip Lines and Slotlines*, 2nd ed., ser. Artech House microwave library. Boston: Artech House, 1996.

[85] C. Wen, "Coplanar waveguide: A surface strip transmission line suitable for nonreciprocal gyromagnetic device applications," *IEEE Transactions on Microwave Theory and Techniques*, vol. 17, no. 12, pp. 1087–1090, 1969.

[86] D. M. Pozar, *Microwave engineering; 3rd ed.* Hoboken, NJ: Wiley, 2005, ch. 4.

[87] J. H. Poynting, "XV. On the transfer of energy in the electromagnetic field," *Philos. Trans. R. Soc. Lond.*, vol. 175, no. 0, pp. 343–361, Dec. 1884.

[88] D. M. Pozar, *Microwave engineering; 3rd ed.* Hoboken, NJ: Wiley, 2005, ch. 1.

[89] C. Bilzer, "Microwave susceptibility of thin ferromagnetic films:metrology and insight into magnetization dynamics," Ph.D. dissertation, Université Paris Sud, Paris, France, 2007.

[90] L. Landau and E. Lifshitz, "On the theory of the dispersion of magnetic permeability in ferromagnetic bodies," *Phys. Z. Sowjet*, vol. 8, pp. 153–69, 1935.

[91] T. L. Gilbert, "A lagrangian formulation of the gyromagnetic equation of the magnetization field," *Phys. Rev.*, vol. 100, p. 1243, 1955.

[92] C. Kittel and P. McEuen, *Introduction to Solid State Physics*. John Wiley & Sons, 2005, ch. 13. [Online]. Available: https://books.google.hu/books?id=rAMujwEACAAJ

[93] C. Kittel, “Theory of antiferromagnetic resonance,” *Phys. Rev.*, vol. 82, pp. 565–565, May 1951. [Online]. Available: https://link.aps.org/doi/10.1103/PhysRev.82.565

[94] F. Keffer and C. Kittel, “Theory of antiferromagnetic resonance,” *Phys. Rev.*, vol. 85, pp. 329–337, Jan 1952. [Online]. Available: https://link.aps.org/doi/10.1103/PhysRev.85.329

[95] E. A. Turov, *Compensated Collinear Antiferromagnetism.* New York, USA: Academic Press, 1965, ch. 4.

[96] G. L. Squires, *Introduction to the Theory of Thermal Neutron Scattering*, 3rd ed. Cambridge University Press, 2012, ch. 7.

[97] ——, *Introduction to the Theory of Thermal Neutron Scattering*, 3rd ed. Cambridge University Press, 2012, ch. 1.

[98] Á. Butykai, “Néel-type skyrmions in multiferroic lacunar spinels,” Ph.D. dissertation, Budapest University of Technology and Economincs, Budapest, Hungary, 2018.

[99] C. G. Shull, “Nobel Lecture,” www.NobelPrize.org, Nobel Foundation, Dec. 1994.

[100] M. Fiebig, D. Fröhlich, G. Sluyterman v. L., and R. V. Pisarev, “Domain topography of antiferromagnetic Cr_2O_3 by second-harmonic generation,” *Applied Physics Letters*, vol. 66, no. 21, pp. 2906–2908, 05 1995. [Online]. Available: https://doi.org/10.1063/1.113699

[101] B. B. Van Aken, J.-P. Rivera, H. Schmid, and M. Fiebig, “Observation of ferrotoroidic domains,” *Nature*, vol. 449, no. 7163, pp. 702–705, Oct 2007. [Online]. Available: https://doi.org/10.1038/nature06139

[102] A. S. Zimmermann, B. B. Van Aken, H. Schmid, J.-P. Rivera, J. Li, D. Vaknin, and M. Fiebig, “Anisotropy of antiferromagnetic 180° domains in magnetoelectric $LiMPO_4$ (M = Fe, Co, Ni),” *The European Physical Journal B*, vol. 71, no. 3, pp. 355–360, Oct 2009. [Online]. Available: https://doi.org/10.1140/epjb/e2009-00223-3

[103] S. Heinze, M. Bode, A. Kubetzka, O. Pietzsch, X. Nie, S. Blügel, and R. Wiesendanger, “Real-space imaging of two-dimensional antiferromagnetism on the atomic scale,” *Science*, vol. 288, no. 5472, pp. 1805–1808, 2000. [Online]. Available: https://www.science.org/doi/abs/10.1126/science.288.5472.1805

[104] A. Kubetzka, P. Ferriani, M. Bode, S. Heinze, G. Bihlmayer, K. von Bergmann, O. Pietzsch, S. Blügel, and R. Wiesendanger, "Revealing antiferromagnetic order of the Fe monolayer on W(001): Spin-polarized scanning tunneling microscopy and first-principles calculations," *Phys. Rev. Lett.*, vol. 94, p. 087204, Mar 2005. [Online]. Available: https://link.aps.org/doi/10.1103/PhysRevLett.94.087204

[105] M. Bode, E. Y. Vedmedenko, K. von Bergmann, A. Kubetzka, P. Ferriani, S. Heinze, and R. Wiesendanger, "Atomic spin structure of antiferromagnetic domain walls," *Nature Materials*, vol. 5, no. 6, pp. 477–481, Jun 2006. [Online]. Available: https://doi.org/10.1038/nmat1646

[106] J.-Y. Chauleau, T. Chirac, S. Fusil, V. Garcia, W. Akhtar, J. Tranchida, P. Thibaudeau, I. Gross, C. Blouzon, A. Finco, M. Bibes, B. Dkhil, D. D. Khalyavin, P. Manuel, V. Jacques, N. Jaouen, and M. Viret, "Electric and antiferromagnetic chiral textures at multiferroic domain walls," *Nat. Mater.*, vol. 19, no. 4, pp. 386–390, Apr. 2020.

[107] P. M. Sass, W. Ge, J. Yan, D. Obeysekera, J. J. Yang, and W. Wu, "Magnetic imaging of domain walls in the antiferromagnetic topological insulator $MnBi_2Te_4$," *Nano Letters*, vol. 20, no. 4, pp. 2609–2614, Apr 2020. [Online]. Available: https://doi.org/10.1021/acs.nanolett.0c00114

[108] R. D. Johnson, P. Barone, A. Bombardi, R. J. Bean, S. Picozzi, P. G. Radaelli, Y. S. Oh, S.-W. Cheong, and L. C. Chapon, "X-ray imaging and multiferroic coupling of cycloidal magnetic domains in ferroelectric monodomain $BiFeO_3$," *Phys. Rev. Lett.*, vol. 110, p. 217206, May 2013. [Online]. Available: https://link.aps.org/doi/10.1103/PhysRevLett.110.217206

[109] F. P. Chmiel, N. Waterfield Price, R. D. Johnson, A. D. Lamirand, J. Schad, G. van der Laan, D. T. Harris, J. Irwin, M. S. Rzchowski, C.-B. Eom, and P. G. Radaelli, "Observation of magnetic vortex pairs at room temperature in a planar α-Fe_2O_3/Co heterostructure," *Nature Materials*, vol. 17, no. 7, pp. 581–585, Jul 2018. [Online]. Available: https://doi.org/10.1038/s41563-018-0101-x

[110] I. Gross, W. Akhtar, V. Garcia, L. J. Martínez, S. Chouaieb, K. Garcia, C. Carrétéro, A. Barthélémy, P. Appel, P. Maletinsky, J.-V. Kim, J. Y. Chauleau, N. Jaouen, M. Viret, M. Bibes, S. Fusil, and V. Jacques, "Real-space imaging of non-collinear antiferromagnetic order with a single-spin magnetometer," *Nature*, vol. 549, no. 7671, pp. 252–256, Sep 2017. [Online]. Available: https://doi.org/10.1038/nature23656

[111] S. Kollarics, F. Simon, A. Bojtor, K. Koltai, G. Klujber, M. Szieberth, B. Márkus, D. Beke, K. Kamarás, A. Gali, D. Amirari, R. Berry, S. Boucher, D. Gavryushkin, G. Jeschke, J. Cleveland, S. Takahashi, P. Szirmai, L. Forró, E. Emmanouilidou, R. Singh, and K. Holczer, "Ultrahigh nitrogen-vacancy center concentration in diamond," *Carbon*, vol. 188, pp. 393–400, 2022. [Online]. Available: https://www.sciencedirect.com/science/article/pii/S000862232101191X

[112] P. Grundy and R. Tebble, "Lorentz electron microscopy," *Advances in Physics*, vol. 17, no. 66, pp. 153–242, 1968. [Online]. Available: https://doi.org/10.1080/00018736800101286

[113] Y. Togawa, T. Koyama, K. Takayanagi, S. Mori, Y. Kousaka, J. Akimitsu, S. Nishihara, K. Inoue, A. S. Ovchinnikov, and J. Kishine, "Chiral magnetic soliton lattice on a chiral helimagnet," *Phys. Rev. Lett.*, vol. 108, p. 107202, Mar 2012. [Online]. Available: https://link.aps.org/doi/10.1103/PhysRevLett.108.107202

[114] P. Němec, M. Fiebig, T. Kampfrath, and A. V. Kimel, "Antiferromagnetic opto-spintronics," *Nature Physics*, vol. 14, no. 3, pp. 229–241, Mar 2018. [Online]. Available: https://doi.org/10.1038/s41567-018-0051-x

[115] A. F. Andreev and V. I. Marchenko, "Symmetry and the macroscopic dynamics of magnetic materials," *Soviet Physics Uspekhi*, vol. 23, no. 1, p. 21, jan 1980. [Online]. Available: https://dx.doi.org/10.1070/PU1980v023n01ABEH004859

[116] T. Kampfrath, A. Sell, G. Klatt, A. Pashkin, S. Mährlein, T. Dekorsy, M. Wolf, M. Fiebig, A. Leitenstorfer, and R. Huber, "Coherent terahertz control of antiferromagnetic spin waves," *Nature Photonics*, vol. 5, no. 1, pp. 31–34, Jan 2011. [Online]. Available: https://doi.org/10.1038/nphoton.2010.259

[117] C. Tzschaschel, K. Otani, R. Iida, T. Shimura, H. Ueda, S. Günther, M. Fiebig, and T. Satoh, "Ultrafast optical excitation of coherent magnons in antiferromagnetic NiO," *Phys. Rev. B*, vol. 95, p. 174407, May 2017. [Online]. Available: https://link.aps.org/doi/10.1103/PhysRevB.95.174407

[118] M. Fiebig, V. Pavlov, and R. Pisarev, "Second-harmonic generation as a tool for studying electronic and magnetic structures of crystals: review," *Journal of the Optical Society of America B*, vol. 22, pp. 96–118, 01 2005.

[119] V. J. Folen, G. T. Rado, and E. W. Stalder, "Anisotropy of the magnetoelectric effect in Cr_2O_3," *Phys. Rev. Lett.*, vol. 6, pp. 607–608, Jun 1961. [Online]. Available: https://link.aps.org/doi/10.1103/PhysRevLett.6.607

[120] G. T. Rado and V. J. Folen, “Observation of the magnetically induced magnetoelectric effect and evidence for antiferromagnetic domains,” *Phys. Rev. Lett.*, vol. 7, pp. 310–311, Oct 1961. [Online]. Available: https://link.aps.org/doi/10.1103/PhysRevLett.7.310

[121] K. Kimura, T. Katsuyoshi, Y. Sawada, S. Kimura, and T. Kimura, “Imaging switchable magnetoelectric quadrupole domains via nonreciprocal linear dichroism,” *Communications Materials*, vol. 1, no. 1, p. 39, Jul 2020. [Online]. Available: https://doi.org/10.1038/s43246-020-0040-3

[122] K. Amine, H. Yasuda, and M. Yamachi, “Olivine $LiCoPO_4$ as 4.8 V electrode material for lithium batteries,” *Electrochemical and Solid-State Letters*, vol. 3, no. 4, 2000. [Online]. Available: https://doi.org/10.1149/1.1390994

[123] M. Hu, X. Pang, and Z. Zhou, “Review recent progress in high-voltage lithium ion batteries,” 2013. [Online]. Available: https://doi.org/10.1016/j.jpowsour.2013.03.024

[124] X. Fan, L. Chen, O. Borodin, X. Ji, J. Chen, S. Hou, T. Deng, J. Zheng, C. Yang, S. C. Liou, K. Amine, K. Xu, and C. Wang, “Non-flammable electrolyte enables Li-metal batteries with aggressive cathode chemistries,” *Nature Nanotechnology*, vol. 13, no. 8, 2018. [Online]. Available: https://doi.org/10.1038/s41565-018-0183-2

[125] R. E. Newnham and M. J. Redman, “Crystallographic data for $LiMgPO_4$, $LiCoPO_4$, and $LiNiPO_4$,” *J. Am. Ceram. Soc.*, vol. 48, no. 10, pp. 547–547, Oct. 1965.

[126] R. Santoro, D. Segal, and R. Newnham, “Magnetic properties of $LiCoPO_4$ and $LiNiPO_4$,” *Journal of Physics and Chemistry of Solids*, vol. 27, no. 6, pp. 1192–1193, 1966. [Online]. Available: https://www.sciencedirect.com/science/article/pii/0022369766900977

[127] C. Ederer and N. A. Spaldin, “Towards a microscopic theory of toroidal moments in bulk periodic crystals,” *Phys. Rev. B*, vol. 76, p. 214404, Dec 2007. [Online]. Available: https://link.aps.org/doi/10.1103/PhysRevB.76.214404

[128] A. S. Zimmermann, D. Meier, and M. Fiebig, “Ferroic nature of magnetic toroidal order,” *Nature Communications*, vol. 5, no. 1, p. 4796, Sep 2014. [Online]. Available: https://doi.org/10.1038/ncomms5796

[129] V. Kocsis, S. Bordács, Y. Tokunaga, J. Viirok, L. Peedu, T. Rõõm, U. Nagel, Y. Taguchi, Y. Tokura, and I. Kézsmárki, “Magnetoelectric spectroscopy of

spin excitations in $LiCoPO_4$," *Phys. Rev. B*, vol. 100, p. 155124, Oct 2019. [Online]. Available: https://link.aps.org/doi/10.1103/PhysRevB.100.155124

[130] J.-P. Rivera, "The linear magnetoelectric effect in $LiCoPO_4$ revisited," *Ferroelectrics*, vol. 161, no. 1, pp. 147–164, 1994. [Online]. Available: https://doi.org/10.1080/00150199408213364

[131] D. Vaknin, J. L. Zarestky, L. L. Miller, J.-P. Rivera, and H. Schmid, "Weakly coupled antiferromagnetic planes in single-crystal $LiCoPO_4$," *Phys. Rev. B*, vol. 65, p. 224414, May 2002. [Online]. Available: https://link.aps.org/doi/10.1103/PhysRevB.65.224414

[132] M. Mercier, J. Gareyte, and E. F. Bertaut, "Une nouvelle famille de corps manétoelectriques: $LiMPO_4$ (M = Mn, Co, Ni)," *C. R. Acad. Sc. Paris*, vol. 264, p. 979, Mar. 1967. [Online]. Available: https://gallica.bnf.fr/ark:/12148/bpt6k6224817h/f269.item

[133] V. Kocsis, Y. Tokunaga, Y. Tokura, and Y. Taguchi, "Switching of antiferromagnetic states in $LiCoPO_4$ as investigated via the magnetoelectric effect," *Phys. Rev. B*, vol. 104, p. 054426, Aug 2021. [Online]. Available: https://link.aps.org/doi/10.1103/PhysRevB.104.054426

[134] R. Saint-Martin and S. Franger, "Growth of $LiCoPO_4$ single crystals using an optical floating-zone technique," *Journal of Crystal Growth*, vol. 310, no. 4, pp. 861–864, 2008. [Online]. Available: https://www.sciencedirect.com/science/article/pii/S0022024807011645

[135] J.-P. Rivera, "Optics of $LiCoPO_4$ single crystal," *Journal of the Korean Physical Society*, vol. 32, pp. 1839–1842, 02 1998.

[136] I. Kornev, J.-P. Rivera, S. Gentil, A. Jansen, M. Bichurin, H. Schmid, and P. Wyder, "Optical absorption of Co^{2+} in $LiCoPO_4$," *Physica B: Condensed Matter*, vol. 270, no. 1, pp. 82–87, 1999. [Online]. Available: https://www.sciencedirect.com/science/article/pii/S0921452699001581

[137] K. Kimura and T. Kimura, "Nonvolatile switching of large nonreciprocal optical absorption at shortwave infrared wavelengths," *Phys. Rev. Lett.*, vol. 132, p. 036901, Jan 2024. [Online]. Available: https://link.aps.org/doi/10.1103/PhysRevLett.132.036901

[138] J. H. Jung, M. Matsubara, T. Arima, J. P. He, Y. Kaneko, and Y. Tokura, "Optical magnetoelectric effect in the polar $GaFeO_3$ ferrimagnet," *Phys. Rev. Lett.*, vol. 93, p. 037403, Jul 2004. [Online]. Available: https://link.aps.org/doi/10.1103/PhysRevLett.93.037403

[139] L. Barron, *Molecular Light Scattering and Optical Activity*. Cambridge University Press, 2004. [Online]. Available: https://books.google.hu/books?id=KYfXjwEACAAJ

[140] M. Saito, K. Taniguchi, and T.-h. Arima, "Gigantic optical magnetoelectric effect in CuB_2O_4," *Journal of the Physical Society of Japan*, vol. 77, no. 1, p. 013705, Jan. 2008. [Online]. Available: http://dx.doi.org/10.1143/JPSJ.77.013705

[141] J.-P. Rivera and H. Schmid, "Search for the piezomagnetoelectric effect in $LiCoPO_4$," *Ferroelectrics*, vol. 161, no. 1, pp. 91–97, 1994. [Online]. Available: https://doi.org/10.1080/00150199408213357

[142] J.-G. Park, M. D. Le, J. Jeong, and S. Lee, "Structure and spin dynamics of multiferroic $BiFeO_3$," *Journal of Physics: Condensed Matter*, vol. 26, no. 43, p. 433202, Oct. 2014. [Online]. Available: https://doi.org/10.1088/0953-8984/26/43/433202

[143] S. Kawachi, A. Miyake, T. Ito, S. E. Dissanayake, M. Matsuda, W. Ratcliff, Z. Xu, Y. Zhao, S. Miyahara, N. Furukawa, and M. Tokunaga, "Successive field-induced transitions in $BiFeO_3$ around room temperature," *Phys. Rev. Materials*, vol. 1, p. 024408, Jul 2017. [Online]. Available: https://link.aps.org/doi/10.1103/PhysRevMaterials.1.024408

[144] R. Haumont, I. A. Kornev, S. Lisenkov, L. Bellaiche, J. Kreisel, and B. Dkhil, "Phase stability and structural temperature dependence in powdered multiferroic $BiFeO_3$," *Phys. Rev. B*, vol. 78, p. 134108, Oct 2008. [Online]. Available: https://link.aps.org/doi/10.1103/PhysRevB.78.134108

[145] D. C. Arnold, K. S. Knight, F. D. Morrison, and P. Lightfoot, "Ferroelectric-paraelectric transition in $BiFeO_3$: Crystal structure of the orthorhombic β phase," *Phys. Rev. Lett.*, vol. 102, p. 027602, Jan 2009. [Online]. Available: https://link.aps.org/doi/10.1103/PhysRevLett.102.027602

[146] J. Moreau, C. Michel, R. Gerson, and W. James, "Ferroelectric $BiFeO_3$ X-ray and neutron diffraction study," *Journal of Physics and Chemistry of Solids*, vol. 32, no. 6, pp. 1315–1320, 1971. [Online]. Available: https://www.sciencedirect.com/science/article/pii/S0022369771801890

[147] T. Ito, T. Ushiyama, Y. Yanagisawa, R. Kumai, and Y. Tomioka, "Growth of Highly Insulating Bulk Single Crystals of Multiferroic $BiFeO_3$ and Their Inherent Internal Strains in the Domain-Switching Process," *Crystal Growth & Design*, vol. 11, no. 11, pp. 5139–5143, nov 2011. [Online]. Available: https://pubs.acs.org/doi/10.1021/cg201068m

[148] S. V. Kiselev, R. P. Ozerov, and G. S. Zhdanov, “Detection of magnetic order in ferroelectric $BiFeO_3$ by neutron diffraction,” *Soviet Physics Doklady*, vol. 7, p. 742, 1963, *in Russian:* Detection of magnetic arrangement in the $BiFeO_3$ ferroelectric by means of neutron diffraction study, *Dokl. Akad. Nauk SSSR*, 1962, Vol. 145, no. 6, pp. 1255–1258.

[149] R. S. Fishman, “Pinning, rotation, and metastability of $BiFeO_3$ cycloidal domains in a magnetic field,” *Phys. Rev. B*, vol. 97, p. 014405, Jan 2018. [Online]. Available: https://link.aps.org/doi/10.1103/PhysRevB.97.014405

[150] J. Jeong, E. A. Goremychkin, T. Guidi, K. Nakajima, G. S. Jeon, S.-A. Kim, S. Furukawa, Y. B. Kim, S. Lee, V. Kiryukhin, S.-W. Cheong, and J.-G. Park, “Spin wave measurements over the full Brillouin zone of multiferroic $BiFeO_3$,” *Physical Review Letters*, vol. 108, no. 7, p. 077202, Feb 2012. [Online]. Available: https://doi.org/10.1103/physrevlett.108.077202

[151] M. Matsuda, R. S. Fishman, T. Hong, C. H. Lee, T. Ushiyama, Y. Yanagisawa, Y. Tomioka, and T. Ito, “Magnetic dispersion and anisotropy in multiferroic $BiFeO_3$,” *Physical Review Letters*, vol. 109, no. 6, p. 067205, Aug 2012. [Online]. Available: https://doi.org/10.1103/physrevlett.109.067205

[152] Z. Xu, J. Wen, T. Berlijn, P. M. Gehring, C. Stock, M. B. Stone, W. Ku, G. Gu, S. M. Shapiro, R. J. Birgeneau, and G. Xu, “Thermal evolution of the full three-dimensional magnetic excitations in the multiferroic $BiFeO_3$,” *Phys. Rev. B*, vol. 86, p. 174419, Nov 2012. [Online]. Available: http://link.aps.org/doi/10.1103/PhysRevB.86.174419

[153] I. Sosnowska and A. K. Zvezdin, “Origin of the long period magnetic ordering in $BiFeO_3$,” *J. Magn. Magn. Mater.*, vol. 140-144, pp. 167–168, Feb. 1995.

[154] M. Ramazanoglu, M. Laver, W. Ratcliff, S. M. Watson, W. C. Chen, A. Jackson, K. Kothapalli, S. Lee, S. W. Cheong, and V. Kiryukhin, “Local weak ferromagnetism in single-crystalline ferroelectric $BiFeO_3$,” *Physical Review Letters*, vol. 107, no. 20, p. 207206, 2011.

[155] J. Jeong, M. D. Le, P. Bourges, S. Petit, S. Furukawa, S.-A. Kim, S. Lee, S.-W. Cheong, and J.-G. Park, “Temperature-dependent interplay of Dzyaloshinskii-Moriya interaction and single-ion anisotropy in multiferroic $BiFeO_3$,” *Phys. Rev. Lett.*, vol. 113, p. 107202, Sep 2014. [Online]. Available: https://link.aps.org/doi/10.1103/PhysRevLett.113.107202

[156] D. Talbayev, S. A. Trugman, S. Lee, H. T. Yi, S.-W. Cheong, and A. J. Taylor, “Long-wavelength magnetic and magnetoelectric excitations in the ferroelectric

antiferromagnet $BiFeO_3$," *Phys. Rev. B*, vol. 83, p. 094403, Mar 2011. [Online]. Available: https://link.aps.org/doi/10.1103/PhysRevB.83.094403

[157] U. Nagel, R. S. Fishman, T. Katuwal, H. Engelkamp, D. Talbayev, H. T. Yi, S.-W. Cheong, and T. Rõõm, "Terahertz spectroscopy of spin waves in multiferroic $BiFeO_3$ in high magnetic fields," *Phys. Rev. Lett.*, vol. 110, p. 257201, Jun 2013. [Online]. Available: https://link.aps.org/doi/10.1103/PhysRevLett.110.257201

[158] K. Ohoyama, S. Lee, S. Yoshii, Y. Narumi, T. Morioka, H. Nojiri, G. Sang Jeon, S.-W. Cheong, and J.-G. Park, "High field neutron diffraction studies on metamagnetic transition of multiferroic $BiFeO_3$," *J. Phys. Soc. Jpn.*, vol. 80, no. 12, p. 125001, Dec. 2011.

[159] A. V. Zalesskii, A. K. Zvezdin, A. A. Frolov, and A. A. Bush, "^{57}Fe NMR study of a spatially modulated magnetic structure in $BiFeO_3$," *JETP Lett.*, vol. 71, no. 11, pp. 465–468, Jun. 2000.

[160] A. V. Zalesskii, A. A. Frolov, A. K. Zvezdin, A. A. Gippius, E. N. Morozova, D. F. Khozeevc, A. S. Bush, and V. S. Pokatilov, "Effect of spatial spin modulation on the relaxation and NMR frequencies of ^{57}Fe nuclei in a ferroelectric antiferromagnet $BiFeO_3$," *J. Exp. Theor. Phys.*, vol. 95, no. 1, pp. 101–105, Jul. 2002.

[161] I. Sosnowska, T. P. Neumaier, and E. Steichele, "Spiral magnetic ordering in bismuth ferrite," *Journal of Physics C: Solid State Physics*, vol. 15, no. 23, pp. 4835–4846, aug 1982. [Online]. Available: http://stacks.iop.org/0022-3719/15/i=23/a=020?key=crossref.7f3c354050e924e5f80e799192fea4ef

[162] B. Ruette, S. Zvyagin, A. P. Pyatakov, A. Bush, J. F. Li, V. I. Belotelov, A. K. Zvezdin, and D. Viehland, "Magnetic-field-induced phase transition in $BiFeO_3$ observed by high-field electron spin resonance: Cycloidal to homogeneous spin order," *Physical Review B*, vol. 69, no. 6, p. 064114, Feb. 2004. [Online]. Available: https://doi.org/10.1103/physrevb.69.064114

[163] Z. V. Gareeva, A. F. Popkov, S. V. Soloviov, and A. K. Zvezdin, "Field-induced phase transitions and phase diagrams in $BiFeO_3$-like multiferroics," *Physical Review B*, vol. 87, p. 214413, Jun 2013. [Online]. Available: https://link.aps.org/doi/10.1103/PhysRevB.87.214413

[164] M. Matsuda, S. E. Dissanayake, T. Hong, Y. Ozaki, T. Ito, M. Tokunaga, X. Z. Liu, M. Bartkowiak, and O. Prokhnenko, "Magnetic field induced antiferromagnetic cone structure in multiferroic $BiFeO_3$," *Physical Review*

Materials, vol. 4, no. 3, p. 034412, Mar 2020. [Online]. Available: https://doi.org/10.1103/physrevmaterials.4.034412

[165] C. Daumont, W. Ren, I. C. Infante, S. Lisenkov, J. Allibe, C. Carrétéro, S. Fusil, E. Jacquet, T. Bouvet, F. Bouamrane, S. Prosandeev, G. Geneste, B. Dkhil, L. Bellaiche, A. Barthélémy, and M. Bibes, "Strain dependence of polarization and piezoelectric response in epitaxial $BiFeO_3$ thin films," *J. Phys. Condens. Matter*, vol. 24, no. 16, p. 162202, Apr. 2012.

[166] D. Sando, A. Barthélémy, and M. Bibes, "$BiFeO_3$ epitaxial thin films and devices: past, present and future," *Journal of Physics: Condensed Matter*, vol. 26, no. 47, p. 473201, oct 2014. [Online]. Available: https://dx.doi.org/10.1088/0953-8984/26/47/473201

[167] D. Albrecht, S. Lisenkov, W. Ren, D. Rahmedov, I. A. Kornev, and L. Bellaiche, "Ferromagnetism in multiferroic $BiFeO_3$ films: A first-principles-based study," *Phys. Rev. B*, vol. 81, p. 140401, Apr 2010. [Online]. Available: https://link.aps.org/doi/10.1103/PhysRevB.81.140401

[168] P. Rovillain, R. de Sousa, Y. Gallais, A. Sacuto, M. A. Méasson, D. Colson, A. Forget, M. Bibes, A. Barthélémy, and M. Cazayous, "Electric-field control of spin waves at room temperature in multiferroic $BiFeO_3$," *Nat. Mater.*, vol. 9, no. 12, pp. 975–979, Dec. 2010.

[169] A. Haykal, J. Fischer, W. Akhtar, J.-Y. Chauleau, D. Sando, A. Finco, F. Godel, Y. A. Birkhölzer, C. Carrétéro, N. Jaouen, M. Bibes, M. Viret, S. Fusil, V. Jacques, and V. Garcia, "Antiferromagnetic textures in $BiFeO_3$ controlled by strain and electric field," *Nature Communications*, vol. 11, no. 1, p. 1704, Apr 2020. [Online]. Available: https://doi.org/10.1038/s41467-020-15501-8

[170] P. Meisenheimer, G. Moore, S. Zhou, H. Zhang, X. Huang, S. Husain, X. Chen, L. W. Martin, K. A. Persson, S. Griffin, L. Caretta, P. Stevenson, and R. Ramesh, "Switching the spin cycloid in $BiFeO_3$ with an electric field," *Nature Communications*, vol. 15, no. 1, p. 2903, Apr 2024. [Online]. Available: https://doi.org/10.1038/s41467-024-47232-5

[171] M. Tokunaga, M. Akaki, T. Ito, S. Miyahara, A. Miyake, H. Kuwahara, and N. Furukawa, "Magnetic control of transverse electric polarization in $BiFeO_3$," *Nature Communications*, vol. 6, p. 5878, 2015. [Online]. Available: http://dx.doi.org/10.1038/ncomms6878

[172] R. S. Fishman, N. Furukawa, J. T. Haraldsen, M. Matsuda, and S. Miyahara, "Identifying the spectroscopic modes of multiferroic $BiFeO_3$,"

Phys. Rev. B, vol. 86, p. 220402, Dec 2012. [Online]. Available: https://link.aps.org/doi/10.1103/PhysRevB.86.220402

[173] R. S. Fishman, "Field dependence of the spin state and spectroscopic modes of multiferroic $BiFeO_3$," *Phys. Rev. B*, vol. 87, p. 224419, Jun 2013. [Online]. Available: https://link.aps.org/doi/10.1103/PhysRevB.87.224419

[174] H. Katsura, N. Nagaosa, and A. V. Balatsky, "Spin current and magnetoelectric effect in noncollinear magnets," *Phys. Rev. Lett.*, vol. 95, p. 057205, Jul 2005. [Online]. Available: https://link.aps.org/doi/10.1103/PhysRevLett.95.057205

[175] M. Cazayous, Y. Gallais, A. Sacuto, R. de Sousa, D. Lebeugle, and D. Colson, "Possible observation of cycloidal electromagnons in $BiFeO_3$," *Phys. Rev. Lett.*, vol. 101, p. 037601, Jul 2008. [Online]. Available: https://link.aps.org/doi/10.1103/PhysRevLett.101.037601

[176] R. de Sousa and J. E. Moore, "Optical coupling to spin waves in the cycloidal multiferroic $BiFeO_3$," *Phys. Rev. B*, vol. 77, p. 012406, Jan 2008. [Online]. Available: https://link.aps.org/doi/10.1103/PhysRevB.77.012406

[177] P. Rovillain, M. Cazayous, Y. Gallais, A. Sacuto, R. P. S. M. Lobo, D. Lebeugle, and D. Colson, "Polar phonons and spin excitations coupling in multiferroic $BiFeO_3$ crystals," *Phys. Rev. B*, vol. 79, p. 180411(R), May 2009. [Online]. Available: https://link.aps.org/doi/10.1103/PhysRevB.79.180411

[178] G. A. Komandin, V. I. Torgashev, A. A. Volkov, O. E. Porodinkov, I. E. Spektor, and A. A. Bush, "Optical properties of $BiFeO_3$ ceramics in the frequency range 0.3–30.0 THz," *Phys. Solid State*, vol. 52, no. 4, pp. 734–743, Apr. 2010.

[179] D. G. Farkas, D. Szaller, I. Kézsmárki, U. Nagel, T. Rõõm, L. Peedu, J. Viirok, J. S. White, R. Cubitt, T. Ito, R. S. Fishman, and S. Bordács, "Selection rules and dynamic magnetoelectric effect of the spin waves in multiferroic $BiFeO_3$," *Phys. Rev. B*, vol. 104, p. 174429, Nov 2021. [Online]. Available: https://link.aps.org/doi/10.1103/PhysRevB.104.174429

[180] S. Bordács, D. G. Farkas, J. S. White, R. Cubitt, L. DeBeer-Schmitt, T. Ito, and I. Kézsmárki, "Magnetic Field Control of Cycloidal Domains and Electric Polarization in Multiferroic $BiFeO_3$," *Physical Review Letters*, vol. 120, no. 14, p. 147203, 2018.

[181] M. Białek, T. Ito, H. Rønnow, and J.-P. Ansermet, "Terahertz-optical properties of a bismuth ferrite single crystal," *Phys. Rev. B*, vol. 99, p. 064429,

Feb 2019. [Online]. Available: https://link.aps.org/doi/10.1103/PhysRevB.99.064429

[182] K. Matsuura, Y. Nishizawa, Y. Kinoshita, T. Kurumaji, A. Miyake, H. Oike, M. Tokunaga, Y. Tokura, and F. Kagawa, “Low-temperature hysteresis broadening emerging from domain-wall creep dynamics in a two-phase competing system,” *Communications Materials*, vol. 4, no. 1, p. 71, Sep 2023. [Online]. Available: https://doi.org/10.1038/s43246-023-00399-8

[183] S. Ghara, E. Barts, K. Vasin, D. Kamenskyi, L. Prodan, V. Tsurkan, I. Kézsmárki, M. Mostovoy, and J. Deisenhofer, “Magnetization reversal through an antiferromagnetic state,” *Nature Communications*, vol. 14, no. 1, p. 5174, Aug 2023. [Online]. Available: https://doi.org/10.1038/s41467-023-40722-y

[184] P. Pincus, “Theory of magnetic resonance in αFe$_2$O$_3$,” *Phys. Rev. Lett.*, vol. 5, pp. 13–15, Jul 1960. [Online]. Available: https://link.aps.org/doi/10.1103/PhysRevLett.5.13

[185] T. Rõõm, J. Viirok, L. Peedu, U. Nagel, D. G. Farkas, D. Szaller, V. Kocsis, S. Bordács, I. Kézsmárki, D. L. Kamenskyi, H. Engelkamp, M. Ozerov, D. Smirnov, J. Krzystek, K. Thirunavukkuarasu, Y. Ozaki, Y. Tomioka, T. Ito, T. Datta, and R. S. Fishman, “Magnetoelastic distortion of multiferroic BiFeO$_3$ in the canted antiferromagnetic state,” *Physical Review B*, vol. 102, no. 21, p. 214410, Dec. 2020. [Online]. Available: https://doi.org/10.1103/physrevb.102.214410

[186] F. Kagawa, M. Mochizuki, Y. Onose, H. Murakawa, Y. Kaneko, N. Furukawa, and Y. Tokura, “Dynamics of multiferroic domain wall in spin-cycloidal ferroelectric DyMnO$_3$,” *Phys. Rev. Lett.*, vol. 102, p. 057604, Feb 2009. [Online]. Available: https://link.aps.org/doi/10.1103/PhysRevLett.102.057604

[187] J. Lu, A. Günther, F. Schrettle, F. Mayr, S. Krohns, P. Lunkenheimer, A. Pimenov, V. D. Travkin, A. A. Mukhin, and A. Loidl, “On the room temperature multiferroic BiFeO$_3$: magnetic,dielectric and thermal properties,” *The European Physical Journal B*, vol. 75, no. 4, pp. 451–460, Jun 2010. [Online]. Available: https://doi.org/10.1140/epjb/e2010-00170-x

[188] F. Kagawa, Y. Onose, Y. Kaneko, and Y. Tokura, “Relaxation dynamics of multiferroic domain walls in DyMnO$_3$ with cycloidal spin order,” *Phys. Rev. B*, vol. 83, p. 054413, Feb 2011. [Online]. Available: https://link.aps.org/doi/10.1103/PhysRevB.83.054413

[189] L. Rózsa, M. Weißenhofer, and U. Nowak, “Spin waves in skyrmionic structures with various topological charges,” *Journal of Physics: Condensed Matter*, vol. 33, no. 5, p. 054001, nov 2020. [Online]. Available: https://dx.doi.org/10.1088/1361-648X/abc404

[190] N. E. Kulagin, A. F. Popkov, and A. K. Zvezdin, “Spatially modulated antiferromagnetic structures in an easy-plane multiferroic,” *Physics of the Solid State*, vol. 53, no. 5, pp. 970–977, May 2011. [Online]. Available: https://doi.org/10.1134/S1063783411050155

[191] G. H. Wannier, “Antiferromagnetism. The triangular ising net,” *Phys. Rev.*, vol. 79, pp. 357–364, Jul 1950. [Online]. Available: https://link.aps.org/doi/10.1103/PhysRev.79.357

[192] H. T. Diep and H. Giacomini, “Frustration - exactly solved frustrated models,” in *Frustrated Spin Systems*. WORLD SCIENTIFIC, Jan. 2005, pp. 1–58.

[193] V. Fritsch, J. Hemberger, N. Büttgen, E. W. Scheldt, H. A. K. V. Nidda, A. Loidl, and V. Tsurkan, “Spin and orbital frustration in $MnSc_2S_4$ and $FeSc_2S_4$,” *Physical Review Letters*, vol. 92, 3 2004.

[194] S. Gao, O. Zaharko, V. Tsurkan, Y. Su, J. S. White, G. S. Tucker, B. Roessli, F. Bourdarot, R. Sibille, D. Chernyshov, T. Fennell, A. Loidl, and C. Rüegg, “Spiral spin-liquid and the emergence of a vortex-like state in $MnSc_2S_4$,” *Nature Physics*, vol. 13, pp. 157–161, 2 2017.

[195] S. Gao, H. D. Rosales, F. A. G. Albarracín, V. Tsurkan, G. Kaur, T. Fennell, P. Steffens, M. Boehm, P. Čermák, A. Schneidewind, E. Ressouche, D. C. Cabra, C. Rüegg, and O. Zaharko, “Fractional antiferromagnetic skyrmion lattice induced by anisotropic couplings,” *Nature*, vol. 586, pp. 37–41, 10 2020.

[196] H. D. Rosales, F. A. G. Albarracín, K. Guratinder, V. Tsurkan, L. Prodan, E. Ressouche, and O. Zaharko, “Anisotropy-driven response of the fractional antiferromagnetic skyrmion lattice in $MnSc_2S_4$ to applied magnetic fields,” *Phys. Rev. B*, vol. 105, p. 224402, Jun 2022. [Online]. Available: https://link.aps.org/doi/10.1103/PhysRevB.105.224402

[197] A. Bogdanov and A. Hubert, “Thermodynamically stable magnetic vortex states in magnetic crystals,” *Journal of Magnetism and Magnetic Materials*, vol. 138, no. 3, pp. 255–269, 1994. [Online]. Available: https://www.sciencedirect.com/science/article/pii/0304885394900469

[198] U. K. Rössler, A. N. Bogdanov, and C. Pfleiderer, “Spontaneous skyrmion ground states in magnetic metals,” *Nature*, vol. 442, no. 7104, pp. 797–801, Aug. 2006.

[199] T. Okubo, S. Chung, and H. Kawamura, “Multiple-q states and the skyrmion lattice of the triangular-lattice Heisenberg antiferromagnet under magnetic fields,” *Phys. Rev. Lett.*, vol. 108, p. 017206, Jan 2012. [Online]. Available: https://link.aps.org/doi/10.1103/PhysRevLett.108.017206

[200] N. Nagaosa and Y. Tokura, “Topological properties and dynamics of magnetic skyrmions,” *Nat. Nanotechnol.*, vol. 8, no. 12, pp. 899–911, Dec. 2013. [Online]. Available: https://www.nature.com/articles/nnano.2013.243

[201] A. O. Leonov and M. Mostovoy, “Multiply periodic states and isolated skyrmions in an anisotropic frustrated magnet,” *Nature Communications*, vol. 6, p. 8275, 11 2015.

[202] S. Hayami, “Skyrmion crystals in centrosymmetric triangular magnets under hexagonal and trigonal single-ion anisotropy,” *Journal of Magnetism and Magnetic Materials*, vol. 553, p. 169220, 2022. [Online]. Available: https://www.sciencedirect.com/science/article/pii/S0304885322001767

[203] T. Skyrme, “A unified field theory of mesons and baryons,” *Nuclear Physics*, vol. 31, pp. 556–569, 1962. [Online]. Available: https://www.sciencedirect.com/science/article/pii/0029558262907757

[204] F. S. Galasso, “Spinel and related structures,” in *Structure and Properties of Inorganic Solids*, ser. International Series of Monographs in Solid State Physics, F. S. Galasso, Ed. Pergamon, 1970, ch. 8, pp. 211–234. [Online]. Available: https://www.sciencedirect.com/science/article/pii/B9780080068732500111

[205] A. P. Ramirez, “Strongly geometrically frustrated magnets,” *Annu. Rev. Mater. Sci.*, vol. 24, no. 1, pp. 453–480, Aug. 1994.

[206] J. E. Greedan, “Geometrically frustrated magnetic materials,” in *Functional Oxides*. Chichester, UK: John Wiley & Sons, Ltd, Jun. 2010, pp. 41–117.

[207] A. P. Ramirez, G. P. Espinosa, and A. S. Cooper, “Strong frustration and dilution-enhanced order in a quasi-2D spin glass,” *Phys. Rev. Lett.*, vol. 64, no. 17, pp. 2070–2073, Apr. 1990.

[208] K. Hirakawa, H. Kadowaki, and K. Ubukoshi, “Experimental studies of triangular lattice antiferromagnets with S=1/2: $NaTiO_2$ and $LiNiO_2$,” *J. Phys. Soc. Jpn.*, vol. 54, no. 9, pp. 3526–3536, Sep. 1985.

[209] H. Takeda, M. Kawano, K. Tamura, M. Akazawa, J. Yan, T. Waki, H. Nakamura, K. Sato, Y. Narumi, M. Hagiwara, M. Yamashita, and C. Hotta, “Magnon thermal hall effect via emergent SU(3) flux on the antiferromagnetic skyrmion lattice,” *Nature Communications*, vol. 15, no. 1, Jan 2024. [Online]. Available: https://doi.org/10.1038/s41467-024-44793-3

[210] D. Bergman, J. Alicea, E. Gull, S. Trebst, and L. Balents, “Order-by-disorder and spiral spin-liquid in frustrated diamond-lattice antiferromagnets,” *Nature Physics*, vol. 3, no. 7, pp. 487–491, Jul 2007. [Online]. Available: https://doi.org/10.1038/nphys622

[211] Y. Takahashi, R. Shimano, Y. Kaneko, H. Murakawa, and Y. Tokura, “Magnetoelectric resonance with electromagnons in a perovskite helimagnet,” *Nature Physics*, vol. 8, pp. 121–125, 2 2012.

[212] M. Date, K. Okuda, and K. Kadowaki, “Electron spin resonance in the itinerant-electron helical magnet MnSi,” *Journal of the Physical Society of Japan*, vol. 42, pp. 1555–1561, 5 1977.

[213] T. Schwarze, J. Waizner, M. Garst, A. Bauer, I. Stasinopoulos, H. Berger, C. Pfleiderer, and D. Grundler, “Universal helimagnon and skyrmion excitations in metallic, semiconducting and insulating chiral magnets,” *Nature Materials*, vol. 14, no. 5, pp. 478–483, May 2015. [Online]. Available: https://doi.org/10.1038/nmat4223

[214] Y. Onose, Y. Okamura, S. Seki, S. Ishiwata, and Y. Tokura, “Observation of magnetic excitations of skyrmion crystal in a helimagnetic insulator Cu_2OSeO_3,” *Phys. Rev. Lett.*, vol. 109, p. 037603, Jul 2012. [Online]. Available: https://link.aps.org/doi/10.1103/PhysRevLett.109.037603

[215] M. Mochizuki, “Spin-wave modes and their intense excitation effects in skyrmion crystals,” *Phys. Rev. Lett.*, vol. 108, p. 017601, Jan 2012. [Online]. Available: https://link.aps.org/doi/10.1103/PhysRevLett.108.017601

[216] M. Garst, J. Waizner, and D. Grundler, “Collective spin excitations of helices and magnetic skyrmions: review and perspectives of magnonics in non-centrosymmetric magnets,” *J. Phys. D Appl. Phys.*, vol. 50, no. 29, p. 293002, Jul. 2017.

[217] L. Xing, D. Hua, and W. Wang, “Magnetic excitations of skyrmions in antiferromagnetic-exchange coupled disks,” *Journal of Applied Physics*, vol. 124, no. 12, p. 123904, Sep 2018. [Online]. Available: https://doi.org/10.1063/1.5042794

[218] M. Lonsky and A. Hoffmann, “Coupled skyrmion breathing modes in synthetic ferri- and antiferromagnets,” *Phys. Rev. B*, vol. 102, p. 104403, Sep 2020. [Online]. Available: https://link.aps.org/doi/10.1103/PhysRevB.102.104403

[219] X.-G. Wang, L. Chotorlishvili, G. Tatara, A. Dyrdał, G. hua Guo, V. K. Dugaev, J. Barnaś, S. Parkin, and A. Ernst, “Skyrmion lattice hosted in synthetic antiferromagnets and helix modes,” *Physical Review B*, vol. 106, no. 10, Sep. 2022. [Online]. Available: https://doi.org/10.1103/physrevb.106.104424

[220] M. Lonsky and A. Hoffmann, “Dynamic fingerprints of synthetic antiferromagnet nanostructures with interfacial Dzyaloshinskii–Moriya interaction,” *Journal of Applied Physics*, vol. 132, no. 4, p. 043903, Jul 2022. [Online]. Available: https://doi.org/10.1063/5.0101522

[221] C. E. A. Barker, E. Haltz, T. A. Moore, and C. H. Marrows, “Breathing modes of skyrmion strings in a synthetic antiferromagnet multilayer,” *Journal of Applied Physics*, vol. 133, no. 11, p. 113901, Mar 2023. [Online]. Available: https://doi.org/10.1063/5.0142772

[222] A. J. Sievers and M. Tinkham, “Far infrared antiferromagnetic resonance in MnO and NiO,” *Physical Review*, vol. 129, no. 4, pp. 1566–1571, Feb. 1963. [Online]. Available: https://doi.org/10.1103/physrev.129.1566

[223] R. S. Fishman, T. Rõõm, and R. de Sousa, “Normal modes of a spin cycloid or helix,” *Physical Review B*, vol. 99, p. 064414, 2 2019.

[224] H. Martinho, N. O. Moreno, J. A. Sanjurjo, C. Rettori, A. J. García-Adeva, D. L. Huber, S. B. Oseroff, W. Ratcliff, S.-W. Cheong, P. G. Pagliuso, J. L. Sarrao, and G. B. Martins, “Studies of the three-dimensional frustrated antiferromagnetic $ZnCr_2O_4$,” *Journal of Applied Physics*, vol. 89, no. 11, pp. 7050–7052, Jun. 2001. [Online]. Available: https://doi.org/10.1063/1.1358340

[225] T. Dohi, S. DuttaGupta, S. Fukami, and H. Ohno, “Formation and current-induced motion of synthetic antiferromagnetic skyrmion bubbles,” *Nature Communications*, vol. 10, no. 1, p. 5153, Nov 2019. [Online]. Available: https://doi.org/10.1038/s41467-019-13182-6

[226] A. Aldarawsheh, M. Sallermann, M. Abusaa, and S. Lounis, “Current-driven dynamics of antiferromagnetic skyrmions: from skyrmion Hall effects to hybrid inter-skyrmion scattering,” *npj Spintronics*, vol. 2, no. 1, p. 41, Aug 2024. [Online]. Available: https://doi.org/10.1038/s44306-024-00049-w